Title
Search for New Physics in pp Collisions at 7 TeV Center-of-Mass Energy Using Diphoton Events with Large Missing Transverse Energy in the CMS Experiment at the LHC

Author
Stringer, Robert

Publication Date
2011

UNIVERSITY OF CALIFORNIA
RIVERSIDE

Search for New Physics in pp Collisions at 7 TeV Center-of-Mass Energy Using Diphoton Events with Large Missing Transverse Energy in the CMS Experiment at the LHC

A Dissertation submitted in partial satisfaction
of the requirements for the degree of

Doctor of Philosophy

in

Physics

by

Robert Wayne Stringer

June 2011

Dissertation Committee:

Dr. Gail Hanson, Chairperson
Dr. Ken Barish
Dr. Jose Wudka

The Dissertation of Robert Wayne Stringer is approved:

Committee Chairperson

University of California, Riverside

Acknowledgments

I would like to acknowledge Gail Hanson and Frank Hartmann. Without their support this wouldn't have been possible.

For Linda and my boys, Nathaniel and Nicholas.

ABSTRACT OF THE DISSERTATION

Search for New Physics in pp Collisions at 7 TeV Center-of-Mass Energy Using Diphoton Events with Large Missing Transverse Energy in the CMS Experiment at the LHC

by

Robert Wayne Stringer

Doctor of Philosophy, Graduate Program in Physics
University of California, Riverside, June 2011
Dr. Gail Hanson, Chairperson

Many theoretical models of physics beyond the Standard Model provide a signature of two photons and large missing transverse energy (E_T^{miss}) in the final state. This search was performed using 36 pb^{-1} of proton-proton collision data at $\sqrt{s} = 7$ TeV. The candidate events are determined by comparing the E_T^{miss} distribution for events with two photons and at least one hadronic jet with the E_T^{miss} distribution from QCD and electroweak processes that have no true missing transverse energy. 1.2 ± 0.8 background events were expected, with one event observed. This result was interpreted in two theoretical models beyond the Standard Model. The cross section for General Gauge Mediated Supersymmetry Breaking is given an upper limit between 0.3 pb and 1.1 pb. Universal Extra Dimensions has been excluded for all values of $1/R < 889$ GeV. All limits are given at 95% CL.

Contents

List of Figures

List of Tables

Chapter 1

Introduction

1.1 Motivation

The Standard Model of particle physics has been extremely successful since its inception. It has made numerous predictions that have lead to discoveries. Most notably the existence of the W and Z bosons, discovered at CERN in 1980's and the Top quark at Fermilab in 1994. The final piece that would complete the Standard Model is the Higgs boson that is expected to be found at the LHC by 2012. However, there are several consequences of the Standard Model that lead to inconsistencies which can have not yet been solved. These inconsistencies have lead theorists to suggest that there may be new physics beyond the Standard Model.

In the Standard Model there is no explanation for why gravity is so much weaker than the other fundamental forces. It is, in fact, 10^{32} times weaker than the weak force. Also, in calculating the Higgs mass, quantum loop corrections make the mass diverge at energies approaching the Planck mass $M_{Pl} \sim 10^{19}$ GeV. This is known as the gauge hierarchy or naturalness problem. Without some mechanism beyond the standard model to remove these infinities, theorists have been forced to set a cutoff scale for the energy, typically denoted Λ, which makes the quantum corrections finite. Physics beyond the standard model can provide a solution to the hierarchy problem. The theoretical models are widely varied. Two such models are SuperSymmetry and Extra Dimensions.

1.1.1 Gauge-Mediated SUSY

SuperSymmetry (SUSY) is an elegant solution to the gauge hierarchy problem. Each SM particle has a superpartner which has a spin differing by 1/2. This way every fermion has boson superpartner and vice-versa. This solves the hierarchy problem because the loop corrections between fermion and boson differ by a factor of -1, in effect canceling the loop corrections and protecting the Higgs mass. There are many flavors of SUSY models, each with its own phenomenology. This analysis focuses on a variant of the Minimally Supersymmetric Standard Model where the symmetry is broken by gauge mediation. This model is known as Gauge-Mediated Supersymmetry Breaking (GMSB). There are further simplifications that reduce the number of free parameters, the simplest being minimal Gauge-Mediated Supersymmetry Breaking (mGMSB) which has only five free parameters. The result here is given in terms of General Gauge Mediation (GGM) in which the gluino, squark, and neutralino masses are varied. In this model, the next to lightest superpartner (NLSP) is the neutralino (χ_1^0) and the lightest superpartner (LSP) is the gravitino ($\tilde{G}$). Because the number of supersymmetric particles created is conserved (R-parity), two neutralinos will be produced decaying to two photons and two gravitinos. Again by R-parity conservation, the gravitinos cannot decay and are stable, making them a dark matter candidate.

1.1.2 Universal Extra Dimensions

Another model of new physics that can provide an experimental signature of two photons and missing transverse energy is the Universal Extra Dimensions model[3]. In this model, the existence of compact additional dimensions is postulated, in which SM particles are allowed to propagate. This explains the weakness of gravity as due to the gravitational force propagating into the extra dimensions. For each SM particle, as it propagates into the extra dimensions, excitations are produced. These excitations, essentially standing waves of different invariant masses in a compactified dimension, are described as a Kaluza-Klein (KK) tower. These KK particles can then cancel the divergences of the SM particle, thus solving the hierarchy problem. In this analysis, a scenario is presented where UED space is embedded in an additional space which has six Large Extra Dimensions (LED) [4]. In the LED only the graviton is allowed to propagate, accounting for the weakness of gravity. With the presence of the LEDs the lightest KK particle (LKP), the KK photon (γ^*), is then allowed to decay gravitationally to a photon and a graviton $\gamma^* \to \gamma + G$, where the graviton escapes the detector undetected. Two decay chains are produced per event resulting in the two photons and missing transverse energy final state.

Chapter 2

The Large Hadron Collider

The Large Hadron Collider, built on the French/Swiss border, is a two-ring superconducting hadron collider. It was designed and operated by the European Center for Nuclear Research (CERN). All elements of the description of the LHC found here, unless otherwise noted, are taken from Ref. [5].

The LHC was installed in the 26.7 km circumference tunnel originally used by the Large Electron-Positron (LEP) collider. The tunnel is at a depth of between 45m and 170m below the surface and is tilted towards Lake Geneva at an angle of 1.4 deg. The LHC was designed to provide proton-proton collisions at a center-of-mass energy ($\sqrt{s}$) of 14 TeV and lead ion (Pb-Pb) collisons at $\sqrt{s} = 2.8$ TeV per nucleon. The LHC has two general high-luminosity experiments, the CMS (Compact Muon Solenoid), described in Chapter 3 and ATLAS (A Toroidal LHC Apparatus), which are designed to receive a peak luminosity of $L = 10^{34}\text{cm}^{-2}\text{s}^{-1}$. There is also a low luminosity b-physics experiment LHCb and a heavy ion experiment ALICE (A Large Ion Collider Experiment), which receive a peak luminosity of $L = 10^{32}\text{cm}^{-2}\text{s}^{-1}$ and $L = 10^{27}\text{cm}^{-2}\text{s}^{-1}$, respectively.

While the initial plans called for the startup of the LHC at the design energy of $\sqrt{s} = 14$ TeV, an accident occurred during the commissioning of the magnets. As the bending magnets in sectors 3 and 4 were raised to the full field for 7 TeV beams, a "quench" occurred where the magnets stopped being superconducting. During a quench, the stored energy of the magnet is dissipated through a "busbar" designed to handle large currents. However, due to faulty connections, the busbars had higher than expected resistances, causing them to melt. The heat generated caused a rupture in the Helium tank resulting in the explosive release of 3-4 tons of helium. The explosion damaged over 50 magnets and resulted in an 18 month delay. When the LHC resumed operation in 2010, it was at the lower energy of $\sqrt{s} = 7$ TeV. During the 2010 run, a peak instantaneous luminosity of $L = 5 \times 10^{32}\text{cm}^{-2}\text{s}^{-1}$ was achieved.

2.1 LHC specifications

The luminosity delivered by the LHC is based only on the beam parameters [5]. For a gaussian distribution, it is given as:

$$L = \frac{N_b^2 n_b f_{rev} \gamma_r}{4\pi \varepsilon_n \beta^\star} F \tag{2.1}$$

where N_b is the number of particles per bunch, n_b is the number of bunches per beam, f_{rev} is the frequency of revolution, γ_r is the relativistic gamma factor, ε_n is the beam emittance, $\beta^\star$ is the beta function[1] at the interaction point, and F is a geometric factor due to the crossing angle, which is defined:

$$F = \left(1 + \left(\frac{\theta_c \sigma_z}{2\sigma^\star}\right)^2\right)^{1/2} \tag{2.2}$$

---

[1] The beta function defines the envelope of particle motion[6]. To maximize luminosity $\beta^\star$ should be minimized. During the majority of the 2010 run $\beta^\star$ was reduced to 2 meters.

with θ_c being the crossing angle at the interaction point, σ_z is the RMS bunch length, and $\sigma^\star$ is the transverse RMS beam size at the interaction point.

The maximum acceptable transverse emittance is limited by the mechanical aperture of the beam pipe, the beam-beam interaction and the peak of the β function in the LHC arcs (180 meters). The beam-beam interaction is measured by the linear tune shift equation:

$$\xi = \frac{N_b r_p}{4\pi\varepsilon_n} \tag{2.3}$$

where r_p is the classical proton radius $r_p = e^2/(4\pi\varepsilon_0 m_p c^2)$. In order to have quality collisions at the three proton experiments, the linear shift should not exceed 0.005. Solving for the bunch intensity in Eq. 2.3, the maximum bunch intensity is $N_b = 1.15 \times 10^{11}$. The mechanical aperture of the triplet magnets also places limits on the $\beta^\star$ and crossing angles at the interaction point. All of these parameters limit the maximum attainable instantaneous luminosity. In order to achieve the design luminosity of $L = 10^{34}\mathrm{cm}^2\mathrm{s}^1$, with the mechanical limits, 2808 bunches of nominal intensity with a bunch spacing of 25 ns are required. During the 2010 proton run, problems with electron clouds prevented stable operation at bunch spacings less than 150 ns. This limited the number of bunches per beam to 424. An example calculation of the expected luminosity at the end of the 2010 proton run follows.

At the end of the 2010 proton run, the fill scheme used at the LHC was $150ns\_368b\_348\_15\_344\_4x8bpi19inj$. This translates to 150ns bunch spacing, 368 bunches per beam, 344 bunches colliding at point 1 (ATLAS) and point 5 (CMS), 15 bunches colliding at point 8 (LHCb), 4 bunch trains of 8 bunches , with the fill being loaded in 18 injections. Using Eq. 2.1, we can calculate the approximate luminosity delivered to

CMS and ATLAS.

At an energy of 3.5 TeV the proton mass is negligible, thus $E = p$. Then momentum can be expressed in terms of the relativistic gamma factor, $p = \gamma mc$. Solving for γ_r for 3.5 TeV protons, then $\gamma_r = 3731$. The frequency of revolution, with $v \approx c$, is $11235Hz$. Ignoring the geometric factor F and assuming nominal bunch intensity, the expected luminosity is:

$$L = \frac{(1.1 \times 10^{11})^2(384)(11275s^{-1})(3731)}{4\pi(2.0 \times 10^{-4}cm)(2.0 \times 10^{2}cm)} = 2.87 \times 10^{32}cm^{-2}s^{-1} \tag{2.4}$$

This value agrees well with the measured luminosity at CMS of $1.92{\times}10^{32}\mathrm{cm}^{-2}\mathrm{s}^{-1}$.

2.2 LHC Magnets

The superconducting magnets used in the LHC are constructed using NbTi superconductors, cooled by supercritical helium. The NbTi technology is well understood and has been used for other accelerators such as the Tevatron, HERA, and RHIC. However, because the field required at the LHC, over 8 T, is greater than that of the other experiments, which are at most 5 T, the LHC magnets are operated at a colder temperature, less than 2K as opposed to 4.2K. This lower temperature reduces the heat capacity of the superconducting cable and thus reduces the amount of energy required to cause a quench, when the magnet temperature is raised to the point at which the cable is no longer superconducting. The difference between the critical and operating temperatures is known as the “margin” and is shown in Fig. 2.1.

The LHC uses 1232 dipoles in the ring, 154 per arc. The purpose of the dipoles is to bend the path of the beam around the arcs. To bend the beam at the nominal

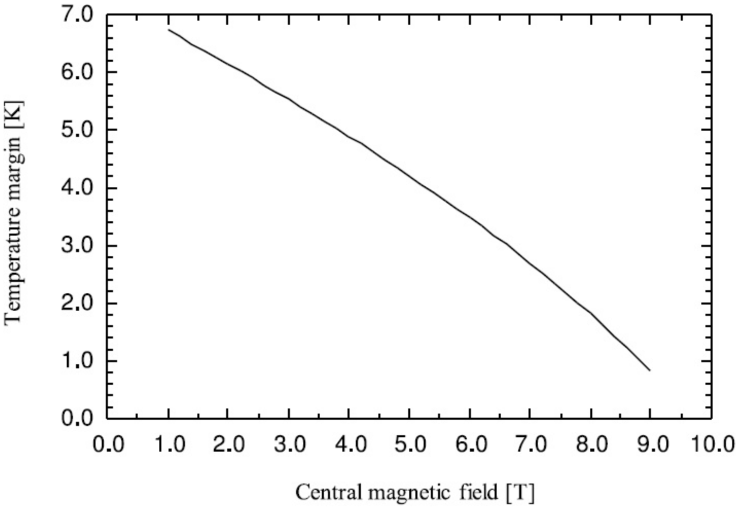

Figure 2.1: Temperature margin for the inner layer of the LHC magnets at normal operating temperature.

energy of 7 TeV, a magnetic field of 8.33 T is required. The dipoles use two types of superconducting cables. The inner layer of the magnet uses cables with 28 strands of a diameter of 1.065 mm and the outer layer has cables with 36 strands of 0.825 mm. Each strand consists of superconducting filaments of 7 μm and 6 μm for the inner and outer layers, respectively. The magnets have an aperture of 56 mm and due to limited space within the LHC tunnel, two dipole channels share a common cold mass. This results in a complicated magnet configuration because the field in each channel is in opposite directions.

In addition to the bending dipoles, the LHC also utilizes 858 quadrapole magnets in the "short straight sections" of the ring. These quadrapole magnets serve to focus the beam. There are also "inner triplet" magnets, located near the experiments, that steer the beams into collisions.

The total energy stored in the LHC magnet system is approximately 600 MJ [7]. This presents a challenge to dissipate this much energy in the case of a quench or a

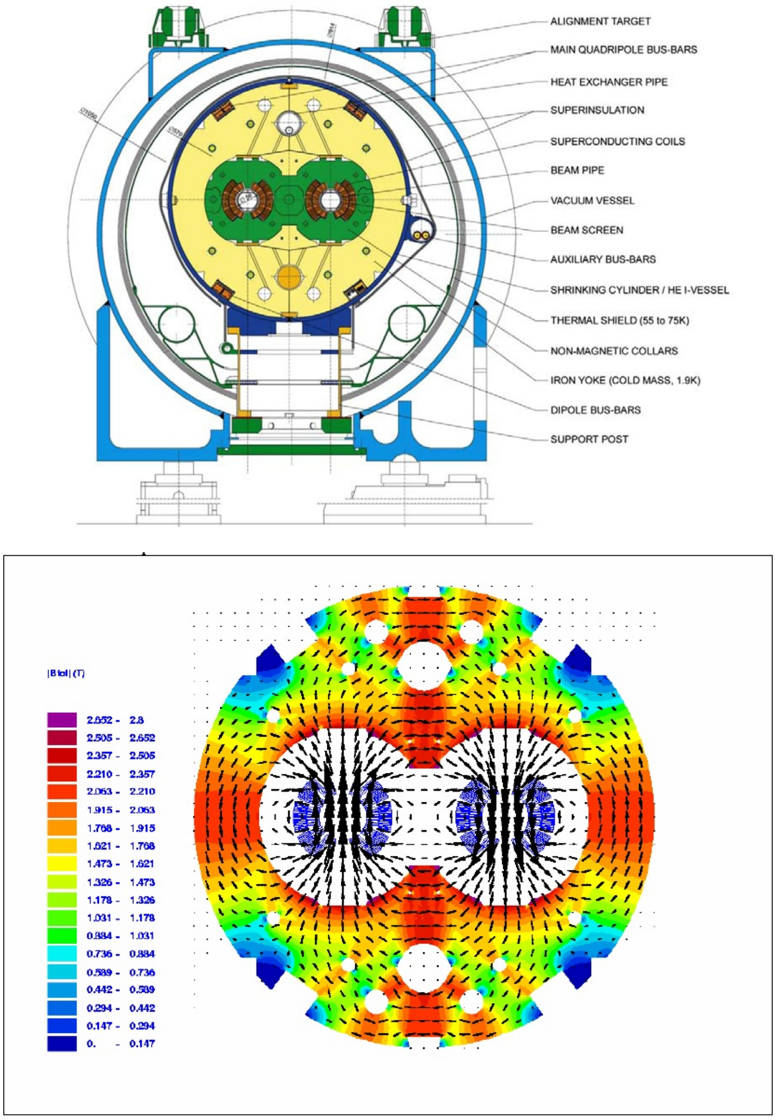

Figure 2.2: Cross-section of an LHC dipole and cryo mass.

malfunction.

2.3 Vacuum System

At the LHC, a vacuum system is used to evacuate the beam pipe and preserve beam lifetimes. In addition to the beam vacuum, vacuum systems are used to insulate the magnets and the helium distribution system. Insulation vacua are maintained at 10^{-1} mbar at room temperature and 10^{-6} mbar at cryogenic temperatures. To achieve the required 100 hours lifetime, the beam pipe vacuum, expressed as gas density normalized to hydrogen, must be below 10^{15} $\mathrm{H_2 m^3}$. Near the experiments the vacuum must be below 10^{15} $\mathrm{H_2 m^3}$ to reduce the beam background.

2.3.1 Beam Vacuum

In addition to preserving the quality of the beam, the beam vacuum system also shields the cryogenic systems from beam-related heat sources. The main heat sources include synchrotron radiation, energy loss due to nuclear scattering, induced currents, and the formation of electron clouds. The loss of vacuum lifetime is dominated by the interaction of protons on the residual gas in the beam pipe.

Table 2.1: Nuclear cross sections at 7 TeV for residual gases and densities and pressures for 100 h lifetime.

Gas	**Nuclear scattering cross section ($\mathbf{cm^2}$)**	**Max gas density**	**Pressure at 5 K**
H_2	9.5×10^{-26}	9.8×10^{14}	6.7×10^{-8}
He	1.26×10^{-25}	7.4×10^{14}	5.1×10^{-8}
CH_4	5.66×10^{-25}	1.6×10^{14}	1.1×10^{-8}
H_2O	5.65×10^{-25}	1.6×10^{14}	1.1×10^{-8}
CO	8.54×10^{-25}	1.1×10^{14}	7.5×10^{-9}
CO_2	1.32×10^{-24}	7.0×10^{13}	4.9×10^{-9}

2.3.2 Insulation Vacua

The insulation vacuum is a much larger volume, approximately 80 m^3 than the beam vacuum. An insulation vacuum volume is used for the magnet cryostats and the QRL[1]. The high volume requires high-capacity ($64 m^3 h^{-1}$) pumps. The vacuum is divided into sectors of 428 m in the QRL and 214 m for the magnet vacuum with 14 magnet sectors and 7 QRL sectors per arc.

2.4 Cryo System

The LHC has the lowest operating temperature of any superconducting accelerator. To maintain the temperature below 1.9 K, the magnets are immersed in a bath of superfluid helium at a pressure of 0.13 mPa. The low temperature maximizes thermal conductivity of the helium and reduces the viscosity so that the helium permeates the magnets. Because the specific heat of the superconducting metals decreases with temperature, the stability of the magnet temperature relies on the large specific heat of superfluid helium. Therefore, the temperature of the helium must remain in a superfluid state even after a fast current discharge.

Design specifications of the LHC require that the entire cold mass of the accelerator, 37×10^6 kg, be brought to operating temperature within 15 days. Differences in temperature in the magnets must be kept below 75 K to avoid mechanical stresses. The cryogenic system must also be able to handle heat generated by magnet quenches without causing significant delays in LHC operation. In case of a quench, the propagation of heat is limited to neighboring magnets. The recovery time is expected to be less than a few hours.

---

[1] The cryogenic feed lines (QRL) distribute helium to the magnet cold masses.

2.4.1 Refrigeration System

The are eight refrigerator plants located at five points around the ring. Each refrigerator plant shown in Fig. 2.3 is comprised of two refrigerator units, a 1.8K unit and a 4.5K unit. Of the eight 4.5 K refrigerator units, four were previously used at LEP. These are of a split-cold-box design where the four new refrigerator units are made with integrated cold-boxes. Because of space considerations, point 2 was not able to contain two plants like points 4, 6, and 8. Instead there is one plant at point 2 and another at point 1. This difference does not affect normal operation but limits the redundancy for sector 2-3.

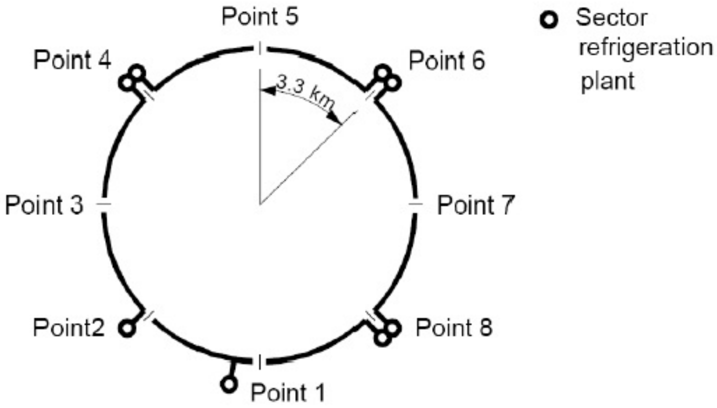

Figure 2.3: General layout of the cryogenic system.

The LHC refrigeration system is capable of handling the nominal demand of 5.3 kW per sector. The 4.5 K refrigerators provide a total capacity of 144 kW at 4.5 K. The 1.8 K refrigerators, providing several kW at 1.8 K, use a system of compressors and heat exchangers to operate efficiently and are connected to the 4.5 K units. The total amount of helium stored in the LHC refrigeration system is 96×10^3kg.

2.4.2 Temperatures

Different parts of the LHC are kept at different temperatures. As it is difficult to maintain 1.8 K, the cryogenic system was designed such that the main influx of heat is absorbed by higher temperature components. The different temperature components are listed in Table 2.2.

Table 2.2: Cryo temperatures.

Temperature	**Component**
50 K to 75 K	Thermal shield for cold masses
4.6 K to 20 K	Beam screens
1.9 K	Superfluid helium for cold masses
4 K	Low pressure helium transport between heat exchanger and refrigeration unit
4.5 K	Saturated helium for insertion magnets, RF cavities
20 K to 300 K	Cooling for upper HTS current leads[8]

2.5 RF systems

The LHC uses a system of superconducting radio frequency (RF) cavities to accelerate the particles in the beam from the injection energy of 450 GeV to the desired beam energy of up to 7 TeV. The RF cavities use oscillating electric fields to push and pull charged particles at a frequency of 400 MHz. Each cavity has a 2 MV accelerating voltage, which provides a field strength of 5.5 MV/m. The cavities are constructed of niobium sputtered onto copper. This is advantageous because excess heat generated is absorbed into the copper, reducing the chances of a quench. Also, pure niobium cavities require shielding from the Earth's magnetic field whereas the niobium/copper cavities do not.

2.6 Beam Injection Systems

The proton beam injected into the LHC is produced and accelerated to the injection energy of 450 GeV by a chain of smaller accelerators. The full chain, shown in Fig. 2.4, is Linac2 → Proton Synchroton Booster (PSB) → Proton Synchroton (PS) → Super Proton Synchroton (SPS). In order for the beam to be suitable for the LHC, it must satisfy many requirements. For example, the beam emittance must be small to pass through the LHC magnets, the beam intensity is limited due to heat effects from synchroton radiation, and there are many others.

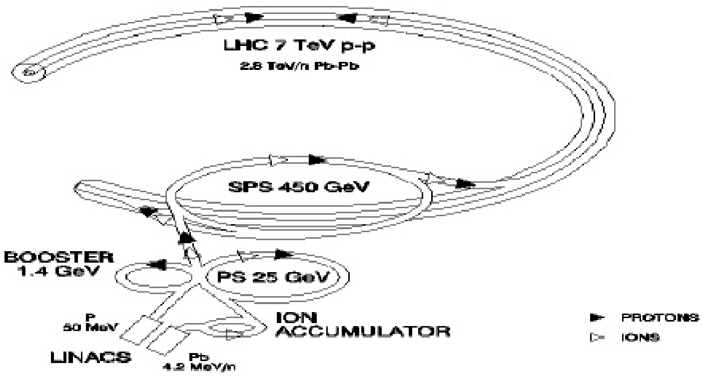

Figure 2.4: The LHC injector complex.

The injection into the LHC, from the SPS, is performed by use of kicker magnets located in RA23, for injection into Ring 1, and RA87, which injects beam into Ring 2. The beam coming from SPS must enter the kicker magnets at an angle of 0.85 mrad. The dipole field in the kickers of 1.2 T-m then deflects to the beam into the proper LHC orbit.

Chapter 3

The CMS Detector

The Compact Muon Solenoid [9] is one of the four large experiments at the CERN LHC. Located in France, in the village of Cessy, at the site known as Point 5 (the fifth of eight sites around the ring in the positive beam direction). The CMS Detector is situated 100 meters below ground, although, unlike the ATLAS detector, the majority of the components were assembled on the surface. The components, once assembled had to be lowered into the experimental cavern. Some of the components were extremely heavy, notably the part of CMS containing the magnet yoke (YB0) which weighs over 10000 tons. The complete CMS detector is 21 meters long, 15 meters wide, and 15 meters tall. It weighs approximately 12500 tons, making it the heaviest of the LHC experiments.

The design of the CMS detector was motivated by both the specifications of the LHC and by the phenomenology of the new physics for which it will search[9]. Due to the high design luminosity (10^{34} cm^{-2}s^{-1}) and high nominal energy (14 TeV) of the LHC, the CMS detector is faced with challenges, both in its ability to do physics and its ability to withstand the harsh LHC environment.

The total cross section for proton-proton interactions at $\sqrt{s} = 14$ TeV is about 100 mb. This implies, at design luminosity, about 10^9 inelastic events per second. The short distance between bunches (25 ns) requires a very robust readout and trigger system. It is expected that each event of interest will have, on average, 20 additional inelastic events from the same collision. To compensate for this effect, the CMS subdetectors must be built with high granularity and good time resolution. They must also be radiation hard to survive the high radiation coming from the interaction point.

In order to meet the physics goals set for the LHC, the CMS detector must:

- Be able to identify muons with good momentum resolution, have good dimuon mass resolution (1% at 100 GeV), and be able to measure the charge of muons with $p < 1$ TeV.
- Have good inner tracking, with excellent resolution and efficiency, and the ability to tag τ and b-jets.
- The electromagnetic calorimeter must have good energy resolution over a large energy range and good π^0 rejection.
- Have good missing transverse energy and di-jet mass resolution.

To accomplish these goals the CMS detector is made up of several subdetectors. A cut-away view of the CMS detector is shown in Figure 3.1. From inside out, CMS is arranged as follows. At the center is the tracking system: Pixel detector and Silicon Strip Tracker. Outside the trackers are the calorimeters: Electromagnetic (ECAL) and Hadronic (HCAL), which are inside the superconducting solenoid coil. The outermost layers make up the muon system: Cathode Strip Chambers (CSC), Resistive Plate Chambers (RPC), and Drift Tubes (DT).

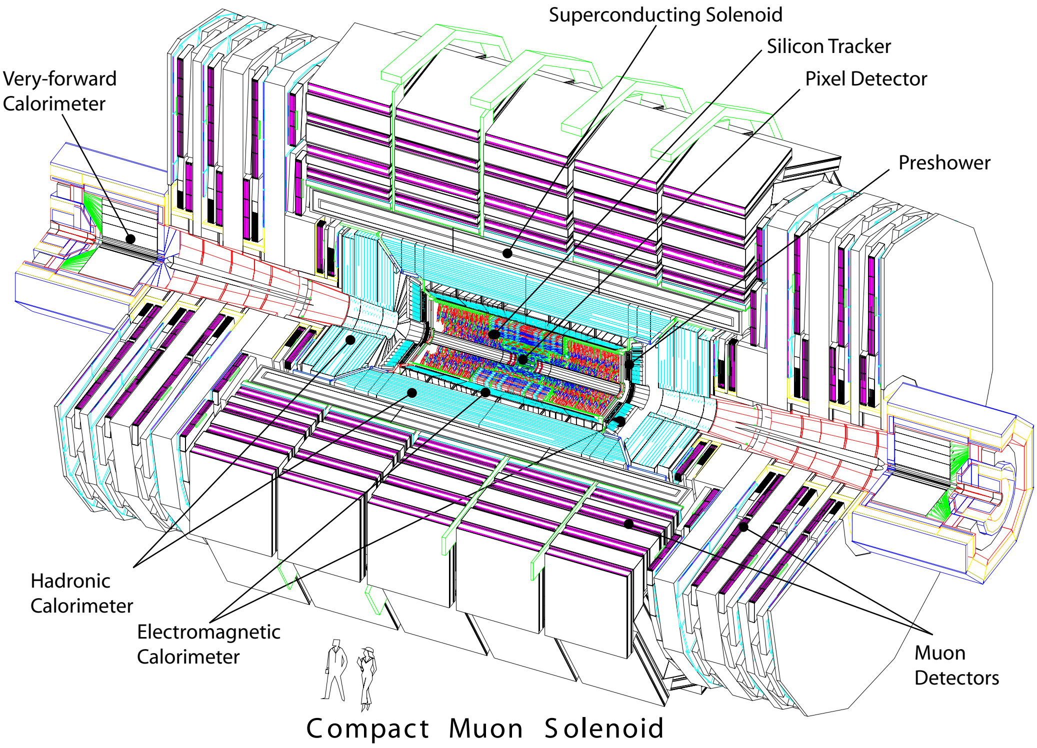

Figure 3.1: A detailed cut-away view of the CMS Detector showing the various detector components[1].

3.1 Analysis Requirements

To look for signals in the diphoton plus large E_T^{miss} channel, the use of several of the CMS subdetectors is required. Photons are identified by deposits in the ECAL with little or no energy deposited in the HCAL. To determine the isolation of photons, the Pixel detector, ECAL, and HCAL each are used. In order to differentiate between photons and electrons, the Pixel detector is used as only charged particles would create Pixel hits.

The measurement of the energy of hadronic jets, as well as the calculation of $E_T^{miss}$is performed using the ECAL and HCAL and then corrected using tracks reconstructed in the tracking system. To measure the momentum of each track in the tracker, the presence of a magnetic field is required.

The following sections describe the various pieces of the CMS detector used by this analysis. The only part of the CMS detector not used by this analysis, the muon system, is also described for completeness.

3.2 CMS Solenoid

The heart of the CMS detector is its four Tesla (T) superconducting solenoid[9]. The magnet bore is 6 meters in diameters and 12.5 meters long. At full field the magnet stores 2.6 GJ of energy. Compared with the strength of the field, the cold mass of the CMS solenoid is low, with the energy-mass ratio being 11.6 KJ/kg. This subjects the magnet to some mechanical deformation during ramping (0.15%), which exceeds that of any previously built solenoid detector magnet.

3.2.1 Magnet Design

The magnet itself is comprised of four layers of windings. The conductor is a NbTi Rutherford cable that has been reinforced with aluminum. To limit the interference with particles coming from the interaction point, the thickness of the coil needs to be limited, with $\Delta R/R \sim 0.1$. As the magnetic pressure ($P = \frac{B_0^2}{2\mu_0} = 6.4$ MPa) is high, the hoop strain (ε) on the structure is high, and is given as follows:

$$\frac{PR}{\Delta R} = Y\varepsilon \tag{3.1}$$

where Y is the elastic modulus of the supporting material (aluminum, $Y = 80$ GPa) and ΔR is 170 mm. This implies a hoop strain of $\varepsilon = 1.5 \times 10^{-3}$, which is high compared to existing detector magnets.

To compensate for the high mechanical stress, an innovative design was used. Since the conductor itself is reinforced, the CMS magnet has essentially a self-supporting conductor, rather than relying on the outer structures for support as was done for previous thin detector solenoids. The magnet structure takes about 70% of the stress generated by the field. A cross section of the magnet cold mass showing the four layers of conductor is presented in Figure 3.2.

3.2.2 Magnet Performance

The CMS solenoid was designed to reach a maximum field strength of 4 T ($I = 19.14$ kA) but is normally operated at 3.8 T ($I = 18.16$ kA). In 2006, magnet tests were performed to gauge the effects of the charge and discharge cycles. The magnet was ramped to differing field strengths and then discharged, using slow and fast discharges, to determine electrical, magnetic, thermal, and mechanical effects of these cycles. During

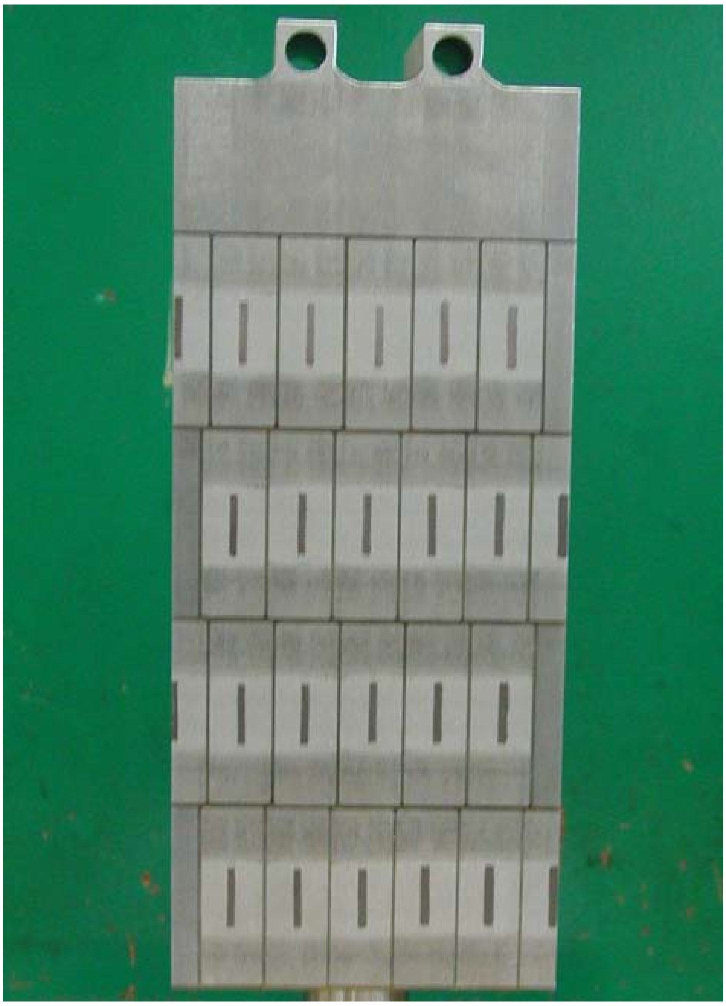

Figure 3.2: Cross section of the cold mass with the details of the 4-layer winding with reinforced conductor.

discharge, the energy of the magnet is dissipated in a 2 MΩ dump resistor for slow dumps or a 30 MΩ resistor for fast dumps. For the slow discharge the refrigeration system can absorb the total heat load and the magnet continues to be superconducting, whereas during a fast dump, some energy is dissipated in the coil. As a result, after a fast dump the coil is no longer superconducting and must be re-cooled, which can take up to 3 days.

After installation, the magnetic field was measured at different locations in the field and compared with computer models[10]. The test was performed at five different values of B_0: 2.02, 3.02, 3.52, 3.81, and 4.01 T. The comparison between the CMS TOSCA model and the measured values matched very well with a discrepancy of 5 mT. The results of the measurements for $B_0 = 4.01$ T are shown in Figure 3.3.

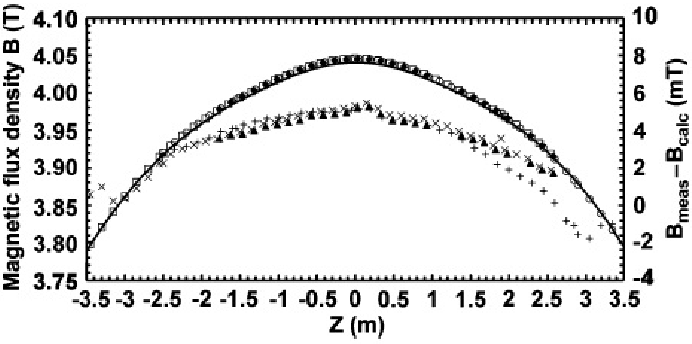

Figure 3.3: Magnetic flux density (left scale) measured and calculated along the coil axis in the horizontal plane at a radius of 1.724 m in the range of ±3.5 m with respect to the coil transverse middle plane. Points (squares and circles) represents different points int the field. The smooth curve represents the calculations done with the CMS TOSCA model. Triangles and crosses show the difference (right scale) between the measurements and calculations.

3.3 Pixel Detector

The CMS Pixel Detector is the innermost subdetector with respect to the beamline. The pixel detector consists of a central barrel region, containing three layers, and two identical endcaps one on each side of the barrel. The geometry of the pixel detector is shown in Figure 3.4. The endcap disks are assembled from 24 overlapping “blades” with modules on each side. The pixel endcap covers the region in pseudorapidity (η) from 1.5 to 2.5. The barrel layers are made up of ladders containing eight modules each. The silicon sensors used by the modules use a “n-on-n” design with isolated pixels. In total, the CMS Pixel Detector has 66 million pixels for high precision tracking.

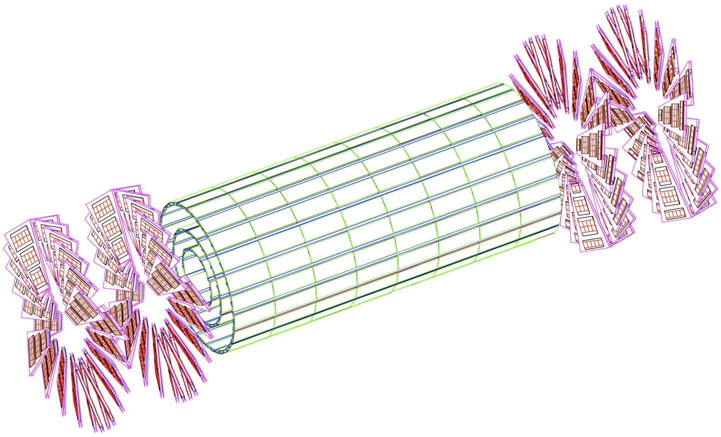

Figure 3.4: The geometry of the CMS Pixel Detector, forward and barrel regions.

3.3.1 Performance

The performance of the CMS Pixel Detector was recently measured using cosmic ray data[11] taken with the CMS magnet at 3.8 T. 370 million events were reconstructed with 80000 tracks in the pixel detector. Measured charge deposition in the pixel detector from cosmic ray muons matched very well to simulation, as shown in Figure 3.5. The position resolution of tracks in the pixel detector can be determined by examining the distance between the hits and the reconstructed track, known as the hit residuals. The distribution of residuals is shown in Figure 3.6. The cosmic ray data indicate a position resolution of 14 μm.

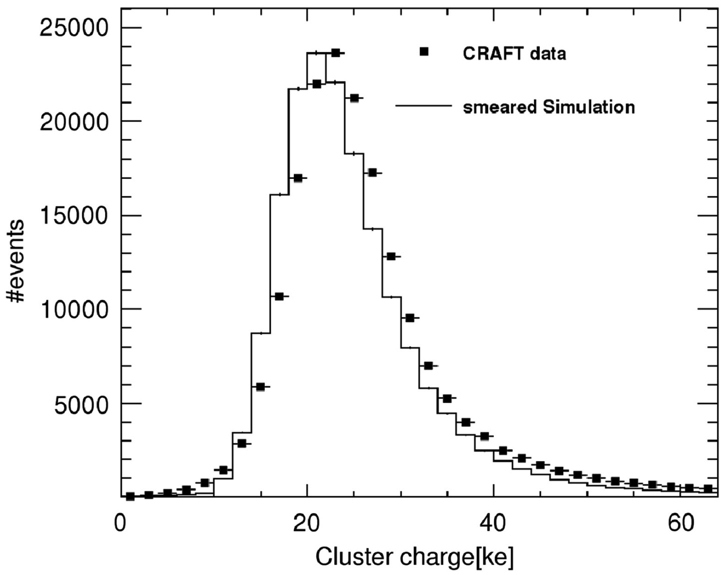

Figure 3.5: The charge deposition of clusters from cosmic ray muons match well to simulation.

3.3.2 Upgrade

Since it is the subdetector closest to the IP, the pixel detector faces the harshest radiation environment of any of the CMS subdetectors. At a luminosity of 10^{34} cm^{-2}s^{-1}, the pixel detector is expected to face an integrated fluence of $\Phi_{eq} = 3 \cdot 10^{14} n_{1MeV}/\mathrm{cm}^2$ per year[1], where Φ_{eq} is the radiation equivalent of N 1 MeV neutrons[12]. This radiation damages both the readout electronics and the silicon sensors. In fact, it was not until

---

[1] At the lower luminosity currently achieved by the LHC the pixel detector is expected to face a total fluence of $\Phi_{eq} = 6 \cdot 10^{14} n_{1MeV}/\mathrm{cm}^2$ after 4 to 5 years.

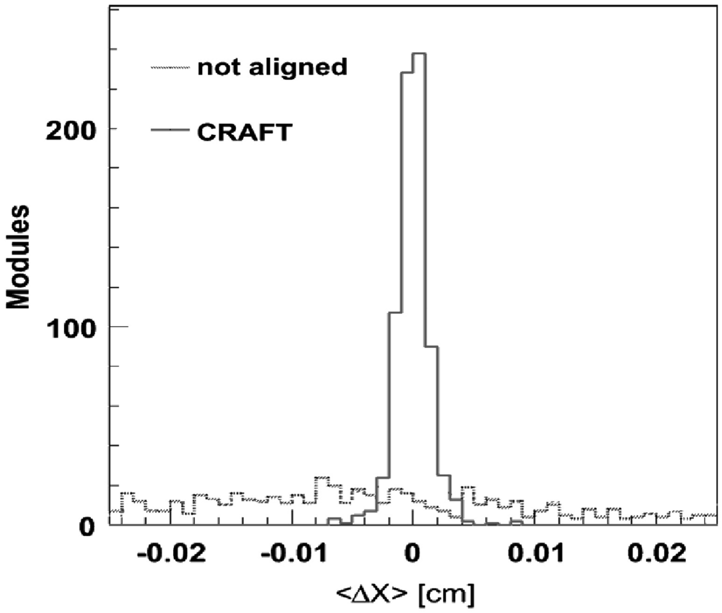

Figure 3.6: The position resolution is determined by the distribution of hit residuals.

the late 1990s that chip technology[2] was sufficiently radiation-hard to be able to endure the radiation at the LHC. As it is, the pixel detector performance will be degraded by radiation before the end of LHC operations and so two upgrades are planned.

The Pixel Phase I Upgrade, originally planned for 2014, is a complete replacement of the pixel detector, adding one additional barrel layer and one additional disk per endcap. The Phase I Upgrade, which is now estimated to be installed sometime around 2016, is foreseen to use mostly the same technology as the previous pixel detector. Later, when the LHC is upgraded to the even higher luminosity Super LHC (SLHC), a Phase II Pixel Detector will be developed. Sensor and electronics technologies for the Phase II Pixel are still being developed.

---

[2] Radiation hardness in chips depends on the feature size of the structures in the chips. Only at a feature size of 0.25 μm and below are the chips tolerant enough for the LHC environment.

3.4 Silicon Strip Tracker

The CMS Silicon Strip Tracker, along with the Pixel Detector, make up the CMS inner tracking system. The Tracker has $\sim$ 200 m^2 of active area and is the largest all-silicon tracker ever built. The strip tracker is divided into several subsystems that were built separately before being integrated at CERN in 2007. The individual subsystems are: the Tracker Inner Barrel (TIB) and Tracker Inner Disks (TID), the Tracker Outer Barrel (TOB), and the two Tracker EndCaps (TEC), with the two endcaps known as TECplus and TECminus. The barrel region has ten layers, four in the inner barrel and six in the outer barrel. The TID has three disks on each side and each TEC has nine disks. Some layers in the barrel and disks in the endcaps contain double-sided "stereo" modules, which have a 100 mradian angle between the sensors on each side, provide two dimensional position information[12]. In total, the strip tracker has 9.3 million readout channels.

3.4.1 Track Reconstruction

As charged particles pass through the tracker, signals are detected in each layer. These "hits" must be then reconstructed into tracks. As there can be at design luminosity over 1000 tracks per event, a pattern matching algorithm is used to associate hits into tracks. There are four steps in the CMS track reconstruction algorithm: seeding, pattern recognition, outlier rejection and final fit, and quality filtering[13].

The track seeds are "proto-tracks" containing at least two hits in the pixel detector that are in a position compatible with the interaction point. The excellent spatial resolution of the pixel detector makes the seeds used by the CMS tracking system very high quality. The pattern recognition algorithm uses a combinatorial Kalman filter to find tracks, which starts with the seed and extrapolates the trajectory through the layers choosing the hits that result in the best χ^2 value between the predicted track and measured value. Several candidates are fit simultaneously to resolve ambiguities. The third step is to remove outliers from the candidate tracks and choose the best fit track. The last step is to reject tracks that are likely fake tracks by examining the number of hits, χ^2 between the fit and the p_T, and the location of the reconstructed vertices.

3.4.2 Tracking Performance

The tracking efficiency and p_T resolution can be determined using the decay process $J/\Psi \rightarrow \mu^+\mu^-$[13]. Tracking efficiency can be determined by the use of a tag-and-probe method with the tag requiring high quality identification of the muon and the probe requiring detection only by the muon system. A probe is consider to pass if the probe matches a reconstructed track from the tracker. The measured efficiency is then $\varepsilon =$(number of passing probes)/(number of passing probes + failing probes). Results are shown in Figure 3.7 with tracking efficiency for muons being $98.8 \pm 0.5\%$. The small width of the J/Ψ mass resonance ($\Gamma(J/\Psi) \sim 90$ keV) allows for the p_T resolution to be expressed as a function of the kinematics of the muons tracks and is shown in Figure 3.8. The p_T resolution is better than 2% in the barrel regions and 3% in the endcaps.

3.5 Electromagnetic Calorimeter

The CMS Electromagnetic Calorimeter (ECAL) is a hermetic high precision scintillating crystal calorimeter[14]. The ECAL is divided into a barrel region and two endcaps. The barrel is constructed from 61200 lead tungstate ($PbWO_4$) crystals and covers the region $|\eta| < 1.48$, while each endcap contains 7244 crystals and covers the

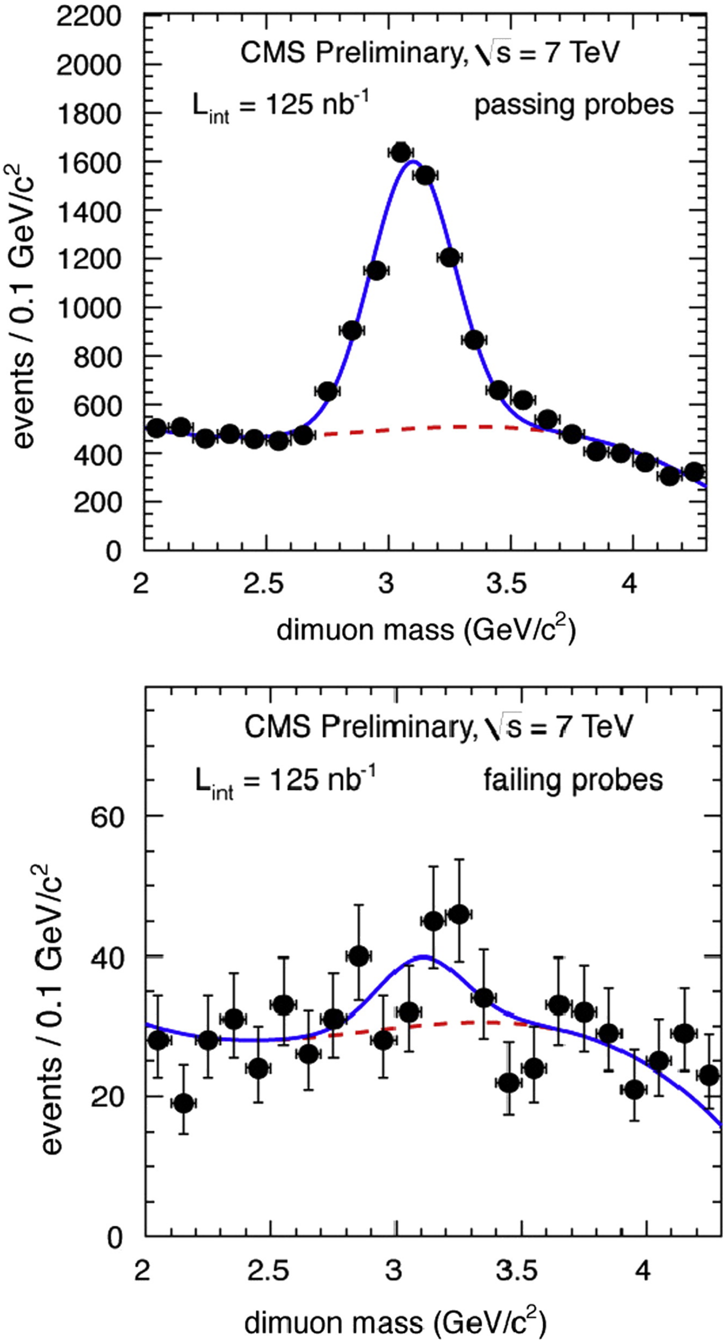

Figure 3.7: The di-muon mass distribution for passing and failing probes using $J/\Psi \rightarrow \mu^+\mu^-$decays.

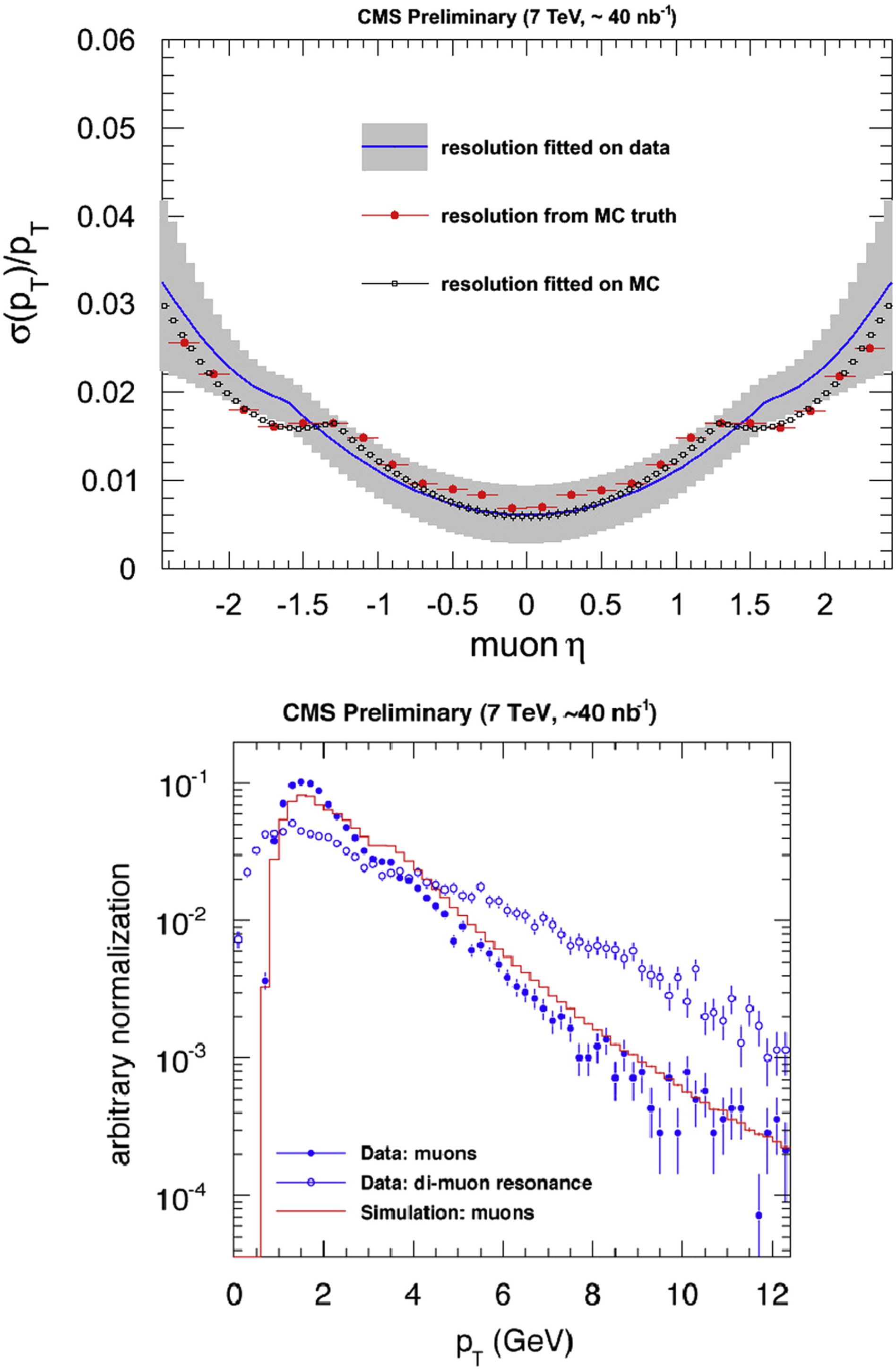

Figure 3.8: The p_T resolution for tracks in the silicon strip tracker is shown using $J/\Psi \to \mu^+\mu^-$decays.

region $1.48 < |\eta| < 3.0$. The crystals in the barrel are grouped into "supermodules" containing 1700 crystals each, and the crystals in the endcaps are grouped into smaller "supercrystals" containing 25 crystals. The structure of the ECAL, showing supermodules, supercrystals, and the preshower detector, described later in the text, can be seen in Figure 3.9.

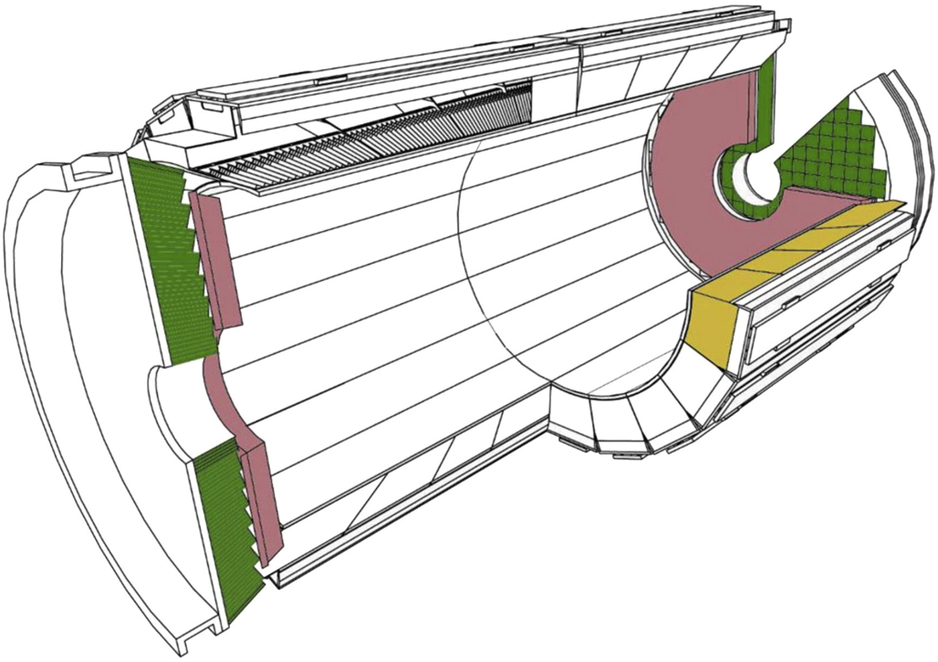

Figure 3.9: The structure of the CMS ECAL. Supermodules can be seen in the barrel region and supercrystals are seen in the endcaps. The Preshower radiators are seen in front of the endcaps.

Lead tungstate is a dense, fast, and radiation tolerant scintillating crystal. Its density reduces the radiation length and therefore the size of the calorimeter. The scintillation rate allows for 80% of the energy to be collected with the LHC's 25 ns bunch spacing. Radiation effects can change the transparency of the crystals, but the crystals recover from this effect when radiation ceases. Since lead tungstate does not produce large amounts of light and has a temperature dependance of 2.2%/°C, avalanche photo-diodes (APD) are used to boost the signal in the barrel. In the endcaps, radiation resistant photo-triodes are used. The barrel APDs are operated at a gain of 50 and also have a large temperature dependence with a temperature coefficient of -2.4%/°C[15]. Due to the thermal dependance on the signal, and therefore the measured energy, the ECAL must be kept at a constant temperature to within 0.1°C.

3.5.1 ECAL Spikes

During operation in 2010, anomalous high energy deposits were observed in the ECAL barrel. These signals do not come from deposits in the crystals but are rather thought to be due to the interaction of particles with the APDs themselves. These signals can effectively mimic high energy photons, causing erroneous triggering and presents a problem during analysis. To identify and reject these "spikes" various methods of detection are used. The ECAL spikes generally appear in one or two crystals so two different algorithms to identify this signature are commonly used to reject spikes.

To determine the presence of an ECAL spike a 3×3 "cluster" of crystals is examined, where the crystal with the highest energy, or "seed crystal", is located at the center. The "Swiss Cross" method computes the value 1-(energy in the four neighboring crystals/energy in the seed crystal). The e2/e9 method computes the ratio of the sum of the two highest energy crystals (e2) to the total energy of the cluster (e9). The two methods are illustrated in Figure 3.10. The recommendation for both methods is to reject the cluster if the computed value is ≥ 0.95.

3.5.2 Preshower

Of all the physics to be done at the LHC, perhaps the most notable is the search for the Higgs boson. The physics channel with the best chance for detection

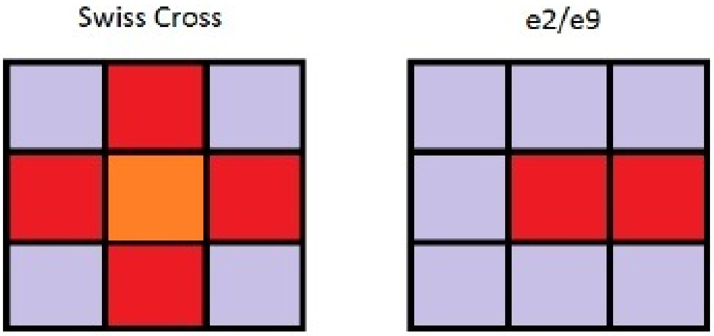

Figure 3.10: The two common spike cleaning methods. On the left, the “Swiss Cross” method uses the seed crystal and its four neighbors. On the right, the e2/e9 method compares the two highest energy crystals to the total energy.

of a low mass Higgs is the process $H \to \gamma\gamma$. There are several processes that produce background to the $\gamma\gamma$ final state from the Higgs decay. Neutral pions (π^0) are commonly produced in proton collisions and decay into closely spaced photons. These photons are so closely spaced that the granularity of the ECAL endcap is not sufficient to resolve them individually. Therefore, a preshower detector was designed to perform π^0 rejection.

The CMS Preshower detector is comprised of two lead radiators and a two-layer silicon detector placed between the interaction point and each ECAL Endcap. The radiators are two and one radiation lengths thick, respectively. The silicon detectors have one layer with vertical strips and one layer with horizontal strips to be able to locate particles in the X-Y plane. As photons or electrons strike the lead radiators, an electromagnetic shower occurs, which is measured by the silicon detectors. The presence of the lead radiators affect the energy measurement by the ECAL; however, the energy loss in the lead is proportional to the energy measured in the silicon detectors, so a correction can be applied to the ECAL deposits.

3.6 Hadronic Calorimeter

The CMS Hadronic Calorimeter (HCAL) is used to measure the energy of hadronic jets and is necessary to compute E_T^{miss} due to neutrinos or possible exotic particles that escape undetected. The HCAL is comprised of four subsystems[9]: the HCAL Barrel (HB), the outer calorimeter (HO), the HCAL Endcap (HE), and the forward calorimeter (HF).

The HB is a sampling calorimeter that covers the range $|\eta| < 1.3$, however the barrel size is restricted due to its position inside the CMS solenoid and requires an additional calorimeter to measure the energy that passes through the HB. The HB is divided into 36 wedges aligned parallel to the beamline. Each wedge is made of brass and steel absorber plates with a plastic scintillator. The wedges overlap in a configuration that creates no dead areas.

The HO sits outside the CMS solenoid and serves to measure any energy that passes through the barrel. The HO uses the solenoid coil as an additional absorber. The HO is divided into five rings with differing absorber thicknesses with the central ring being the smallest. As shower energy that passes through the HB is not measured, this directly affects the measurement of E_T^{miss}. The presence of the HO to measure this additional energy can improve the E_T^{miss} measurement for events with high p_T jets, commonly produced by QCD.

The HE covers a large portion of the solid angle, $1.3 < |\eta| < 3$, which sees $\sim 34\%$ of the particles produced in the final state. The HE must have high radiation tolerance, with 10 Mrad expected after 10 years of operation. It also must be non-magnetic due to its position in the solenoid, leading to the all-brass design. The absorber is designed to minimize the gaps in coverage between the HB and HE creating a hermetic detector.

The HF experiences the harshest radiation environment and therefore requires an extremely radiation tolerant material. The active material chosen is quartz fibers that generate Cherenkov light. The fibers are mounted in grooves in the steel absorber plates. The inner part of the HF will be exposed to close to 100 Mrad/year. As the absorber will become radioactive the entire HF can be moved into a "garage" to limit exposure of personnel during maintenance periods.

3.7 Muon System

The CMS muon system[9] uses three different types of detectors to detect muons. In the barrel region, Drift Tubes (DTs) and Resistive Plate Chambers (RPCs) are used, while in the endcap there are Cathode Strip Chambers (CSCs) and also RPCs. All of the these detectors use gas-filled chambers that collect charge from ionization trails created by charged particles. The CMS muon system has a very high efficiency, as shown in Figure 3.11, except for the regions between the two DT wheels at $|\eta| = 0.25$ and 0.8, and at the transition between the DTs and CSCs. The p_T resolution varies between 9 and 40% depending on muon p_T and $|\eta|$. Combining information from the tracker improves the p_T resolution to about 5% at the cost of some loss in efficiency.

3.7.1 Drift Tubes

In the central region of CMS, $|\eta| < 1.2$, the muon system consists of four concentric cylinders containing 250 gas drift chambers. Each Drift Tube is filled will a mix of 85% Argon and 15% CO_2 with active wires for charge collection. As muons pass through the gas they leave an ionization trail. The charge drifts to the wires, which

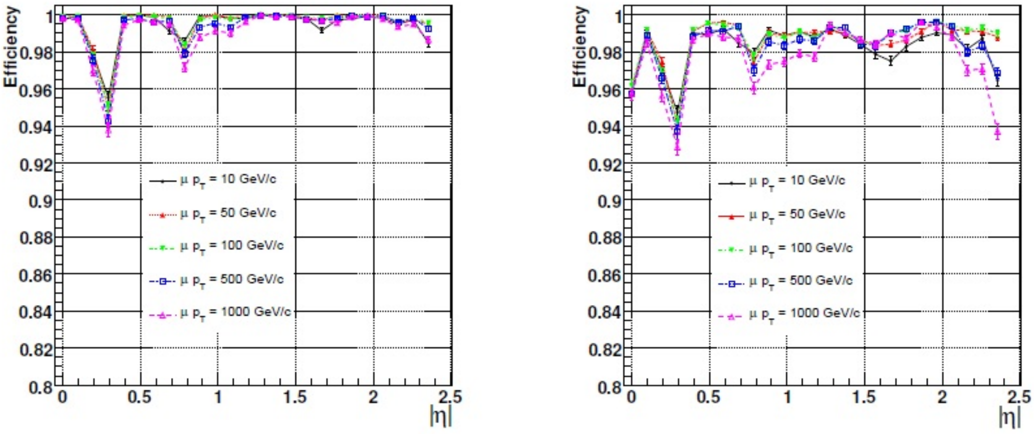

Figure 3.11: Muon reconstruction efficiency is shown as a function of η for several values of p_T. On the left is the standalone muon efficiency using only the muon system. On the right is the global muon efficiency using both the muon system and the tracker. It is important to note that while the standalone reconstruction has better efficiency, the global muons have better p_T resolution.

detect the charge. The size of the drift cell was chosen so the maximum drift time is 380 ns. There are ∼172000 active wires in the entire system. The use of DTs is only possible in this region due its low magnetic field.

3.7.2 Cathode Strip Chambers

In the endcap, the muon system is comprised of Cathode Strip Chambers (CSC). The CSCs are multiwire proportional chambers with six anode wire planes interleaved between seven cathode panels. The overall area covered by the CSC system is over 5000 m^2 with approximately two million wires. The CSCs are used in the endcap because the high muon rate and high non-uniform magnetic field makes other technologies, such as DTs, impossible.

3.7.3 Resistive Plate Chambers

Complementing the DTs in the barrel region and the CSCs in the endcap, are the Resistive Plate Chambers (RPC), which are gaseous parallel plate detectors. The RPCs have fast time resolution and are able to discern an ionizing particle within the 25 ns between events. However, the RPCs have coarser position resolution making them more useful for the trigger. The RPCs are also used to resolve ambiguities in track reconstruction that arise using only the DT or CSC systems.

3.8 Trigger System

At the design luminosity of the LHC the event rate is approximately 40 MHz. Since it is not possible to record events at this rate, a two-part trigger system, consisting of a hardware-based trigger (Level 1) and a software-based trigger (High Level Trigger) is used[16, 9]. The rate is then reduced by a factor of 10^6 to rates less than 100 kHz.

3.8.1 Level 1 Trigger

The Level 1 Trigger (L1T) is a hardware-based system implemented using custom developed Field Programable Gate Array (FPGA) technology. The L1T must be able to process events and make triggering decisions at the full LHC event rate of 40 MHz. The L1T capabilities are limited by the Front End (FE) electronics ability to store event information coming from the subdetectors. The FE electronics can store information from up to 128 consecutive events, which equates to $\sim 3\mu$s. The L1T must obtain event information from the subdetectors and make a decision within this interval. To cope with this time limitation the L1T uses only partial information, with coarser granularity and lower resolution in its decision. The L1T architecture is shown in Figure

3.12. The L1T reduces the overall rate by a factor of 400.

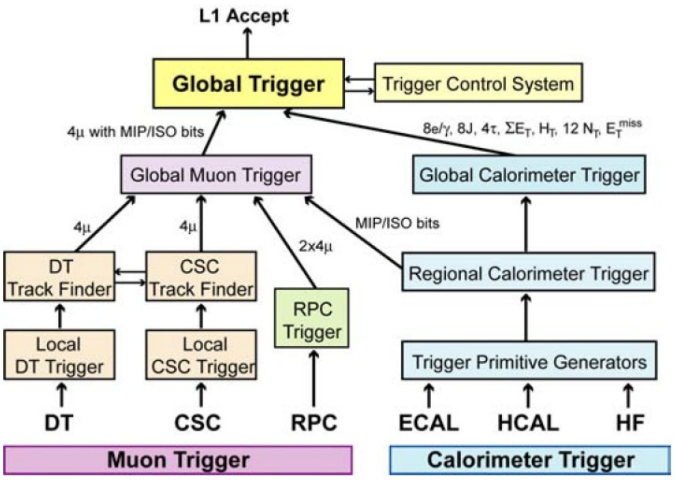

Figure 3.12: The Level 1 Trigger uses information from the calorimeters and muon system to reduce the overall event rate by a factor of 400.

3.8.2 High Level Trigger

Events passing the L1T are then processed by the High Level Trigger (HLT) system. The HLT is software-based, using a computing farm with over 1000 commercial processors. The HLT must reduce the overall event rate by an additional factor of 1000. Unlike the L1T, the HLT uses the complete event to make its decision. The HLT algorithms require on average 10 ms to complete and with an event size of approximately 1 MB the computing farm must sustain data transfer rates of 100 GB/s.

Chapter 4

Tracker Detector Control Systems

The CMS Tracker has very large supporting systems that power and monitor the detector. These systems include CAEN power supplies, programmable logic controllers (PLC), temperature and humidity sensors, and others. The Tracker Detector Control System (DCS) was developed to integrate the many disparate systems of the CMS Tracker into a single coherent interface as well as providing automated systems of monitoring and control that help ensure the safety of the detector. The Tracker DCS is a huge project and a full description of the project is beyond the scope of this thesis. More information is available in [17, 18]

The development of the Tracker DCS began in 2005 and continues today with a team of developers supporting and expanding functionality as need dictates. The DCS system runs with the CMS experimental network at Point 5. There are 11 PCs running Microsoft Windows XP that perform different control and monitoring tasks. The DCS system was created using a Supervisory Control and Data Acquisition (SCADA) system. The SCADA system that was chosen by CERN for the LHC is known as PVSS (Prozess-Visualisierungs-und-SteuerungsSystem), thus all LHC experiments use PVSS as do some

LHC control systems. PVSS was originally developed by ETM, an Austrian company. In 2007, ETM was acquired by Siemens and PVSS was renamed SIMATIC WinCC Open Architecture, although at CERN as well as in this thesis, it is still commonly called PVSS.

4.1 PVSS

The PVSS application is comprised of several different programs, known as "managers," which each perform specific tasks including event handling, data storage, and communication. These managers interact with each other, even across multiple systems, allowing for a distributed architecture[19]. The structure of this interaction is illustrated in Fig. 4.1. The distributed architecture of PVSS makes it well suited to large scale systems as are found at the LHC and is one of the most important factors in CERN's decision to use PVSS for its control systems.

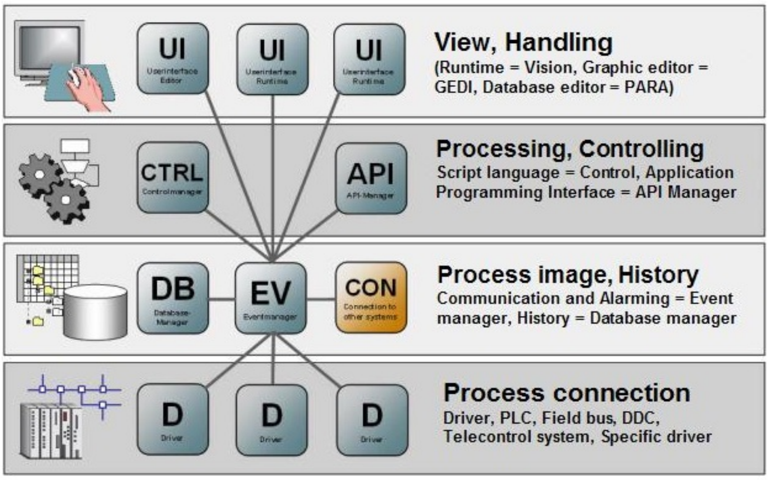

Figure 4.1: The PVSS architecture.

A short description of the PVSS managers follows:

- Event Manager - Handles all event processing, including data requests and callback subscriptions.
- Data Manager - Interfaces to the PVSS internal database. Performs all storage and retrieval tasks.
- Distribution Manager - Coordinates connections between distributed systems.
- Control Manager - Runs user-defined scripts that have no user interface.
- User Interface - Presents graphical panels and performs user-driven operations.
- Driver - Interface layer between PVSS and different hardware systems.

4.1.1 PVSS programming

PVSS is an event-driven system. PVSS programs are either "Panels," which connect functionality to a graphical user interface or "Control Scripts," which execute functions in the background with no user interaction. The heart of the PVSS structure are the "datapoints". Datapoints are similar to C struct objects, having members (in PVSS called elements) of varying types, but unlike in C, the datapoints are permanently stored in an internal database.

In addition to data values stored in the datapoints, one can attach "configs" to individual elements. There are different types of configs that add automatic functions to the datapoint elements. Some of the most commonly used configs are: alert handing, address (interface to hardware), archiving, and datapoint functions (arithmetic functions applied to one or more values).

Alert handling configs allow for user defined alarms to be raised in case a value moves beyond normal operating limits. Alerts can be defined as boolean or analog alerts with the latter allowing for up to five levels of severity. Alerts can be grouped so that multiple alerts are combined into a single alert. This is known as a summary alert and is useful to keep the number of alerts to a manageable level, even in the case of cascade failures.

Address configs work in conjunction with a PVSS driver to provide an interface with experimental hardware. For each address config, a driver and address is selected, thus mapping a hardware parameter to a specific datapoint element. Addresses can be configured for input or output.

Archive configs allow for changes of values over time to be stored to a local or remote database (ORACLE). Archiving can be configured to record different types of changes from the simple old/new comparison to more advanced filtering using "deadbands." A deadband is a range of change from the original value, absolute or relative, that is allowed without triggering the new value to be written to the database. In this way the rate of data sent to the database can be limited and noise arising from the sensitivity of the hardware can be ignored.

Datapoint functions (dpFunctions) are arithmetic functions that take one or more other datapoint elements as inputs and return a result. Datapoint functions are automatically triggered each time the value of an input datapoint element changes. This is particularly useful for converting raw values from hardware to engineering units and also for computed values such as dew points which are derived from the temperature and relative humidity.

4.1.1.1 Control Programming

The programming language of PVSS is known as "Control" (Ctrl). Ctrl is a C-like language with data structures specific to PVSS. Ctrl is a very type-safe language, allowing transparent conversions between compatible types. Also, variable allocations are handled dynamically without requiring specific memory allocation.

4.1.2 JCOP

The Joint Controls Project is an effort at CERN to produce a framework of PVSS panels and scripts to perform common tasks that are required in all experiments. The elements of the JCOP framework used by the Tracker DCS are:

4.1.2.1 CAEN System

The JCOP framework provides a set of tools for communicating with and configuring CAEN power supplies. The JCOP CAEN package provides a tool that creates all datapoints, assigns hardware addresses, and sets up basic alert structures. Example control and monitoring panels are also provided, some of which were integrated directly into the Tracker DCS.

4.1.2.2 Finite State Machine

In order to provide a common user interface for all the disparate subdetectors and DCS systems, a Finite State Machine (FSM) was developed as part of the JCOP Framework and is used as the primary control interface for all of CMS. The CMS FSM is a hierarchal structure of nodes where each node represents some partition of the detector. This partition can be as large, at the upper nodes, as an entire subdetector or as small, at the bottom of the hierarchy, as a single power supply.

In the FSM, commands are propagated down the tree, with each node passing the command to each of its children and each child passing to its children down to the bottom of the branch. The lowest levels of the tree almost always represent a hardware device, these nodes are called "device units". As each device changes its state, e.g. OFF to ON, as a result of a command issued though the FSM or any other cause, the FSM node will reflect the new state. Higher level nodes summarize the states of its children, in effect, having the state propagate up the tree. The state and command structures are independent, therefore the state is not assumed after a command is given.

4.1.2.3 Alert Handling

The JCOP alert handing system provides a set of tools for creating and managing alerts. Several different alert types are available. The simplest alert type is the binary alert is configured to trigger on a true or false condition. Non-binary or analog alerts allow for up to five user defined ranges. Each range can be assign an alert class which specifies the displayed color, the priority rating, and whether a user acknowledgement is required.

4.1.2.4 RDB Archiving

The PVSS RDB archiving features allows values, read out from hardware devices or computed internally, to be be stored in an ORACLE database. To reduce the rate at which data are written to the database, several different methods of filtering may be applied, such as "deadbands", which only allows changes that exceed chosen absolute or relative difference from the original value.

4.1.2.5 Cooling and Ventilation

The Cooling and Ventilation package provides an "out of the box" solution for configuring communication with cooling PLCs. The CERN EN-CV group can provide a file with the description of all readable and writable parameters, which can be read by the Cooling and Ventilation software and used to configure the PVSS system.

4.1.2.6 Configuration Database

The Configuration Database allows any number of PVSS datapoints, configs, and values to be stored in an ORACLE database and then restored to a PVSS system. This provides a simple method for making backups to be restored in case of system failures. In addition to complete configurations, a subset of this information containing only commonly changed values and alert limits can be stored as a separate “recipe”, to be loaded as necessary.

4.1.2.7 Majority

The Majority voting system is used to provide more intelligent state summary information than can be computed by the FSM alone. Using this system, each device (power supply channel, cooling valve, etc.) can be summed individually and the summary state changed based on the percentage of devices in a given state. Using the FSM alone, one could not differentiate between a state change for a single device or multiple devices.

4.2 Tracker DCS Architecture

The CMS Tracker DCS is a distributed system running on 10 PCs running Windows XP and provides all monitoring and control functions for the CMS Silicon Strip Tracker and CMS Pixel Detector. These PCs are located underground at Point 5 and operate on the CMS experimental network. The different DCS systems are arranged by task, with five systems for the power system, two for readout and programming of the PLCs, one for communication with the Tracker cooling plants, one for readout of

PVSS[1] temperatures and voltages, and one supervisor that provides a top level interface for the other systems.

4.2.1 Installation

There are really two aspects of the Tracker DCS: software and configuration. The DCS software consists of packages, described in section 4.2.1.1, which can be updated easily, without interfering with Tracker operation. The configuration contains all the datapoints, configs, and other static structures. These structures reflect the hardware configuration and are changed infrequently.

4.2.1.1 Software Packages

All of the software comprising the Tracker DCS is organized into separate packages. These packages are defined by the functionality they encompass. A comprehensive list of Tracker DCS packages is shown in Table 4.1. The packages are stored in the Subversion (SVN) source control system. The packages are installed in the production by web based interface which retrieves the latest version of the package from SVN and deploys it to all the systems where it is required.

4.2.1.2 Construction DB

In order to construct the Tracker DCS, an ORACLE database was designed to contain the necessary information about the layout of the CMS Tracker and its supporting systems. This database, known as the "Construction DB", was arranged in a "first principles" approach, by which all elements, logical and physical, were defined. Con-

---

[1] The Detector Control Unit (PVSS) are chips integrated into each silicon module and are able to measure individual module temperatures and voltages. Unlike other read out data, the DCU data is retrieved by the Data Acquisition (DAQ) system. There are over 100000 PVSS values read out for the Tracker.

Table 4.1: DCS Packages.

Name	**Functionality**
CMS_TRACKER_BASE	Config DB Datapoint Types for , FSMs, Installer panel
CMS_TRACKER_CAEN	Datapoint Types for PS
CMS_TRACKER_CP	Cooling
CMS_TRACKER_PLC	PLC Datapoint types
CMS_TRACKER_DCU	DCU Datapoint types
CMS_TRACKER_CRONJOBS	Scripts and Datapoint types for Cronjobs
CMS_TRACKER_GENERAL	All scripts, libraries, and UI panels
CMS_TRACKER_INSTALL	Script to initiate installation from Configuration DB

straints were placed on the tables to provide that the data is self-consistent. Database views were then made to show the information in a format that easily translates to the DCS structures. For example, one subsection of the tracker, the Tracker Inner Barrel, contains 40 cooling loops. Each cooling loop has either two or four associated temperature probes. The silicon modules near each cooling loop, are powered by several power supplies. In case the temperature exceeds safe limits, the power is interrupted by the opening of “interlock” relays. Information from different tables are combined to create the complex mapping between detector elements, power supplies, probes, and relays. If this mapping is incorrect, the detector could be damaged as the power would not be cut as temperatures reached dangerous levels.

4.2.1.3 Configuration DB

The DCS computers used for the live production system at the CMS site are not allowed to be accessed directly by the developers. This tight control helps protect the systems from inadvertent corruption. In order to allow for easy deployment and maintenance of the DCS system, while respecting the CMS policies, a methodology was developed by which all updates are performed using the Configuration Database. The procedure for creating and deploying the DCS system, illustrated in Fig. 4.2, is as follows.

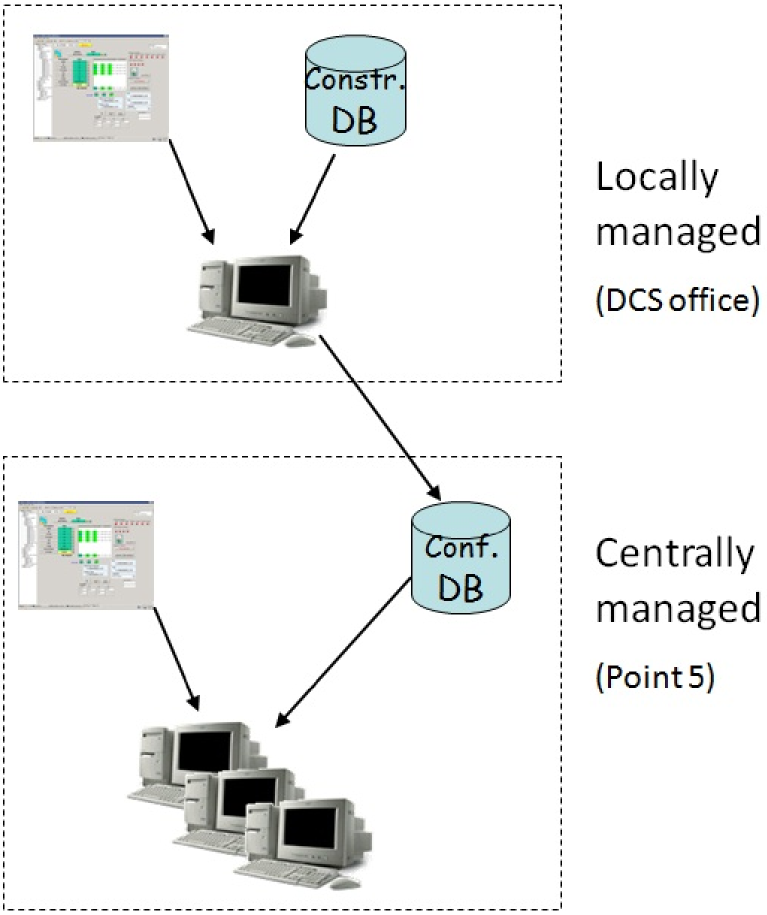

Figure 4.2: The DCS systems are first created on local systems then saved to the Configuration DB. After a system is saved, it can be deployed to the production system.

To build a DCS system, the Tracker DCS PC Installer (Fig. 4.3) is used. The installer can identify the type of system by its entry in the Construction DB or a type can be selected manually. The installer uses the definitions from the Construction DB to define all connections to hardware, logical control structures, and Each system is built first in a test environment and examined to verify the installation was successful. Once satisfied that the constructed system is valid, its image is saved to the Configuration DB. This image can then be restored to the production system. This procedure assures that in case of a PC failure, a DCS PC can be recovered quickly, minimizing downtime to the experiment.

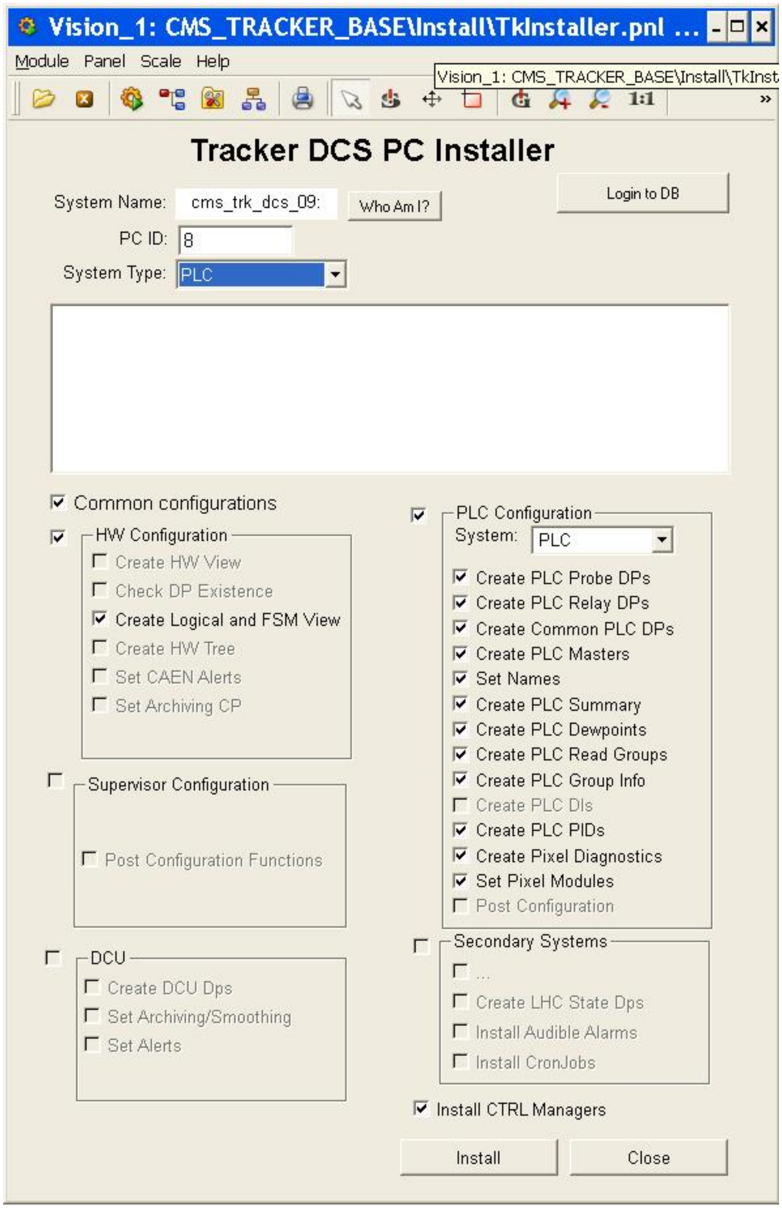

Tracker DCS PC Installer

System Name: cms_trk_dcs_09:
PC ID: 8
System Type: PLC

☑ Common configurations
☑ HW Configuration
- ☐ Create HW View
- ☐ Check DP Existence
- ☑ Create Logical and FSM View
- ☐ Create HW Tree
- ☐ Set CAEN Alerts
- ☐ Set Archiving CP

☐ Supervisor Configuration
- ☐ Post Configuration Functions

☐ DCU
- ☐ Create DCU Dps
- ☐ Set Archiving/Smoothing
- ☐ Set Alerts

☑ PLC Configuration
System: PLC
- ☑ Create PLC Probe DPs
- ☑ Create PLC Relay DPs
- ☑ Create Common PLC DPs
- ☑ Create PLC Masters
- ☑ Set Names
- ☑ Create PLC Summary
- ☑ Create PLC Dewpoints
- ☑ Create PLC Read Groups
- ☑ Create PLC Group Info
- ☐ Create PLC DIs
- ☑ Create PLC PIDs
- ☑ Create Pixel Diagnostics
- ☑ Set Pixel Modules
- ☐ Post Configuration

☐ Secondary Systems
- ☐ ...
- ☐ Create LHC State Dps
- ☐ Install Audible Alarms
- ☐ Install CronJobs

☑ Install CTRL Managers

Figure 4.3: The DCS PC Installer can build any of the different types of DCS systems. Each PC type has its own set of default options. PC types can be automatically determined by system name or can be manually selected.

When a system is saved to the Configuration DB, all the datapoints are retrieved from the PVSS system and their contents and descriptions are saved into the OR-

ACLE database. Previously saved values remain in the database as a historical record, from which previous configurations can be recovered. In the Tracker DCS scheme, each DCS system has a separate stored configuration, from which some or all of the datapoints can be restored. It is also possible to retrieve only specific parts of a configuration, such as only address configs or only stored value data. This flexibility allows the Configuration DB to be used, not just for installation, but for updates as well.

In the case that a change is required to the hardware configuration, the change can be made to a local copy of the DCS and then saved to the Configuration DB. To facilitate this type of operation, a tool was developed. The Configuration DB management tool, provides the ability to view the contents of the database, allows for individual datapoints to be saved, and other manipulation of configuration data. Changes made to the database, even to a single datapoint, can then be restored to the production system.

4.2.2 Control Structures

The CMS Tracker controls are based on the geometric layout of the detector. The tracker is divided into several different parts: the Tracker Inner Barrel (TIB), the Tracker Inner Disc (TID), the Tracker Outer Barrel (TOB), and the Tracker EndCaps (TEC). Each of the subdetectors is separated into two ends, “plus” and “minus”, which refer to their position forward or backward along the beamline. Within each subdetector there are cooling lines that loop through the volume, making thermal contact with the silicon modules. As the greatest danger to the safety of the detector comes from overheating, it makes sense to arrange the power system around the cooling geometry. This way if the cooling fails or is insufficient along a cooling loop, the power in this region can be cut independently.

The next level below the cooling geometry is organized by the power requirements of the readout electronics. Groups of silicon modules are connected to a (CCU), which must be powered before the integrated electronics of the modules. These considerations allow the formation of a control hierarchy which is illustrated in the next sections.

4.2.2.1 Tracker Finite State Machine

The control hierarchies for all the LHC experiments use a Finite State Machine (FSM). The CMS Tracker FSM has at the highest levels nodes representing the six TTC partitions of the Silicon Strip Tracker and the Pixel Detector. These partitions are the TIB, TOB, TECplus, TECinus, PixelBarrel, and Pixel Endcap. Additional nodes for auxiliary systems are also present at this level. The next levels beneath the TTC partitions depend on the geometry of the subdetector. The full Tracker FSM is shown in Fig. 4.4.

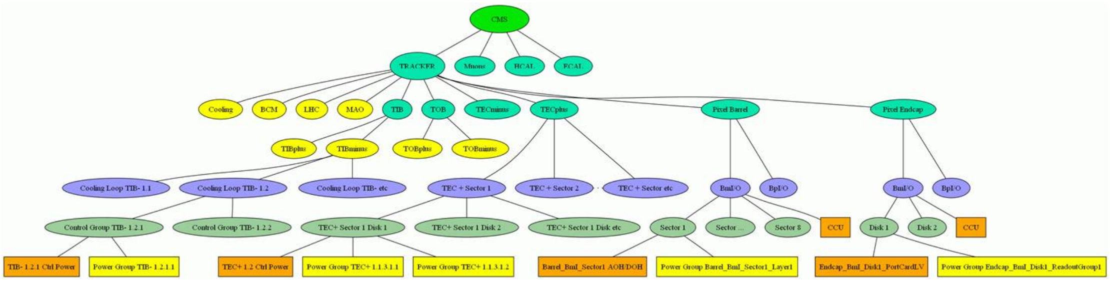

Figure 4.4: The Tracker Finite State Machine.

4.2.2.2 User Interface

The main DCS panel, shown in Fig. **??**, was designed to provide the user with the most commonly used controls and the most important information. Commands are given to the Tracker via the FSM nodes. Commands can be given to the entire tracker or to sub-partitions independently. The current state of each sub-partition is displayed on the FSM node and is also indicated by color. To be able to send commands to the FSM, one must actively take ownership of the FSM tree by clicking on the “lock” icon. Normally, only one user may be the owner of the tree at any time, although the tree may be placed in a “shared” mode.

The state of Tracker is also presented as a percentage of power channels in each state using the Majority system. Percentages for three types of power channels are displayed: high voltage, low voltage, and control power. For each of these types, there are three states: on, off, and error. There are two additional states, ready and not ready, which indicate whether a channel is allowed to be activated based on the current conditions (cooling, beam mode, etc.) The Majority system is configured so the loss of a single channel, which would have a negligible effect on tracking efficiency, does not change the state of the Tracker and stop data-taking.

Communication with hardware must be maintained to have accurate status information and be able to issue commands. To show the user that the system is still communicating, a series of “heartbeats” are displayed. If communication is interrupted, the heartbeat icons will change to “broken” hearts, indicating that there is a problem.

4.2.2.3 Hardware Views

Sometimes, particularly during troubleshooting or maintenance, the logical structure of the FSM is not convenient. In these cases it is commonly more efficient to view and control the hardware, not according to the detector geometry but rather by its location. For this purpose, hardware views[2] were created as an alternate method

---

[2] The CMS DCS group originally suggested the creation of a ”hardware tree”, an FSM hierarchy that is organized by hardware location rather than detector geometry. This idea was rejected by the Tracker DCS group because the size of the Tracker power system exceeds the capabilities of the PVSS FSM.

of control. All of the hardware views were designed to be constructed dynamically, using the hardware definitions to build the panels, allowing changes to the systems to be incorporated automatically.

For the power system, the hardware view that was created is the Power Supply Rack View. The Rack View allows the status of each of the 31 racks to be displayed individually. Racks can be selected by either their physical location in the experimental cavern (balcony, side, rack number) or by their logical location in the power system (mainframe number and branch controller). Each rack contains up to five power supply crates with each crate containing up to 16 power supply units (PSU). The display, shown in Fig. 4.5, shows the current status of each PSU channel by color, indicating off (blue), on (green), interlocked (orange), in error (red), unplugged (grey), or not communicating (purple). The detector element powered by each channel, which serves as an alias for the PSU is displayed as popup text when the mouse cursor is over its representation in the view.

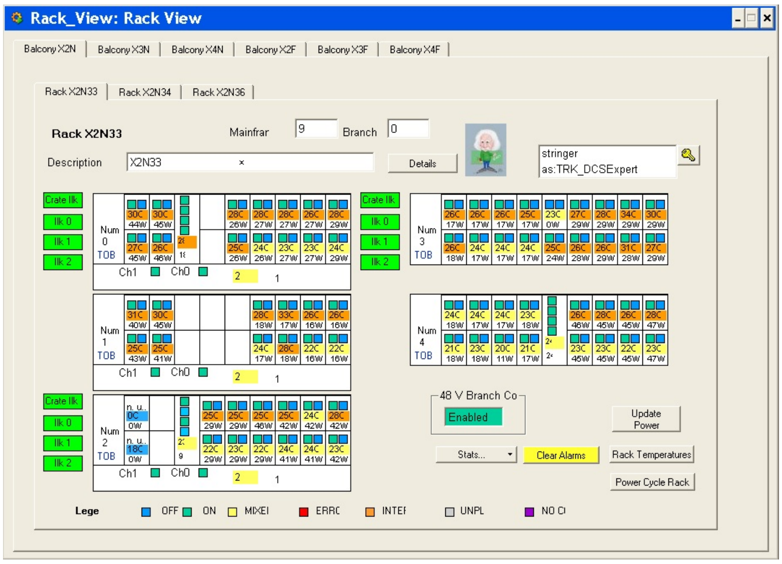

Rack X2N33

Mainfrar 9 Branch 0

Description X2N33

stringer
as:TRK_DCSExpert

Figure 4.5: Power Supply Rack View.

Control via hardware views can be accomplished by clicking on the element you wish to control. Commands can be given to single power channels, entire crates, or the entire rack. As the Rack View does not implicitly implement the powering hierarchy, as does the FSM, safeguards are put into place to warn the user if an operation that would violate the proper sequence is attempted.

The environmental monitoring of the Tracker is performed by the use of over 1000 temperature and relative humdity probes. These probes are connected to eight Siemens Programmable Logic Controllers (PLC). The PLC systems are referred to as the Tracker Safety System (TSS). While the TSS functions independently, the DCS is responsible for communication with and configuration of the PLCs. In order to view the data from each of the PLC systems, a PLC Rack View was implemented (Fig. 4.6).

The PLC View allows the user to view one PLC system at a time, showing the connected modules by their physical position in the rack (row, slot, channel). Different types of modules are represented in the view. Temperature and relative humidity values are displayed in each module. Relay modules, which serve to cut power to (interlock) parts of the detector, show a boolean status of open (red) or closed (green). Unconnected relays are shown in light red and unused analog channels are indicated by a line.

4.2.3 Operational and Monitoring Tools

With over 8000 power channels and more than 10 configurable values per channel, the management of the settings is a challenge. Since different settings are needed for running and maintenance periods, it is useful to allow multiple configurations to be saved.

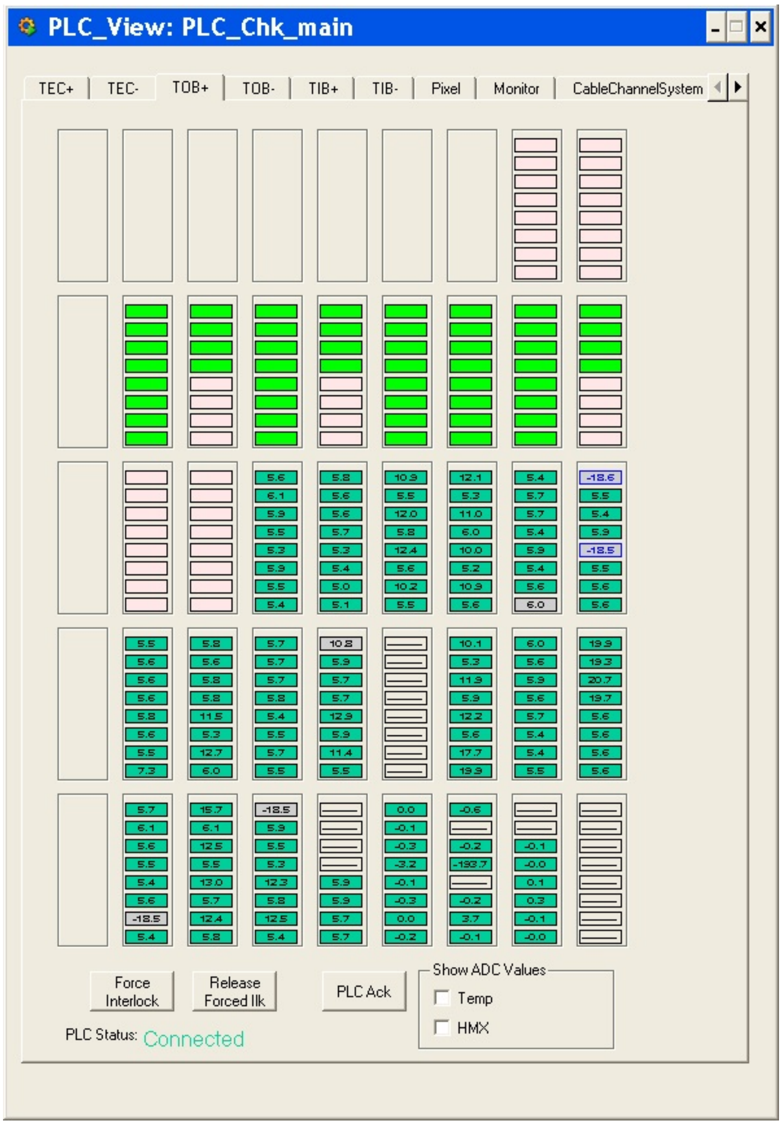

	🟩	🟩	🟩	🟩	🟩	🟩	🟩	🟩
	🟩	🟩	🟩	🟩	🟩	🟩	🟩	🟩
	🟩	🟩	🟩	🟩	🟩	🟩	🟩	🟩
	🟩	🟩	🟩	🟩	🟩	🟩	🟩	🟩
	🟩		🟩		🟩	🟩	🟩	
	🟩		🟩		🟩	🟩	🟩	
	🟩		🟩		🟩	🟩	🟩	
	🟩		🟩		🟩	🟩	🟩	

			5.6	5.8	10.9	12.1	5.4	-18.6
			6.1	5.6	5.5	5.3	5.7	5.5
			5.9	5.6	12.0	11.0	5.7	5.4
			5.5	5.7	5.8	6.0	5.4	5.9
			5.3	5.3	12.4	10.0	5.9	-18.5
			5.9	5.4	5.6	5.2	5.4	5.5
			5.5	5.0	10.2	10.9	5.6	5.6
			5.4	5.1	5.5	5.6	6.0	5.6

	5.5	5.8	5.7	10.8	—	10.1	6.0	19.9
	5.6	5.6	5.7	5.9	—	5.3	5.6	19.3
	5.6	5.8	5.7	5.7	—	11.9	5.9	20.7
	5.6	5.8	5.8	5.7	—	5.9	5.6	19.7
	5.8	11.5	5.4	12.9	—	12.2	5.7	5.6
	5.6	5.3	5.5	5.9	—	5.6	5.4	5.6
	5.5	12.7	5.7	11.4	—	17.7	5.4	5.6
	7.3	6.0	5.5	5.5	—	19.9	5.5	5.6

	5.7	15.7	-18.5	—	0.0	-0.6	—	—
	6.1	6.1	5.9	—	-0.1	—	—	—
	5.6	12.5	5.5	—	-0.3	-0.2	-0.1	—
	5.5	5.5	5.3	—	-3.2	-193.7	-0.0	—
	5.4	13.0	12.3	5.9	-0.1	—	0.1	—
	5.6	5.7	5.8	5.9	-0.3	-0.2	0.3	—
	-18.5	12.4	12.5	5.7	0.0	3.7	-0.1	—
	5.4	5.8	5.4	5.7	-0.2	-0.1	-0.0	—

Show ADC Values
☐ Temp
☐ HMX

PLC Status: Connected

Figure 4.6: PLC Rack View.

4.2.3.1 Configuration Recipes

The Configuration Recipe system provides a method for loading and monitoring the configurable settings for the power system and the PLC safety settings. Two different recipe types are defined, one for the power system and one for the PLC system. Power supply recipes store values for voltages, voltage limits, current limits, and alert settings. The PLC recipes contain temperature limits and alarm settings. In order to keep the recipes to a manageable size, separate recipes are stored for each TTC partion, for the power system, or PLC system. Recipes are currently defined for physics operation and technical stop maintenance periods. During the technical stop periods, the cooling is commonly unavailable thus the temperature alerts must be set higher. In the future, the operating temperature will be lowered which will require a new set of limits, the new limits will be stored as an additional recipe.

Recipes can be loaded using the Configuration node of the FSM or by a Recipe Management expert panel (Fig. 4.7. After a recipe is loaded, a verify process is performed to confirm the new settings were accepted. If there were values that were not accepted, these values are reapplied up to three times. In order to monitor the settings, the verification process is performed automatically every eight hours. If a partition fails this verification, a node in the FSM shows a “NOT READY” state and the partition is indicated in red on the recipe management panel. The recipe management panels shows the last set and saved values of the differing settings, as well as the value read from the hardware, which may be different from either of the other two values[3].

---

[3] A common scenario for settings to be different occurs when malfunctioning PSU modules are replaced. If the new PSU is not reset, its settings may be incorrect and potentially dangerous for the Tracker. In this case, the last set values would be correct but the hardware has the wrong settings.

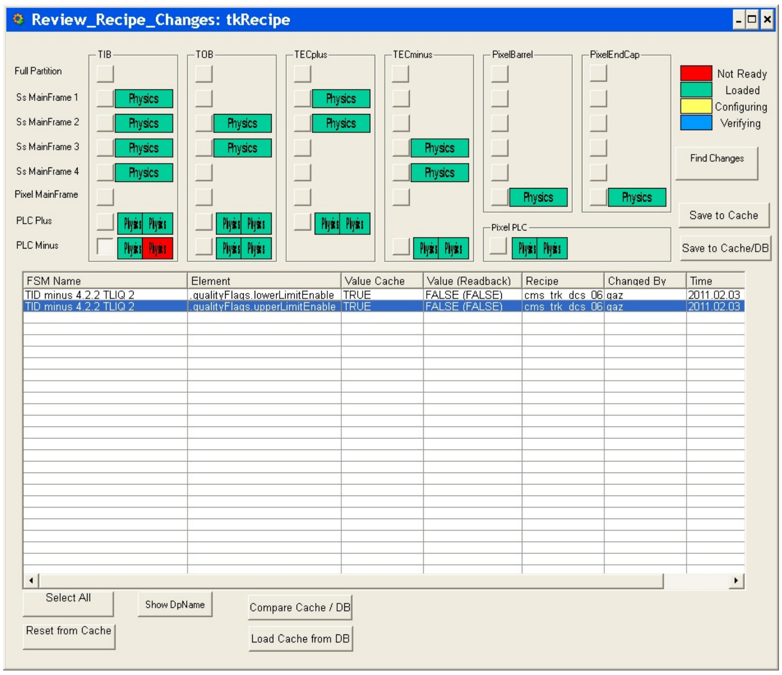

FSM Name	Element	Value Cache	Value (Readback)	Recipe	Changed By	Time
TID minus 4.2.2 TLIQ 2	.qualityFlags.lowerLimitEnable	TRUE	FALSE (FALSE)	cms trk dcs 06	qaz	2011.02.03
TID minus 4.2.2 TLIQ 2	.qualityFlags.upperLimitEnable	TRUE	FALSE (FALSE)	cms trk dcs 06	qaz	2011.02.03

Figure 4.7: Recipe Management expert panel.

Chapter 5

The Standard Model and Beyond

The Standard Model (SM) of particle physics has been remarkably successful in describing the interactions of elementary particles. It describes well three of the four fundamental forces: electromagnetism, the strong force, and the weak force. Only the gravitational force is not incorporated in the SM. In the SM, there three types of elementary particles: quarks, leptons, and gauge bosons. The quarks and leptons, known as fermions because of their half-integer spins, are divided into three generations. The gauge bosons, which have integer spins, act as force carriers and mediate the interactions between particles. These particles are listed in table 5.1.

Table 5.1: The elementary particles of the Standard Model.

	Fermions			Bosons	
Quarks	u	c	t	γ	Force Carriers
	d	s	b	Z	
Leptons	ν_e	ν_μ	ν_τ	W	
	e	μ	τ	g	

5.1 The hierarchy problem

The SM has had many successes in predicting the existence of previously undiscovered particles, such as the W and Z bosons, the top quark, and hopefully the Higgs boson. But it leaves some unanswered questions and inconsistencies that need to be resolved. The SM gauge coupling strengths exhibit "running" by which the strength changes as a function of the energy scale. Examination of the evolution of the couplings suggests that the electromagnetic, weak, and the strong force become unified at high energies; this concept is called the Grand Unified Theories (GUT)[20]. The energy at which unification is thought to occur is called the GUT scale ($M_{GUT} \sim 10^{15} - 10^{16}$ GeV), which is approaching the Planck scale ($M_{Pl} \sim 10^{19}$GeV) where gravity could also be unified.

The SM cannot explain the smallness of the weak scale, which is set by the Higgs mechanism to be $\mu \sim 1/\sqrt{G_F} \sim 250$ GeV, where G_F is the Fermi constant. This inconsistency is called the hierarchy problem. The hierarchy problem is best illustrated in terms of the Higgs boson mass. From perturbation theory we can state that the Higgs mass is $m_h^2 = m_{bare} + \delta m_h^2$, where the m_{bare} is the computed value of the Higgs mass and the first order correction, from the top quark loop (Figure 5.1), is δm_h^2. The correction from the top loop is

$$\delta m^2_{h|top} \sim \frac{3G_F}{\sqrt{2\pi^2}} m_t^2 \Lambda^2 \sim (0.3\Lambda)^2 \tag{5.1}$$

where m_t is the top quark mass and Λ is the energy scale. Because the Higgs mass has this quadratic dependence on the energy scale the Higgs mass diverges at high energy. However, the limits on the Higgs mass set by electroweak precision tests imply that there must be a mechanism that cancels the top loop correction at scales of $\Lambda \sim \mathcal{O}(1$

TeV).

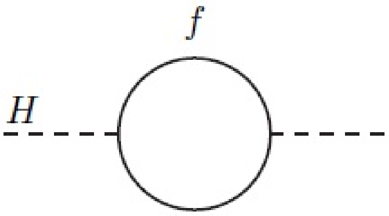

Figure 5.1: The first order correction to the Higgs mass from the top quark loop.

5.2 Supersymmetry

Supersymmetry (SUSY) is a theory that postulates a relationship between fermions and bosons[21]. It suggests that for every SM particle there is a “superpartner” with a spin differing by 1/2. This is accomplished by introducing a supersymmetry transformation such that

$$Q|Boson >= |Fermion > \text{ and } Q|Fermion >= |Boson >, \tag{5.2}$$

where Q is an anti-commuting spinor. The superpartners generated by this transformation would have the same characteristics as their SM counterparts. However, no superpartners have ever been observed. This implies that the superpartners, if they exist, must have a higher mass to have not been detected so far. But since the squared mass operator, $-P^2$, commutes with the operators Q and $Q^\dagger$ then superpartners should have the same mass. To account for this mass difference supersymmetry must be a broken symmetry.

Supersymmetric particles are named after their associated SM particles with quarks and leptons prepending an “s” to the names and bosons adding a suffix “ino.” Some examples of SM particles and their superpartners are presented in Table 5.2.

Table 5.2: Some examples of SUSY partners and nomenclature.

SM Particle	Symbol	Superpartner	Symbol
quark	q	squark	$\tilde{q}$
lepton	l	slepton	$\tilde{l}$
W	W_μ	Wino	$\tilde{W}$
B	B_μ	Bino	$\tilde{B}$
Z	Z^0	Zino	$\tilde{Z}$
Higgs boson	H	Higgsino	$\tilde{H}$

The SUSY theory provides a natural solution to the hierarchy problem by introducing additional contributions to the Higgs mass. The superpartner of the top quark, the stop, also contributes to the Higgs, but since it is a boson it is multiplied by a factor of -1 and exactly cancels the top loop correction (Figure 5.2). However, this is only true if the SUSY breaking terms also do not introduce further divergences. These terms are called “softly-breaking” terms.

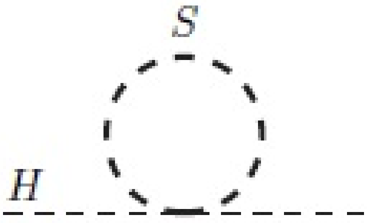

Figure 5.2: The first order correction to the Higgs mass from the (scalar) stop loop cancels the top loop contribution and protects the Higgs mass.

An additional benefit of supersymmetric models is that the presence of the SUSY particles allows for unification at GUT scales. Figure 5.3 shows gauge coupling unification at $\sim 10^{16}$ GeV[22]. Supersymmetric models also have additional consequences. It was shown that in a broken supersymmetry [23] there cannot be tree-level couplings and all communication must be accomplished through a "hidden" sector. Different SUSY models accomplish this communication in different ways, as we will see in the following sections.

Another feature of SUSY models is the conservation of R-Parity. R-Parity is defined as

$$R = (-1)^{2J+3B+L} \tag{5.3}$$

where J is spin, B is baryon number, and L is lepton number. The R-Parity equation implies that all SM particles are $R = 1$ whereas all SUSY particles are $R = -1$. If R-Parity is conserved it has two implications: first that all SUSY particles must be produced in pairs, and second that SUSY particles cannot decay to only SM particles. Therefore, the lightest superpartner (LSP) must be stable. The LSP could then be, depending on mass and production cross section, a candidate for Dark Matter.

5.2.1 Minimally Supersymmetric Standard Model

The most widely used supersymmetric theory is the Minimally Supersymmetric Standard Model (MSSM). The MSSM is the simplest extension of the SM, in which the single particle states of the SM are extended to form *supermultiplets* that contain both fermionic and bosonic states. The MSSM is based on the gauge group $SU(2)_L \times U(1) \times SU(3)_c$ consisting of three gauge superfields, V^a, V, V_s^α and seven left-handed chiral superfields, $H_u, H_d, Q, L, \overline{u}, \overline{d}, \overline{e}$ leading to the particles described in Table 5.3.

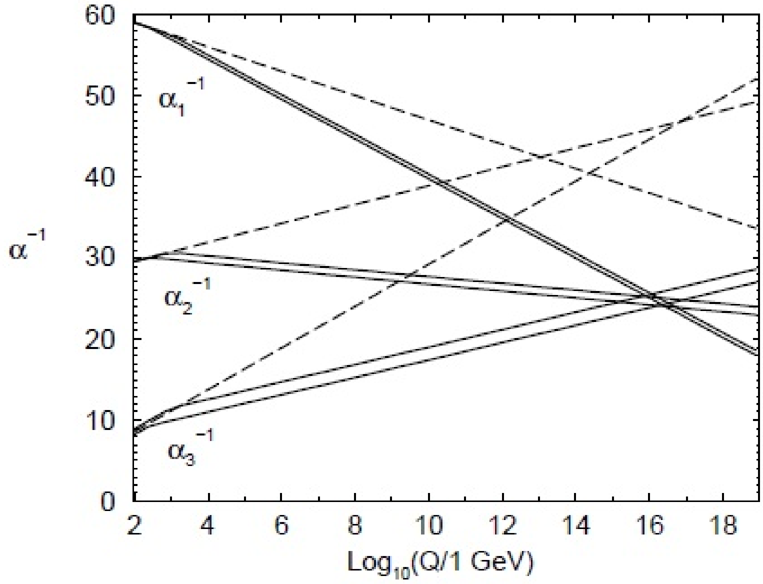

Figure 5.3: The running of the inverse gauge coupling constants α_1^{-1} (electromagnetic), α_2^{-1} (weak), and α_3^{-1} (strong). Dashed lines are for the standard model and solid lines are for the Minimally Supersymmetric Standard Model.

5.2.1.1 SUSY Breaking

SUSY is broken in the same manner as the SM, by the use of a Higgs mechanism. Because the MSSM uses only left-handed superfields, two Higgs doublets are required, one for up-type quarks and one for down-type quarks. This leads to five Higgs bosons and two vacuum expectation values. Additionally, the SUSY breaking terms introduced must be soft. In a general supersymmetric theory, the only possible soft SUSY breaking terms in the Lagrangian are

$$\mathcal{L}_{soft} = -\left(\frac{1}{2}M_a\lambda^a\lambda^a + \frac{1}{6}a^{ijk}\phi_i\phi_j\phi_k + \frac{1}{2}b^{ij}\phi_i\phi_j + t^i\phi_i\right) + \text{c.c.} - (m^2)^i_j\phi^{j*}\phi_i \qquad (5.4)$$

To describe the minimal set of supermultiplets shown in Table 5.3 we can write a superpotential for the MSSM:

Table 5.3: Quantum numbers and particles of each MSSM superfield.

	$SU(2)_L$	$U(1)$	Particles
V^a	3	1	W^a_μ, λ^a, D^a
V	1	0	B_μ, λ, D
L	2	-1	$\begin{pmatrix} \nu_L \\ e_L \end{pmatrix}, \begin{pmatrix} A(\nu_L) \\ A(e_L) \end{pmatrix}, \begin{pmatrix} F(\nu_L) \\ F(e_L) \end{pmatrix}$
$\overline{e}$	1	2	$e_R, A(e_R), F(e_R)$
Q	2	$-\frac{1}{3}$	$\begin{pmatrix} u_L \\ d_L \end{pmatrix}, \begin{pmatrix} A(u_L) \\ A(d_L) \end{pmatrix}, \begin{pmatrix} F(u_L) \\ F(d_L) \end{pmatrix}$
$\overline{u}$	1	$-\frac{4}{3}$	$u_R, A(u_R), F(u_R)$
$\overline{d}$	1	$\frac{2}{3}$	$d_R, A(d_R), F(d_R)$
H_d	2	-1	$\begin{pmatrix} H_1^0 \\ H_1^- \end{pmatrix}, \begin{pmatrix} \tilde{H}_1^0 \\ \tilde{H}_1^- \end{pmatrix}, \begin{pmatrix} F(H_1^0 \\ F(H_1^-) \end{pmatrix}$
H_u	2	1	$\begin{pmatrix} H_2^+ \\ H_2^0 \end{pmatrix}, \begin{pmatrix} \tilde{H}_2^+ \\ \tilde{H}_2^0 \end{pmatrix}, \begin{pmatrix} F(H_2^+ \\ F(H_2^0) \end{pmatrix}$

	$SU(3)_c$	$SU(2)_L \times U(1)$	Particles
V_s^α	8	singlet	$g_\mu^\alpha, \tilde{g}^\alpha, D^\alpha$

$$W_{MSSM} = \overline{u}\boldsymbol{y_u}QH_u - \overline{d}\boldsymbol{y_d}QH_d - \overline{e}\boldsymbol{y_e}LH_d + \mu H_u H_d \tag{5.5}$$

where $H_u, H_d, Q, L, \overline{u}, \overline{d}, \overline{e}$ are the chiral superfields of the chiral supermuliplets of the MSSM. $\boldsymbol{y_u}, \boldsymbol{y_d}, \boldsymbol{y_e}$ are the Yukawa matrices where we assume that only the third generation fermions contribute to the potential and are non-zero.

Adding the soft SUSY-breaking terms, following Equation 5.4, leads to the creation of mass terms for the gluino, Wino, and Bino[21]:

$$\begin{aligned}\mathcal{L}_{soft}^{MSSM} &= -\frac{1}{2}\left(M_3\tilde{g}\tilde{g} + M_2\tilde{W}\tilde{W} + M_1\tilde{B}\tilde{B} + \text{c.c.}\right)\\ &- \left(\tilde{\bar{u}}\boldsymbol{a_u}\tilde{Q}H_u - \tilde{\bar{d}}\boldsymbol{a_d}\tilde{Q}H_d - \tilde{\bar{e}}\tilde{L}H_d + \text{c.c.}\right)\\ &- \tilde{Q}^\dagger\boldsymbol{m_Q^2}\tilde{Q} - \tilde{L}^\dagger\boldsymbol{m_L^2}\tilde{L} - \tilde{\bar{u}}\boldsymbol{m_u^2}\tilde{\bar{u}}^\dagger - \tilde{\bar{d}}\boldsymbol{m_d^2}\tilde{\bar{d}}^\dagger - \tilde{\bar{e}}\boldsymbol{m_e^2}\tilde{\bar{e}}\\ &- m_{H_u}^2 H_u^* H_u - m_{H_d}^2 H_d^* H_d - (bH_uH_d + \text{c.c.}). \end{aligned} \tag{5.6}$$

The mass term for the Wino leads to charged gaugino mixing

$$\mathcal{L} = -\frac{1}{2}M_2\tilde{W}^+\tilde{W}^- - \frac{1}{2}M_2\tilde{W}^-\tilde{W}^+ \tag{5.7}$$

and there is a term for Higgsino-gaugino mixing and the additional Higgs mass parameter μ

$$\mathcal{L}_{HV} = -\sqrt{2}m_W\cos\beta\tilde{H}_d^-\tilde{W}^+ - \sqrt{2}m_W\sin\beta\tilde{H}_u^+\tilde{W}^- \tag{5.8}$$

$$\mathcal{L}_{mass} = -\mu\tilde{H}_1^-\tilde{H}_2^+ \tag{5.9}$$

where $\cos\beta$ and $\sin\beta$ are the vacuum expectation values for the two Higgs doublets. From these equations we can construct a mass matrix

$$X_{\alpha\beta} = \begin{pmatrix} M_2 & \sqrt{2}m_W\sin\beta \\ \sqrt{2}m_W\sin\beta & \mu \end{pmatrix} \tag{5.10}$$

that can be diagonalized to find the physical mass eigenstates, which are the charginos[24]. A transformation between the bases can be defined

$$\begin{pmatrix} \tilde{\chi}_1^\pm \\ \tilde{\chi}_2^\pm \end{pmatrix} = U_{L,R}\begin{pmatrix} \tilde{W}^\pm \\ \tilde{H}^\pm \end{pmatrix} \tag{5.11}$$

where $U_{L,R}$ are two different unitary matrices.

Similarly, the neutral gaugino mass eigenstates, the neutralinos, can be determined. From Equation 5.6 we get the mass terms

$$\mathcal{L} = -\frac{1}{2}M_1\tilde{B}\tilde{B} - \frac{1}{2}M_2\tilde{W}^-\tilde{W}^+ \tag{5.12}$$

and with the mixing terms and Higgs mass term,

$$\mathcal{L}_{HV} = -\sqrt{2}m_W \cos\beta \tilde{H}_d^-\tilde{W}^+ - \sqrt{2}m_W \sin\beta \tilde{H}_u^+\tilde{W}^- \tag{5.13}$$

$$\mathcal{L}_{mass} = -\mu\tilde{H}_1^-\tilde{H}_2^+ \tag{5.14}$$

and we again can define the transformation from weak eigenstates to mass eigenstates[25].

$$\begin{pmatrix} \tilde{\chi}_1^0 \\ \tilde{\chi}_2^0 \\ \tilde{\chi}_3^0 \\ \tilde{\chi}_4^0 \end{pmatrix} = T \begin{pmatrix} \tilde{W} \\ \tilde{B} \\ \tilde{H}_1^0 \\ \tilde{H}_2^0 \end{pmatrix} \tag{5.15}$$

From Eqs. 5.11 and 5.15 it is shown that the chargino and neutralino are mixtures of the gauginos, with the neutralino being a combination of the Zino, Bino, photino, and the Higgsino. The decay modes of these particles are then determine by mixing scenarios. For the neutralino, which is important to this analysis, the possible decay modes are as follows:

$$\tilde{\chi}_1^0 \rightarrow \begin{cases} \gamma + \tilde{G} \\ Z + \tilde{G} \\ H + \tilde{G} \\ e^+e- + \tilde{G} \end{cases} \tag{5.16}$$

5.2.2 General Gauge Mediation

Several variations of the MSSM exist that use different mechanisms of SUSY breaking. In each model, SUSY breaking occurs in a "hidden sector", with only indirect interactions with the visible sector, resulting in the MSSM soft breaking terms (Fig. 5.4). In this analysis, we study the model in which gauge interactions mediate the breaking, which is known as Gauge Mediated SUSY breaking (GMSB)[21]. Specifically our results are presented in terms of General Gauge Mediation.

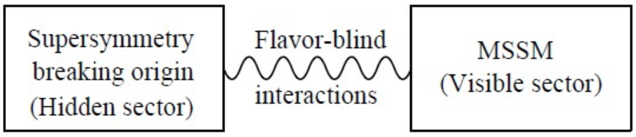

Figure 5.4: SUSY breaking occurs in the hidden sector. Different mechanisms exist by which the hidden and visible sectors interact.

In the simplest form of GMSB the $SU(3)_c \times SU(2)_L \times U(1)_Y$ gauge interactions are responsible for communication with the visible sector, unlike mSUGRA models which use gravity. In GMSB models the gravitational interactions still exist; they are just insignificant in comparison with the gauge interactions. To provide the coupling between the hidden and visible sectors we introduce "messenger" fields. The messengers are an additional set of left-handed chiral supermultiplets $q, \overline{q}, l, \overline{l}$. These messengers must have a large mass to have not been detected. Messenger fields contribute to the MSSM gaugino masses by one loop diagrams with virtual messenger particles (Fig. 5.5).

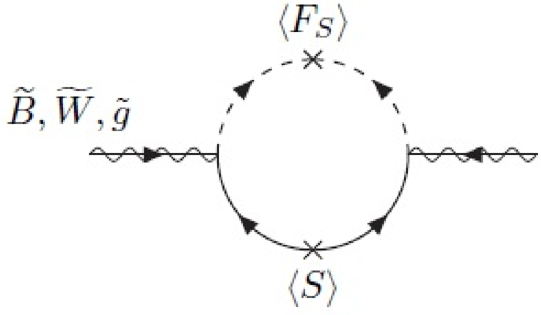

Figure 5.5: Messenger fields interact with MSSM gauginos by one-loop diagrams.

5.2.3 Phenomenology

The distinctive feature of gauge mediated models is that the LSP is the gravitino. This occurs by a "Super-Higgs" mechanism in which, as in the SM Higgs mechanism, a massless Goldstone boson is created due to symmetry breaking. Due to gravitional interactions, the "Goldstino" gets absorbed into the longitudinal component of the gravitino (the spin $\frac{3}{2}$ superpartner of the graviton)[26]. The gravitino mass then becomes:

$$m_{\tilde{G}} = \frac{F}{\sqrt{3}M_{Pl}}, \tag{5.17}$$

where F is the fundamental SUSY breaking scale in the hidden sector.

The NLSP can vary based on your choice of parameters, being most commonly the neutralino $\tilde{\chi}_1^0$, chargino $\tilde{\chi}_1^{\pm}$, or the stau. Additionally, as the neutralino is a mixture of gaugino states, as shown in Eq. 5.15, the decay modes of the neutralino can vary depending on the mixing. The different decay modes for different mixing scenarios is shown in Table 5.4.

Table 5.4: The final states for decays of the NLSP depending on different mixing scenarios.

NLSP	Decay Modes
Bino-like neutralino	Diphoton
Higgsino-like neutralino	Z/W(leptons or jets) H(b-jets)
Wino-like Neutralino/Chargino	Z/W(leptons or jets) Photons
Right-handed slepton	Multileptons Same sign dileptons
Sneutrino	Multileptons
Gluino/Squark	Jets

5.2.3.1 Diphoton final states

In this analysis we search for diphoton final states, so we choose a scenario with a Bino-like neutralino NLSP. A typical event for this scenario is shown in Figure 5.6 where at the LHC strong production dominates. From gluon-gluon fusion, gluinos are pair-produced, conserving R-parity, then decaying into quarks and the NLSP neutralino, with the neutralino decaying into a photon and an LSP gravitino.

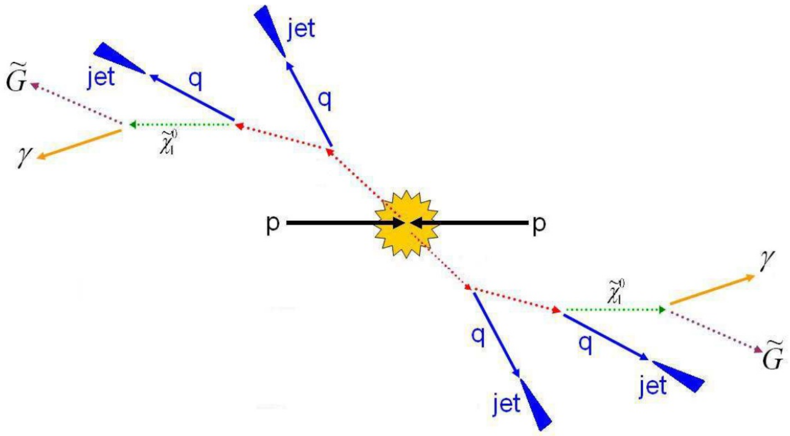

Figure 5.6: A typical GGM diphotonevent at the LHC.

5.3 Universal Extra Dimensions

Another proposed model of physics beyond the standard model is known as the Universal Extra Dimensions (UED) model[4, 2]. In UED models one or more additional TeV^{-1}-size compact extra dimensions exist. All the SM particles, fermions and bosons, then live in a 4+δ dimensional brane. This space can be further embedded in a larger space containing a of number of Large Extra Dimensions, where only gravity propagates, which allows for some additional decay modes. This is the case for the scenario studied in this thesis. The UED model, while it does not directly present a solution to the hierarchy problem, can provide some nice features, including proton-stability and anomaly cancelation. The phenomenology of the UED model has various similarities to SUSY models, including GGM, which make a combined search for SUSY and UED possible.

If we consider the case for one universal extra dimension, then for every SM fermion there are two five-dimensional fermion fields, $q^{\bullet}$ and q°. These two fields, being a doublet and singlet under $SU(2)$, combine to form Kaluza-Klein (KK) fields, which can undergo excitations creating new particle states with the unexcited state (zero-level) being the SM particles. However, fermions in more than four dimensions are not chiral. For five dimensions, the introduction of a S^1/Z_2 orbifold removes the extra degrees of freedom, restoring chirality[27]. The multiple levels of the particle excitations are known as KK towers, with excited states denoted with a star, such as q^*.

At the tree level, the masses of the KK excitations come from the 5-dimensional kinetic energy terms and from the Higgs interaction, which, as in the standard model, give mass to the zero-level particles. The masses of the n$^{\text{th}}$-level KK particles are then[2]:

$$m_n^2 = \frac{n^2}{R^2} + m_{SM}^2, \tag{5.18}$$

where R is the radius of compactification. As the value of R is at least several hundred GeV^{-1} the KK masses become degenerate for each level. Also, the extremely high masses of the 2nd level KK excitations put them beyond the reach of current colliders.

5.3.1 KK Parity

The KK level of each particle is an indication of the particle's momentum in the extra dimensions. This suggests that KK number should be conserved due to momentum conservation. However, the orbifold compactification breaks the translation symmetry in the extra dimension and leads to KK number violation. There is, analogous to supersymmetry's R-parity, a KK parity which conserves the "evenness" or "oddness' of the KK number. KK parity can be expressed as[27]:

$$P = (-1)^n \tag{5.19}$$

where n is the KK level. Following from the assumption of KK parity we can infer two consequences, as we do with supersymmetry's R-parity conservation. First, KK particles must be produced in pairs and second, the lightest KK particle (LKP) should be stable. In some UED models this leads to a Dark Matter candidate.

5.3.2 Large Extra Dimensions

A possible scenario to introduce KK parity violating decays is to embed the 5-dimensional UED space in a larger 4+N dimensional space in which only gravity propagates. In this way, gravitational interactions can mediate KK parity violating decays. The number of large extra dimensions, N, must be at least 2 to preserve Newton's laws at the solar system scale, so N=1 is excluded. At N=2, decays to light gravitons are favored, while at N≥3, decays to heavier gravitons are favored, as shown in Figure 5.7.

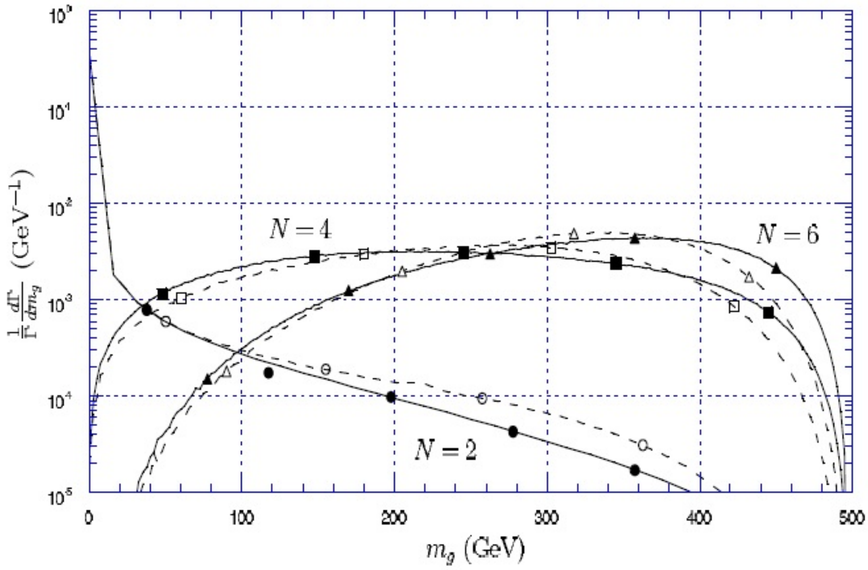

Figure 5.7: The graviton mass distribution for N=2,4,6 dimensions at 1/R=500 GeV. The dashed line represents g_1^* and the solid line represents q_1^*[2].

5.3.3 UED Phenomenology

If KK particles have nearly degenerate masses, then the gravitational decays to SM particles are dominated by KK quark and KK gluon decays (Fig. 5.8). This would be the case following from Equation 5.18; however, radiative corrections can lift this degeneracy[28]. Then the LKP becomes the KK photon γ^* with KK quarks and KK gluons cascading down to the KK photon. Decays to SM particles are dominated by the process $\gamma^* \to \gamma + G$. This produces the same diphoton plus E_T^{miss} final state as SUSY events and makes it possible to include UED models in this search without modifications to the analysis.

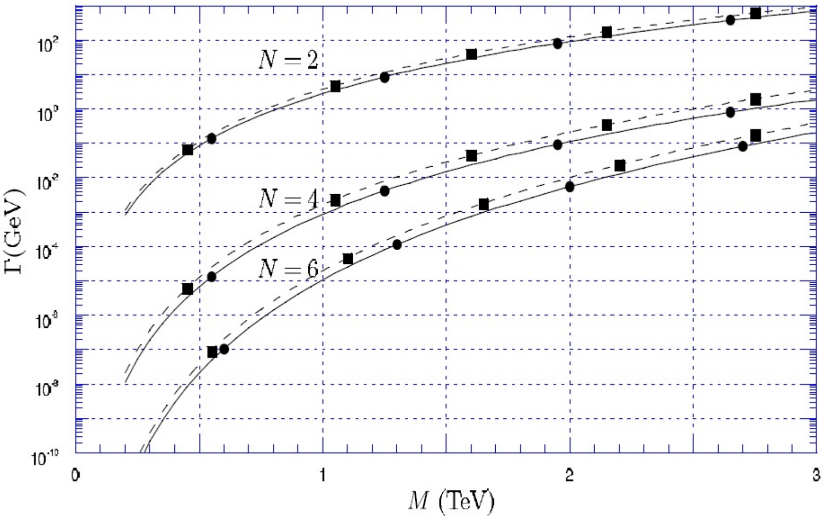

Figure 5.8: The decay widths for N=2,4,6 dimensions for M = 1/R. The dashed line represents g_1^* and the solid line represents q_1^*[2].

At the LHC, there are many different processes that can lead to the production of KK particles. These processes are shown in Figure 5.9. The decays from KK quarks and KK gluons are determined by the mass hierarchy and coupling constants as described in [2]. Gluon excitations decay through the processes $g_1^* \to q\overline{q}_1^\bullet$ and $g_1^* \to q\overline{q}_1^\circ$. The doublet quark excitations $q_1^\bullet$ decay primarily through the following chains:

$$q_1^\bullet \to qZ_1^* \to qll_1^\bullet \to qll\gamma^* \tag{5.20}$$

and

$$q_1^\bullet \to qW_1^* \to ql'l_1^\bullet \to ql'l\gamma^* \tag{5.21}$$

where l can be a lepton or a neutrino. The singlet quark excitations q_1° decay directly to the LKP by the process $q_1^\circ \to q\gamma^*$, since their coupling to the Z_1^* boson is suppressed.

The cross section for the overall process ending in the diphotonfinal state varies

Double KK gluon production		KK quark-gluon production	
$gg \rightarrow g_n^\star g_n^\star$	$q\bar{q} \rightarrow g_n^\star g_n^\star$	$qg \rightarrow q_n^\bullet g_n^\star$	$qg \rightarrow q_n^\circ g_n^\star$
	Double KK quark production		
$q\bar{q} \rightarrow q_n^\bullet \bar{q}_n^\bullet$	$q\bar{q} \rightarrow q_n^\circ \bar{q}_n^\circ$	$gg \rightarrow q_n^\bullet \bar{q}_n^\bullet$	$gg \rightarrow q_n^\circ \bar{q}_n^\circ$
$q\bar{q} \rightarrow q'^\bullet_n \bar{q}'^\bullet_n$	$q\bar{q} \rightarrow q'^\circ_n \bar{q}'^\circ_n$	$qq \rightarrow q_n^\bullet q_n^\bullet$	$qq \rightarrow q_n^\circ q_n^\circ$
$q\bar{q}' \rightarrow q_n^\bullet \bar{q}'^\bullet_n$	$q\bar{q}' \rightarrow q_n^\circ \bar{q}'^\circ_n$	$qq' \rightarrow q_n^\bullet q'^\bullet_n$	$qq' \rightarrow q_n^\circ q'^\circ_n$
$q\bar{q} \rightarrow q_n^\bullet \bar{q}_n^\circ$	$q\bar{q} \rightarrow q_n^\circ \bar{q}_n^\bullet$	$qq' \rightarrow q_n^\bullet q'^\circ_n$	$qq' \rightarrow q_n^\circ q'^\bullet_n$
$q\bar{q}' \rightarrow q_n^\bullet \bar{q}'^\circ_n$	$q\bar{q}' \rightarrow q_n^\circ \bar{q}'^\bullet_n$	$qq \rightarrow q_n^\bullet q_n^\circ$	

Figure 5.9: Production processes of KK excitation at hadron colliders.

with N, the number of large extra dimensions. For N=6, the model studied in this analysis, the cross section in the region of 1/R ~1 TeV is several times larger than for N=2, as shown in Figure 5.10.

5.4 Conclusion

In the search for answers to questions left by the SM, it has been shown that models exist, which can provide solutions in the form of new physics. Both the GGM SUSY and UED models are viable options to extend our understanding of elementary particles and their interactions. While many more models exist, which are not discussed here, the two models presented have signatures to which this analysis is sensitive and should be capable of detecting if they exist.

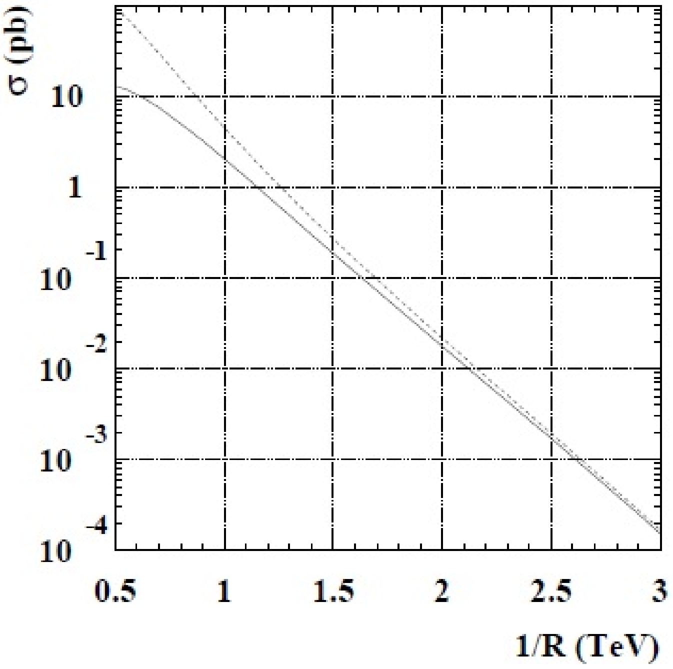

Figure 5.10: Cross sections for $\gamma\gamma + X + E_T^{miss}$ signal coming from universal extra dimensions at the LHC for N = 6 (solid line) and N = 2 (dashed line).

Chapter 6

Photon Identification

6.1 Introduction

The CMS detector has a similar response to photons, electrons, and EM jets. In order to differentiate the photons, several criteria were established that provide a unique identification and allow us to determine the photon identification efficiency. First of all, to simply the analysis, the search was restricted to the barrel region of the ECAL, where the seed crystal of the cluster is at least 6 crystals $\Delta\eta = 0.1$ away from the edges. This prevents any energy losses into the gap between the ECAL Barrel and Endcap. This region is defined in the η coordinate as $|\eta| < 1.379$. This eliminates possible misunderstood losses in efficiency at the cost of reducing the acceptance.

The photon-like objects are selected and classified by a series of identification cuts. For this analysis, we define photon-like objects as photons, electrons, and “fake” photons (EM jets). Selection begins with each significant deposit in the ECAL that is reconstructed into a supercluster [29]. The recommended photon identification cuts are then applied to each supercluster to reject non-isolated or non-photon objects and to classify the object. There are three levels of identification defined by the CMS Egamma group [30]. Their recommended cuts are listed in Table 6.1. An additional cut, the E2/E9 value described below, was also used.

Table 6.1: Photon identification cuts

Variable	Method	EM	Loose	Tight
Jurrasic ECAL Isolation	ECAL sum E_T cone ΔR 0.4	$< 4.2 + 0.006 * p_T$	$< 4.2 + 0.006 * p_T$	$< 4.2 + 0.006 * p_T$
Tower-based HCAL Isolation	Tower sum E_T cone ΔR 0.4	$< 2.2 + 0.025 * p_T$	$< 2.2 + 0.025 * p_T$	$< 2.2 + 0.025 * p_T$
Hadronic / EM	HCAL sum E_T/ ECAL sum E_T	< 0.05	< 0.05	< 0.05
Hollow cone track isolation	Track Sum p_T hollow cone ΔR 0.4		$< 3.5 + 0.001 * p_T$	$< 2.0 + 0.001 * p_T$
Eta width	$\sigma_{i\eta i\eta}$			< 0.013
Track veto	Has pixel seed		false	false

6.2 Photon Identification cuts

At hadron colliders, the number of particles in the underlying event make it nearly impossible to identify individual photons unless they are isolated. That is, they are far enough away from other particles to be sure that the EM object in question is not part of an EM jet. To determine isolation, three isolation quantities are computed.

6.2.1 ECAL isolation

To determine if the photon candidate is isolated from other EM activity an isolation algorithm, illustrated in Figure 6.1, is used. The total energy around the

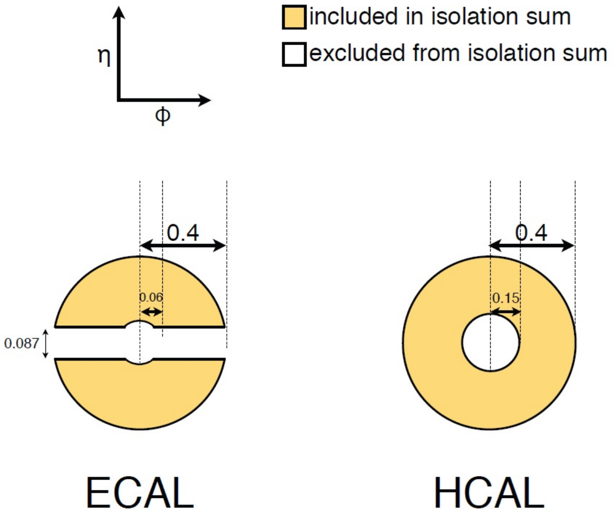

Figure 6.1: ECAL isolation methods.

center of the object in a cone formed by $\Delta R < 0.4$ is summed, and then the energy deposited in a strip of width $\Delta\eta$ from the center, oriented along the ϕ direction, is subtracted from the total energy. This is to ignore energy leakage along the edges of the crystals. A smaller cone of radius R_{in} is also removed to ignore contributions from the candidate object. This method is known as "Jurassic" isolation. The "Jurassic" isolation method significantly improves the rejection of QCD jets.

6.2.2 HCAL isolation

Since EM objects should deposit little or no energy in the HCAL, isolation in the HCAL is required. The total hadronic energy in a cone around the center of the deposit, where $\Delta R < 0.4$, is summed excluding the energy in a smaller inner cone at the center where $\Delta R < 0.15$. The inner cone is excluded to prevent overlap with the hadronic energy/EM energy ratio.

Charged hadrons can leave significant deposits in the ECAL before they reach the HCAL. In order to reject charged hadrons, the ratio of energy deposited in the HCAL to the energy deposited in the ECAL is computed. The size of the cones used to compute the energies is $\Delta R < 0.15$. A significantly smaller sized cone than the ones used for the ECAL and HCAL isolation is used in order to select only the energy in the vicinity of the supercluster itself. Unlike the ECAL isolation there is no strip removed from the isolation cone.

6.2.3 Track Isolation

Track isolation also uses the hollow cone “Jurrassic” method to determine isolation. However, the track isolation has a smaller strip removed than for the ECAL isolation.

6.2.4 Shower shape

The shower shape used in this analysis is defined in terms of a “modified second moment of the electromagnetic energy of the cluster about its mean η position [31]. A 5×5 matrix around the crystal with the highest energy is used to determine the covariance. The covariance $\sigma_{\eta\eta}$ is then

$$\sigma_{\eta\eta}^2 = \sum_{i=1}^{25} w_i(\eta_i - \eta)^2 / \sum_{i=1}^{25} w_i$$

where $w_i = max(0, ln(E_i/E))$, except that the η position is determined by the position of the crystal and not the absolute η in the detector. This allows for a more uniform distribution as the edges of the crystals are ignored. This variant of $\sigma_{\eta\eta}$ is then called $\sigma_{i\eta i\eta}$. Clusters from isolated prompt photons have a narrow distribution in $\sigma_{i\eta i\eta}$ whereas photons produced in hadronic decays produce larger values. This makes $\sigma_{i\eta i\eta}$ an excellent discriminator between photons and electromagnetic jets.

6.2.5 Pixel Seed Veto

Since photons and electrons have a very similar response using our identification criteria, an additional discriminator is needed. The presence of a charged track is one common method to veto electrons. However, since the CMS detector has a large amount of material, the silicon tracker and pixel detector, in between the impact point and the ECAL, a large number of photons will convert to electron-positron pairs via pair production. On average, about 40 percent of photons convert before they reach the ECAL. Therefore, a veto on the presence of a charged track will have an adverse effect on the acceptance. Instead, we use a Pixel Seed Veto based only on the presence of hits in the pixel detector. Since only about five percent of photons convert in the pixel volume the loss of acceptance is manageable. This assumption is verified in the following section.

6.2.6 Pixel Seed Veto Uncertainty

As we depend on the presence of the Pixel Seed to differentiate photons from electrons, it is important to understand the Pixel Seed efficiency and uncertainty. As photons pass through different regions of the pixel detector, they will encounter differing amounts of material, leading to some uncertainty in the efficiency. To determine the efficiency and uncertainty, MC simulations of photons were performed. MC photons with p_T ranging from 10 to 100 GeV were generated using a Particle Gun[1]. These photons were sent through an amount of material to simulate the pixel detector. Three scenarios[2] were used: a low material scenario ($X_0 min$), a high material scenario ($X_0 max$), and a nominal material scenario ($X_0 nom$). The results of the simulation are listed in Table

---

[1] The Particle Gun is an MC generator that creates photons with requested momenta, rather than being produced by any physical processes.

[2] Amounts of material are defined by the total radiation length (X_0).

6.2. The determined efficiency is then given as $0.9661 \pm 0.0004(stat) \pm 0.0014(syst)$.

Table 6.2: Fraction of Photon Gun generated photons with Pixel Seeds.

Scenario	Fraction of Photons with seeds
$X_0 min$	0.0339 ± 0.0004
$X_0 max$	0.0353 ± 0.0004
$X_0 nom$	0.0350 ± 0.0004

6.2.7 e2/e9 Veto

ECAL spikes, see Section 3.5.1, can create unbalanced high energy EM objects that simulate signal photons and create artificial E_T^{miss}. To reject these objects we compute each supercluster's e2/e9 value. The e2/e9 value is computed by examining a 3×3 matrix of crystals, with the seed crystal at the center. The e2 value is the sum of the energy deposited in the two highest energy crystals and the e9 value is the sum of all nine crystals in the matrix. Thus e2/e9 is the ratio of these two values. This is an effective discriminator for ECAL spikes because the spikes are typically contained in one or two crystals whereas for actual EM objects the energy is distributed over the entire cluster.

6.3 EM Object Classifications

The selected EM objects are divided into three orthogonal classifications: photons, electrons, and fake photons. For each event, only the two highest p_T objects are considered. These are defined as the “lead” and “trail” objects with $p_{T_{lead}} > p_{T_{trail}}$. The photon sample should be a very pure collection of true photons. The electron sample should also be almost totally comprised of true electrons, coming predominately from the $Z \to ee$process. The fake photon sample will consists of mostly highly electromagnetic jets. These samples are defined by the following cuts.

6.3.1 Photons

The photon used in this analysis is defined as any supercluster that passes all the isolation cuts (ECAL, HCAL, Track), the Hadronic/EM cut, the shower shape cut, has no Pixel seed, and passes the ECAL spike rejection e2/e9 cut.

6.3.2 Electrons

Electrons are defined in the same way as photons, except that they require a pixel seed. The electron sample is dominated by the process $Z \to ee$. The di-electron invariant mass is shown in Figure 6.3 where the Z peak is clearly visible.

6.3.3 Fake Photons

Fake photons are photons, with or without pixel seed, that fail either the track isolation or shower shape cuts. These objects are likely photons from π^0 decays or highly electromagnetic jets. The difference in shower shape between photons and fakes is clearly illustrated in Figure 6.2.

6.4 Analysis of Identification Cuts

The CMS Egamma group has published two sets of recommended identification (id) cuts: loose cuts and tight cuts. A study was performed to determine the effect on the efficiency of using the loose cut recommendation.

The loose cut criteria remove the $\sigma_{i\eta i\eta}$ requirement and increase the base threshold, before corrections for p_T, of the track isolation from 2.0 GeV to 3.5 GeV. The loss of the $\sigma_{i\eta i\eta}$ cut is the most problematic because the fake photon shapes are very different from electrons and photons, as shown in Fig. 6.2. As fake photons are differentiated from photons and electrons by the showershape and track isolation, we would expect the loosening of these cuts to add more background than signal.

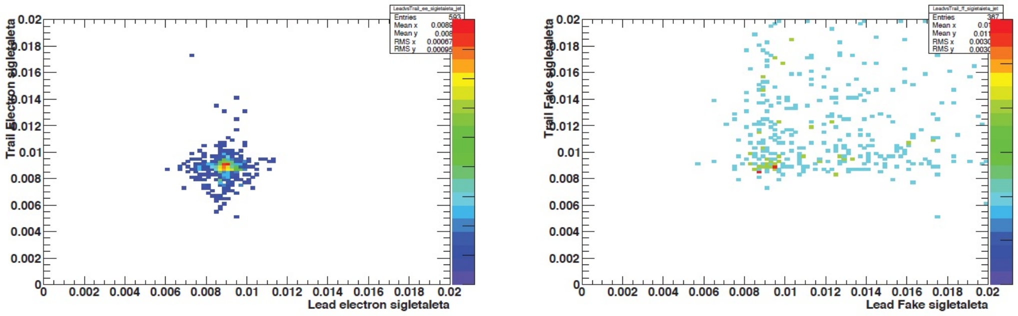

Figure 6.2: Left: The $\sigma_{i\eta i\eta}$ distribution for electrons. Right: The $\sigma_{i\eta i\eta}$ distribution for fake photons.

This effect can be examined quantitatively using three candidate samples from the data, $\gamma\gamma$, ee, and ff, which contain events with two photons, two electrons, or two fakes, respectively. If we assume that the ee sample is completely dominated by $Z \rightarrow ee$decays, the ff sample is completely QCD, and the efficiency of the $\sigma_{i\eta i\eta}$ cut is the same for electrons and photons, we can then define relationships based on the number of ee events passing whichever cut scenario we choose to examine.

$$N_{ee_{pass-pass}} = \varepsilon_1 \varepsilon_2 N_Z \tag{6.1}$$

$$N_{ee_{pass-loose}} = \varepsilon_1 (1 - \varepsilon_2) N_Z \tag{6.2}$$

$$N_{ee_{fail-pass}}\gamma = (1 - \varepsilon_1) \varepsilon_2 N_Z \tag{6.3}$$

$$N_{ee_{fail-fail}} = (1 - \varepsilon_1)(1 - \varepsilon_2) N_Z, \tag{6.4}$$

where ε_1 and ε_2 are the probabilities of the electron passing the selected cut scenario, for the lead and trail electron, respectively. Since we measure the quantities N_Z and

N_{ff} we can solve for the efficiencies ε_1 and ε_2.

We can also write relationships in terms of the fake-fake sample.

$$N_{ff_{pass-pass}} = f_1 f_2 N_{ff} \tag{6.5}$$

$$N_{ff_{pass-fail}} = f_1(1 - f_2)N_{ff} \tag{6.6}$$

$$N_{ff_{fail-pass}} = (1 - f_1)f_2 N_{ff} \tag{6.7}$$

$$N_{ff_{fail-fail}} = (1 - f_1)(1 - f_2)N_{ff}, \tag{6.8}$$

where f_1 and f_2 are the probabilities of a fake photon passing the selected cut scenario, for the lead and trail fake, respectively. As with the ε values, we can solve for f_1 and f_2. The computed values are $\varepsilon_1 = 1.00 \pm 0.00$, $\varepsilon_2 = 0.99 \pm 0.00$, $f_1 = 0.65 \pm 0.02$, and $f_2 = 0.69 \pm 0.02$.

We can then determine the number of **actual** two photon events in the $\gamma\gamma$ sample, which we define as $N_{photon-photon}$. Similarly, we can define the number of **actual** one photon and one fake events and **actual** two fake events as $N_{photon-fake}$ where the trail photon is a fake, $N_{fake-photon}$ where the lead photon is a fake, and $N_{fake-fake}$ where both photons are fakes.

$$N_{ee_{pass-pass}} = \varepsilon_1\varepsilon_2 N_{photon-photon} + \varepsilon_1 f_2 N_{photon-fake} + f_1\varepsilon_2 N_{fake-photon} + f_1 f_2 N_{fake-fake} \tag{6.9}$$

$$\begin{aligned} N_{ee_{pass-fail}} = {} & \varepsilon_1(1 - \varepsilon 2)N_{fake-fake} + \varepsilon_1(1 - f_2)N_{photon-fake} + f_1(1 - \varepsilon_2)N_{fake-photon} \\ & + f_1(1 - f_2)N_{fake-fake} \end{aligned} \tag{6.10}$$

$$\begin{aligned} N_{ee_{fail-pass}} = {} & (1 - \varepsilon_1)\varepsilon_2 N_{photon-photon} + (1 - \varepsilon_1)f_2 N_{photon-fake} + (1 - f_1)\varepsilon_2 N_{fake-photon} \\ & + (1 - f_1)f_2 N_{fake-fake} \end{aligned} \tag{6.11}$$

$$N_{ee_{pass-fail}} = (1-\varepsilon_1)(1-\varepsilon_2)N_{photon-photon} + (1-\varepsilon_1)(1-f_2)N_{photon-fake} \\ + (1-f_1)(1-\varepsilon_2)N_{fake-photon} + (1-f_1)(1-f_2)N_{fake-fake} \quad (6.12)$$

Then we have a system of four equations with four unknowns: $N_{photon-photon}$, $N_{photon-fake}$, $N_{fake-photon}$, and $N_{fake-fake}$. These equations can be solved for the Tight-Tight and Tight-Loose scenarios using the data in Table 6.3 to determine the composition of each sample.

Table 6.3: Number of events in each sample for different id criteria.

ID Type	$\gamma\gamma$	ee	ff
Both pass $\sigma_{i\eta i\eta}$	87	588	167
Only lead passes $\sigma_{i\eta i\eta}$	8	5	74
Only trail passes $\sigma_{i\eta i\eta}$	0	0	90
Both fail $\sigma_{i\eta i\eta}$	0	0	36

Table 6.4: The composition of the $\gamma\gamma$ sample for different id criteria.

Photon Cuts	Photon-Photon	Photon-Fake	Fake-Fake
Tight-Tight	80.8%	19.2%	0.0%
Tight-Loose	74.6%	25.4%	0.0%

As can be seen in Table 6.4, using the relaxed id cuts significantly decreases the purity of our photon sample.

6.5 Photon Efficiency

To determine the photon identification efficiency, two methods were used. The process $Z \to ee$ produces a clearly identifiable peak at the Z mass of 91.1 GeV. As a certain number of electrons will be misidentified as photons, the Z mass peak will be visible in both the $e\gamma$ and ee invariant mass spectra. By determining the count of events in the Z mass peak seen in the $e\gamma$ invariant mass, one can determine the number of misidentified electrons in the photon sample. By comparing the number of misidentified electrons with the number of electrons in the Z peak of the ee invariant mass, one can compute a photon fake rate. The second method uses a tag-and-probe analysis to determine the efficiency. A "tag" electron is chosen, assumed to be from the Z decay, then a "probe" electron is chosen, assumed to be the other leg of the Z decay. From the number of events passing/failing the tag and probe, an efficiency can be determined.

6.5.1 Electron-Photon Misidentification Rate

To determine the number of $Z \to ee$ events in the three candidate samples, we perform a fit of the invariant mass for each sample. In the ee sample, a Crystal Ball function[3] with a linear background (Fig. 6.3) was used. For the $e\gamma$ sample a Crystal Ball function with a linear background was also used (Fig. 6.4). For the $\gamma\gamma$ sample a Breit-Wigner[4] convoluted with a gaussian plus a linear background was used(Fig. 6.5).

Statistical errors, determined by the total number of $Z \to ee$ events, are calculated from the integrals of the fits. Systematic errors were determined by also fitting each sample using a constant background. The differences in the integrals for linear and constant background are the systematic errors.

---

[3] The Crystal Ball function, used to describe regions with low mass tails due to radiative losses (bremsstrahlung) is defined as:

$$f(x) = \begin{cases} Ae^{-\frac{1}{2}(\frac{x-x_0}{\sigma})^2} & \frac{x-x_0}{\sigma} > \alpha \\ A(\frac{n}{\alpha})^n \cdot e - \frac{-\alpha^2}{2} \cdot (\frac{n}{\alpha} - \alpha - \frac{x-x_0}{\sigma})^{-n} & \frac{x-x_0}{\sigma} < \alpha \end{cases} \tag{6.13}$$

where A,x_0, and σ are the amplitude, mean, and standard deviation, respectively.

[4] The Breit-Wigner distribution is defined as:

$$f(x) = \frac{\Gamma}{(x - x_0)^2 + \frac{\Gamma^2}{4}} \tag{6.14}$$

where x_0 is the mean and Γ is the standard deviation

In order to determine the electron identification efficiency, we sum the contents of the Z peak in the ee,$e\gamma$, and $\gamma\gamma$ spectra and define this quantity as the number of $Z \rightarrow ee$ events N_Z. The expected number of ee events observed should then be calculated as

$$N_{ee} = f_e^2 N_Z \tag{6.15}$$

and the number of $Z \rightarrow ee$ events in the $e\gamma$ sample will be

$$N_{e\gamma} = 2[f_e(1 - f_e)]N_Z \tag{6.16}$$

Using 6.15 and 6.16 we can calculate the electron misidentification fake rate.

$$f_e = [1 + 0.5\frac{N_{e\gamma}}{N_{ee}}] - 1 \tag{6.17}$$

We can calculate, as a check, the number of $Z \rightarrow ee$ expected in the $\gamma\gamma$ spectrum using

$$N_{\gamma\gamma} = \frac{[(1 - fe)(1 - fe)]}{[(f_e^2)]} N_{ee} \tag{6.18}$$

Fitting the Z peak of the ee sample yields 1651.6±67.1 events with a systematic error of 46.5 events. Fitting the Z peak of the $e\gamma$ sample yields 50.9 ± 11.2 events with a systematic error of 0.9 event. From the fits we determine an efficiency of $98.46 \pm 0.34\%$. From this we identify the fraction of ee and $e\gamma$ events misidentified as $\gamma\gamma$ events as $(2.45 \pm 0.75) \times 10^{-4}$ and 0.016 ± 0.003, respectively. The misidentification rate will be used to determine the electroweak contribution to the $\gamma\gamma$ sample.

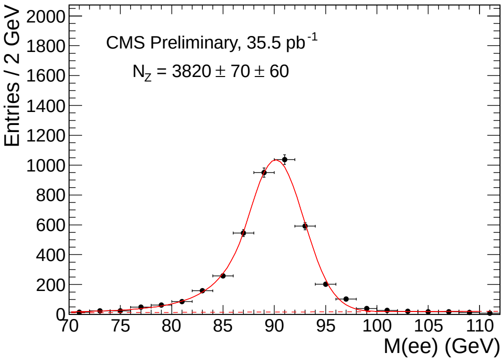

Figure 6.3: Di-electron invariant mass distribution. The $Z \rightarrow ee$ peak is clearly visible.

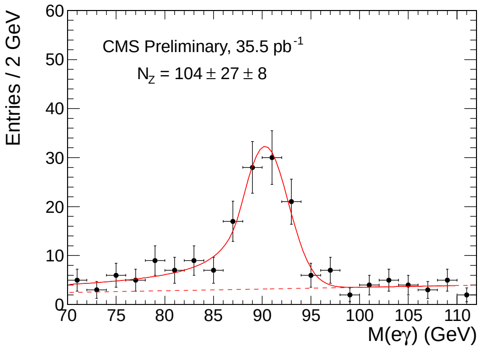

Figure 6.4: $e\gamma$ invariant mass. The $Z \rightarrow ee$ peak represents the misidentification of one electron as a photon.

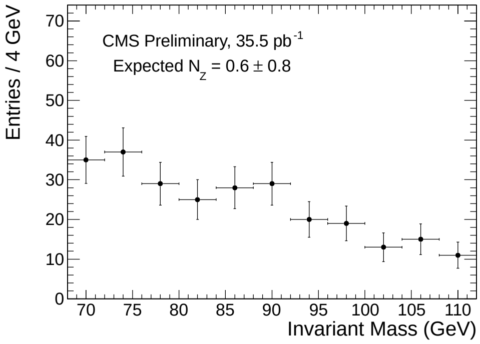

Figure 6.5: $\gamma\gamma$ invariant mass. The $Z \rightarrow ee$ peak represents the misidentification of both electrons as photons.

6.5.2 Photon Efficiency

Since there is no easily identifiable source of isolated photons in the data, we used the fact that electrons and photons have similar responses in the detector. This is also true with our choice of identification cuts. Since the ECAL and Track isolation both use hollow cones, the presence of the track in the case of the electron does not distinguish it from a photon. The other isolation cuts: H/E, shower shape, and HCAL isolation also were chosen to have similar distributions for photons and electrons.

6.5.2.1 Tag and Probe

The $Z \to ee$ gives us a clean source of electrons. By using a Tag and Probe method we can determine the electron identification efficiency which, to within some degree of error, will be the same as the photon identification efficiency. The Tag and Probe criteria are as follows:

For the tag:

- $E_T > 30$ GeV
- matched to a track with $p_T > 15$ GeV within $\Delta R < 0.04$, computed at its closest approach
- in the barrel region $|\eta| < 1.4$
- $\sigma_{i\eta i\eta} < 0.009$
- has a pixel seed
- $H/E < 0.05$
- separated from the nearest jet by $\Delta R > 0.9$

For the probe:

- $p_T > 30$ GeV

- in the barrel region $|\eta| < 1.4$

- matched to a track with $p_T > 30$ GeV within $\Delta R < 0.1$
- $H/E < 0.5$

To determine the electron efficiency, the invariant mass of tag-probe pairs for passing events m_{pass} and for failing events m_{fail} are computed. The passing pairs are those events in which both tag and probe pass the identification cuts detailed in table 6.1 and have a pixel seed. A simultaneous fit is then made on the m_{pass} and m_{fail} distributions to determine the electron efficiency ϵ_e^{data}. For both *pass* and *fail*, the signal shape assumed is a Breit-Wigner convoluted with a gaussian plus an exponential background. To make the fit an extended likelihood method is used.

6.5.2.2 Photon Scale Factor

While we are assuming the detector's response to photons and electrons is similar, there are measurable differences. To determine the effect of the differing response, we compute a "photon scale factor" by which the efficiency is scaled. The photon scale factor was determined by comparing the efficiency for electrons from data ε_e^{Data} and MC simulated $Z \rightarrow ee$ events ε_e^{MC} The photon scale factor, defined as $\varepsilon_e^{Data}/\varepsilon_e^{MC}$ is then shown in Fig. 6.6. Since there is no dependence on η, p_T, $\Delta R_{\gamma-jets}$, or N_{jets}, the bins from all four plots can be combined to determine the scale factor more accurately. The photon scale factor was determined to be 0.986 ± 0.008(stat) ± 0.041(sys).

6.5.2.3 Effect of Pileup

As the instantaneous luminosity increases the chance of having more than one hard scattering proton-proton interaction in each event goes up. This effect, known as "pileup," can reduce the photon efficiency. To determine this effect, the tag and probe

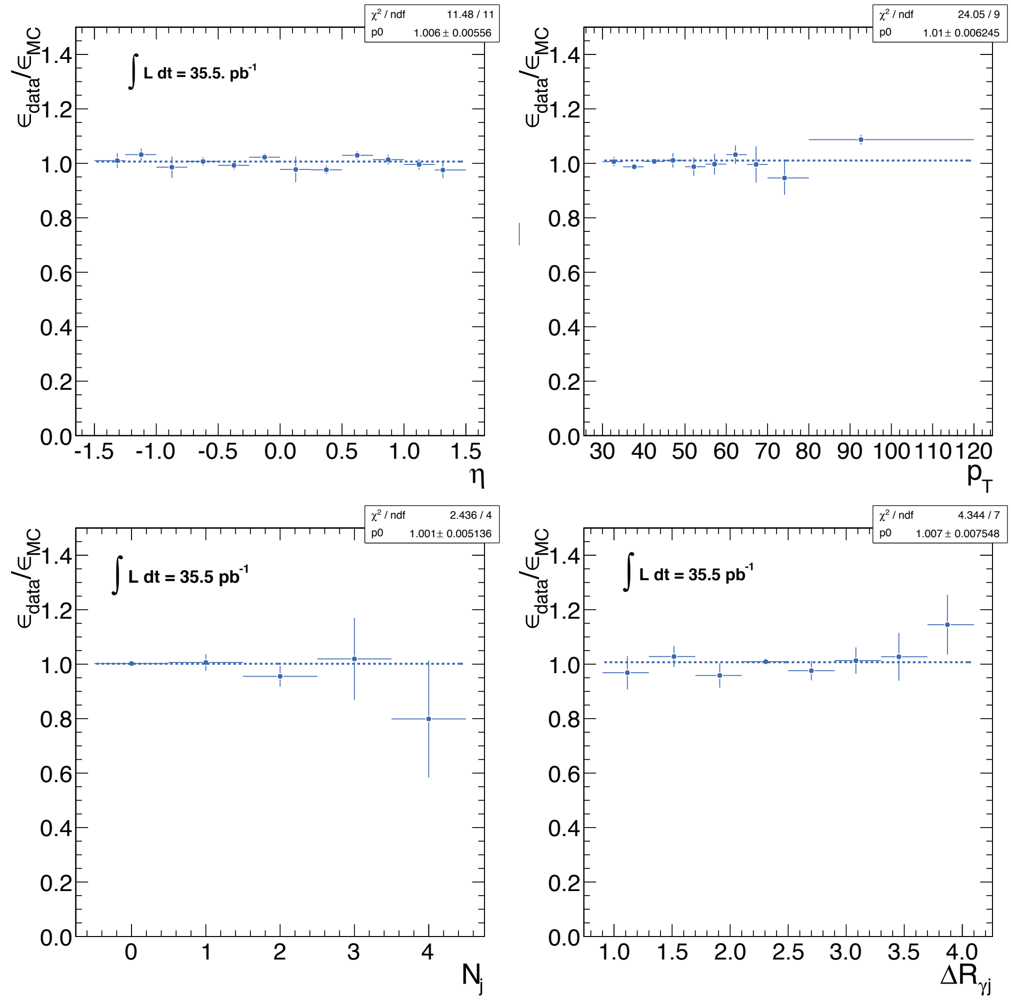

Figure 6.6: Upper Left: Eta. Upper Right: p_T. Lower Left: Number of Jets. Lower Right: ΔR jet-photon

method with $Z \to ee$ event was used again to calculate the electron efficiency ϵ_e^{data} as a function of the number of reconstructed primary vertices. The data fit well to a constant value of 0.88 ± 0.01 (Fig. 6.7), which agrees with the efficiency of 0.89 ± 0.02 obtained from a sample of tag-probe pairs in events with exactly one primary vertex. To determine the effect on the photon scale factor $\varepsilon_e^{Data}/\varepsilon_e^{MC}$, the photon scale factor was computed separately for events with exactly one primary vertex and then for all events. We determined a scale factor for events with one vertex of 0.99 ± 0.02 and 0.98 ± 0.01 for all data. The difference of 0.01 is used as the uncertainty on the photon scale factor due to pileup.

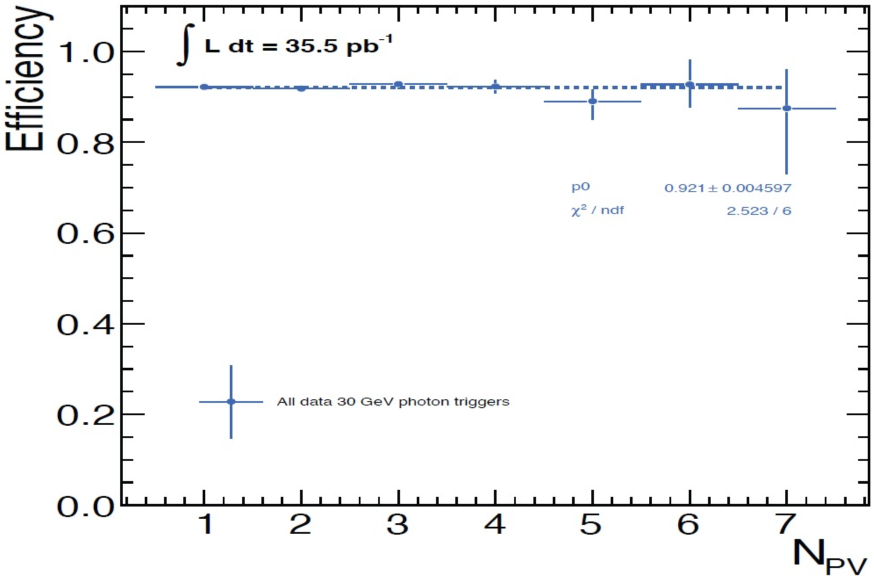

Figure 6.7: Using the tag and probe method with $Z \to ee$ events we determine the electron efficiency as a function of the number of reconstructed primary vertices. All 2010 data were used with the standard triggers listed in Table 7.2

Chapter 7

Data and Event Selection

All the data used in this analysis were collected using 7 TeV proton-proton collisions during the 2010 run. Monte Carlo generated signal and background events were generated with PYTHIA 6.4 and Madgraph. GGM spectra, containing particle mass and decay rates, were generated using ISAJET. For more information on the generation process see Appendix A.1.1.

To determine our candidate events we select events passing the following criteria:

- Two “tight” isolated photon candidates in the ECAL Barrel
    - $E_T > 30$ GeV
    - $|\eta| < 1.4$
    - With the separation between photons such that $\Delta R > 0.8$
- At least one hadronic jet
    - $p_T > 30$ GeV
    - $|\eta| < 2.6$

-Separated from each candidate photon by $\Delta R > 0.9$.

These objects are then divided into the diphoton signal candidate sample, $\gamma\gamma$, and the two control samples: ee and ff, which contain electrons and fake photons, respectively. The signal region is then defined as events with E_T^{miss} ¿ 50 GeV.

7.1 Datasets

The 36 pb^{-1} of data used, the entire amount collected during the 2010 run, were contained in two datasets, listed in Table 7.1. The triggers used to select candidate events are listed in Table 7.2. As luminosity increased during 2010, high rate triggers had to be prescaled and newer lower rate triggers were implemented. To be compatible with older data while avoiding prescaled triggers, multiple triggers were used with each event being required to pass at least one of the selected triggers. The triggered events were then skimmed to select events containing two ECAL superclusters with $E_T > 30$ GeV.

Table 7.1: Datasets used in the analyzed 36 pb^{-1}.

Dataset	Triggered Events	Skimmed Events
Photon-Run2010B-PromptReco-v2-RECO	16592333	2750303
EG-Run2010A-Sep17Reco-v2-RECO	52257480	1100267

7.1.1 Physics Validation

All collected data underwent validation by the CMS Physics Validation group before it was approved for use in physics analyses. The approved data list was provided in the form of a JavaScript Object Notation (JSON) file. The JSON file contains the Run number and LumiSection range for each validated run. The JSON file used for this analysis dated November 11, contained validated runs between runs 132440 and 149442.

7.1.2 Triggers

All of the triggers used require a leading photon with $E_T \geq 30$ GeV except HLT-Photon22-SC22HE-L1R-V1, which requires a single photon with $E_T \geq 22$ GeV that matches an ECAL supercluster. All triggers are cleaned of anomalous signals due to ECAL spikes using the methods described in Section 3.5.1. Some of the later triggers in Table 7.2 also have a photon isolation requirement that the photon have no track within a given radius $\Delta R \leq 0.4$ (where $\Delta R = \sqrt{(\phi_{track} - \phi_{photon})^2 + (\eta_{track} - \eta_{photon}^2)}$ of the photon. Even though the photon identification cuts stated in Section 6.2 require $E_T \geq 30$ GeV for both photons, the effect of the threshold turn on of the trigger efficiency on the signal efficiency is minimal. This is because all the triggers used are single photon triggers while the event selection, described below, requires two photons of $E_T \geq 30$ GeV, giving selected events two opportunities to pass the trigger.

Table 7.2: Triggers used to select candidate events. Different triggers were used to avoid prescaling.

Triggers
HLT-Photon30-L1R
HLT-Photon30-Cleaned-L1R
HLT-Photon30-L1R-8E29
HLT-Photon30-Isol-EBOnly-Cleaned-L1R-V1
HLT-Photon22-SC22HE-L1R-V1

7.2 Physics Objects

CMSSW reconstructs hundreds of physics objects in each event. The objects that are used in this analysis, which is a small subset of the total objects, are described here.

7.2.1 Photons

The CMSSW photon is defined as a reconstructed supercluster. Therefore, the base photon collection contains all reconstructed EM objects, not differentiating between photons, electrons, and jets. In order to separate the different objects and remove "double counting", where an object is reconstructed as more than one object i.e. photons commonly appear in the jet collections as well, additional cuts are needed.

7.2.2 Missing Transverse Energy

Missing transverse energy E_T^{miss} is defined as the imbalance of momentum transverse to the beam line for all final state particles. At hadron colliders, since the colliding particles are composite objects, the total energy of the collision is unknown. However, the total energy transverse to the beam line can be assume to be zero. By conservation of momentum, the sum of transverse momentum after a collision should also be zero. Any imbalance of transverse momentum implies that some particles escaped undetected. As possible exotic particles suggested by theories beyond the standard model will escape undetected, E_T^{miss} becomes a key variable in the search for new physics.

There are three methods for calculating the E_T^{miss} for each event. The simplest method, known as CaloMET, is calculated only using the ECAL and HCAL. An improvement to CaloMET is "track corrected" MET (tcMET). tcMET starts with CaloMET and makes corrections to the energy based on reconstructed track momenta. This is useful as the tracker provide more accurate energy measurements. The third type of E_T^{miss} is Particle Flow MET (pfMET). The particle flow algorithm tries to reconstruct every particle in the event and sum the momenta to determine the E_T^{miss}. The particle flow system creates collections of particle flow objects, i.e. pfPhotons, pfElectrons, etc.

To use pfMET it is recommended that one use all “pf” objects for consistency.

7.2.2.1 Jets

There are four types of jets reconstructed by the CMSSW software. The jets used in this analysis are reconstructed using the Jet Plus Track (JPT) algorithm with L1, L2, and L3 corrections to E and E_T. The JPT algorithm [32] starts with calorimeter jets (calojets), but since the poor energy resolution of the HCAL affects jet energy, the CMS tracking detectors are used to correct the jet p_T.

Calojets use energy deposits from both the ECAL and HCAL, combined into “towers.” A calorimeter tower is built from HCAL and ECAL cells that are aligned geometrically. There are several different clustering algorithms that can be applied to reconstruct the calojets. In this analysis, all jets are reconstructed using the anti-K_T algorithm [33] with a cone radius of $\Delta R = 0.5$.

Charged particle tracks are associated to each calojet by distance in η and ϕ at the surface of the calorimeter. The jet energy and direction is then corrected by the more accurately measured associated tracks.

The energy corrections to reconstructed jets are applied sequentially, in stages that are called levels. The first three levels of energy correction are the Offset, Relative (η), and Absolute (p_T) corrections [34]. The (L1) Offset correction accounts for pileup and electronic noise. The (L2) Relative corrections are necessary because the CMS jet response has an η dependence for a fixed jet p_T. The L2 correction makes the CMS response flat in η. The (L3) Absolute correction corrects the jet p_T versus total energy. This correction comes from a data-driven analysis using photon + jet and Z + jet p_T balance in collision data.

7.3 Event Selection

Candidate events were divided into four distinct sample sets used in the analysis: $\gamma\gamma$, $e\gamma$, ee, and ff events. While events could contain more than two EM objects, possibly allowing an event to qualify for more than one set, only the two highest E_T EM objects are considered to ensure no overlap. Additionally, the two objects must be separated by $\Delta R > 0.8$. If the two highest E_T EM objects do not pass the separation cut, then the event is rejected.

7.3.1 Analysis Cuts

The analysis cuts used to selected isolated objects cause some loss in efficiency. The final event counts for the $\gamma\gamma$, ee, $e\gamma$, and ff samples are shown in Table 7.3.

Table 7.3: Final counts of events passing all selection criteria with 36 pb^{-1}.

Sample	Events (No Jet Req.)	Events ($\geq$ 1 Jet)
$\gamma\gamma$	404	87
$e\gamma$	234	43
ee	4348	588
ff	1950	425

7.3.2 Jet Selection

Of the jets identified by CMSSW, we only use the jets that pass “loose” selection cuts. A loose jet is defined by the following criteria:

- Jet $p_T > 30$ GeV
- $|\eta| < 2.6$ (no forward hadron calorimeter (HF) jets)
- $fHPD \leq 0.98$ (fHPD is the fraction of energy contributed by the highest energy hybrid photodetector readout

- $N90 \geq 2$ (N90 is the minimum number of ECAL and HCAL cells required to contain 90% of the jet energy)

- $EMF \geq 0.01$ (EMF is the electromagnetic fraction of the jet)

To maintain isolation, jets are also required to be separated from both EM objects by at least $\Delta R > 0.9$. This value was chosen as it is the sum of the size of the isolation cones for EM objects, 0.4, (Section 6.2) and the size of the jet reconstruction cone, 0.5 (Section 7.2.2.1).

Contrary to the separation cut for EM objects, if the separation in ΔR between a jet is within 0.9 of either EM object then the jet is rejected rather than the entire event. This is necessary as the jet reconstruction algorithm also identifies the EM objects as jets. The separation cut therefore serves to remove the "double-counted" jets. It is assumed that, in most cases, a real jet near an EM object will cause the object to fail the ECAL and/or HCAL isolation cuts.

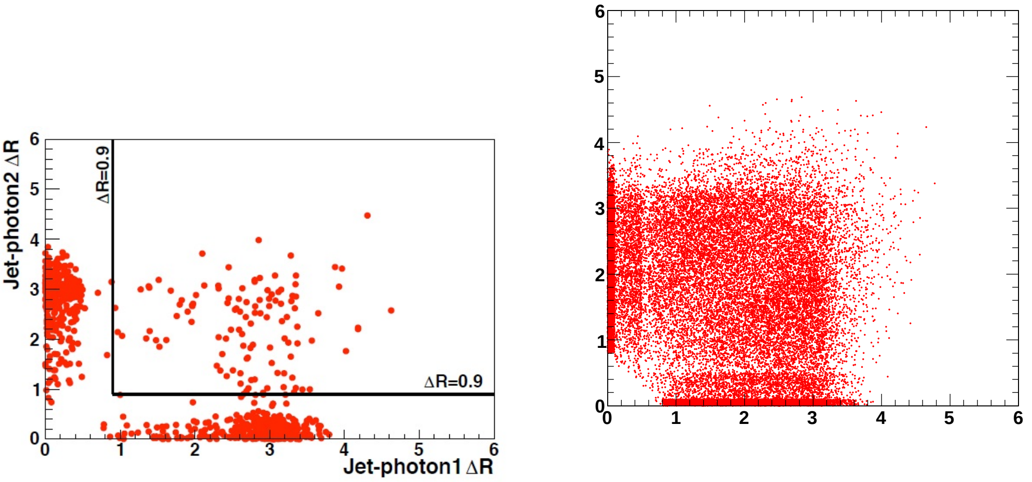

Figure 7.1: Distance from jets to each photon in the $\gamma\gamma$ sample. Right: From data. Left: From UED MC R=1/900.

7.3.3 Jet Requirement

Background events from out-of-time sources, such as cosmic ray and beam halo muons, can very effectively mimic the diphoton and E_T^{miss} signal. Cosmics mimic the signal because the reconstruction algorithm for tracks used during collisions[1] is not designed to reconstruct tracks not originating near the impact point. As cosmic muons can pass through the detector at any angle, without reconstructed tracks, cosmic events can appear as events with two EM clusters (one as it enters the detector and one as it exits), which are interpreted as photons, and large E_T^{miss} because the clusters are not balanced. Such an event is shown in Figure 7.2. Beam halo muons can have a similar effect as beam halo muons can scatter from anywhere along the beam line.

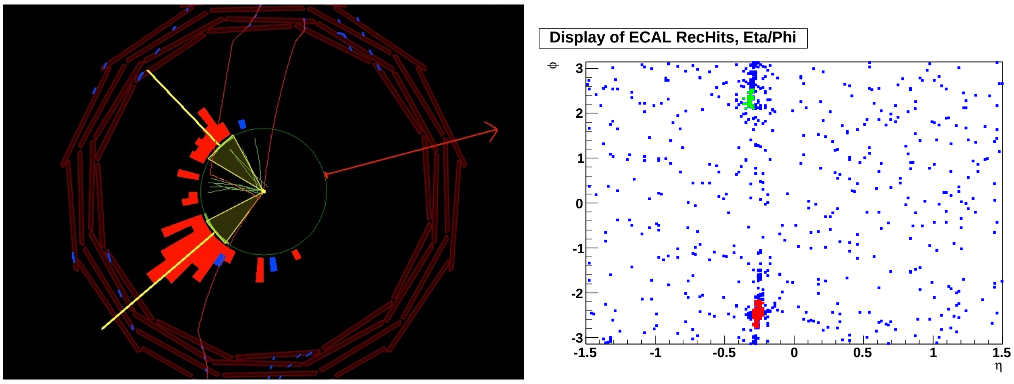

Figure 7.2: Run:143323 Event:313558208. Left: The Rho-Phi view of the CMS detector showing a cosmic event mimicking a diphoton and E_T^{miss} signal. Right: The Eta-Phi view of the ECAL hits. The red cluster represents the higher energy entry point of the muon while the blue cluster shows the lower energy exit point.

In order to eliminate the contribution from out-of-time sources, we require at least one jet to be present in the event. As jets are produced only by hard scattering events and are not present in cosmic and beam halo events, the jet requirement makes the out-of-time background contribution negligible.

---

[1] During cosmic runs a different algorithm is used that assumes the muon is originating outside the detector.

7.3.3.1 Jet Energy Scale

Due to the energy resolution and calibration of the CMS calorimeters, there is some uncertainty associated with the measured p_T of jets. This uncertainty was determined to be 10% [32]. As our selection criteria include a jet requirement with $p_T > 30$ GeV, this uncertainty will have some effect on our acceptance. To quantify this effect a study was performed.

To estimate the effect on acceptance of a varying jet p_T, the acceptance was calculated for three different GGM MC points with jet p_T cuts 10% above and below 30 GeV. The difference in acceptance is shown in Table 7.4. Since, as shown by these results, the effect on the acceptance due to Jet Energy Scale uncertainty is minimal, a very conservative 2% error is used.

Table 7.4: Acceptances for different jet $p_T$thresholds in MC generated GGM events.

GGM Point	Acc. ($p_T > 27$) GeV	Acc. ($p_T > 30$) GeV	Acc.($p_T > 33$) GeV
1	0.245 ± 0.004	0.249 ± 0.004	0.249 ± 0.004
2	0.185 ± 0.004	0.158 ± 0.004	0.190 ± 0.004
3	0.141 ± 0.004	0.140 ± 0.004	0.140 ± 0.004

7.3.4 Analysis of 36 pb^{-1} Data

With all the analysis cuts applied and considering only the signal region ($E_T^{miss} > 50$ GeV) we observe one event. This event is shown graphically using the CMS "Fireworks" Event display, in Figure 7.3. The 3D display (upper left) shows the CMS detector at the outer surface of the calorimeters. The red columns represent deposits in the ECAL, the blue columns are deposits in the HCAL and the red arrow represents the E_T^{miss}. The 3D Lego plot (upper right) shows the calorimeter deposits. The $x - y$ view (lower left) shows the CMS detector from along the beamline. The two photons, shown as ECAL deposits, are clearly visible, as is the one jet. The $\rho - z$ view (lower right) clearly illustrates the energy imbalance of the event.

Table 7.5: Kinematic values for observed event.

Object	p_T (GeV)	η (rad.)	ϕ (rad.)
Lead Photon	88.7	-0.116	1.75
Trail Photon	54.9	0.0158	0.190
Jet	33.3	1.60	-1.86
E_T^{miss}	57.2	-	2.12

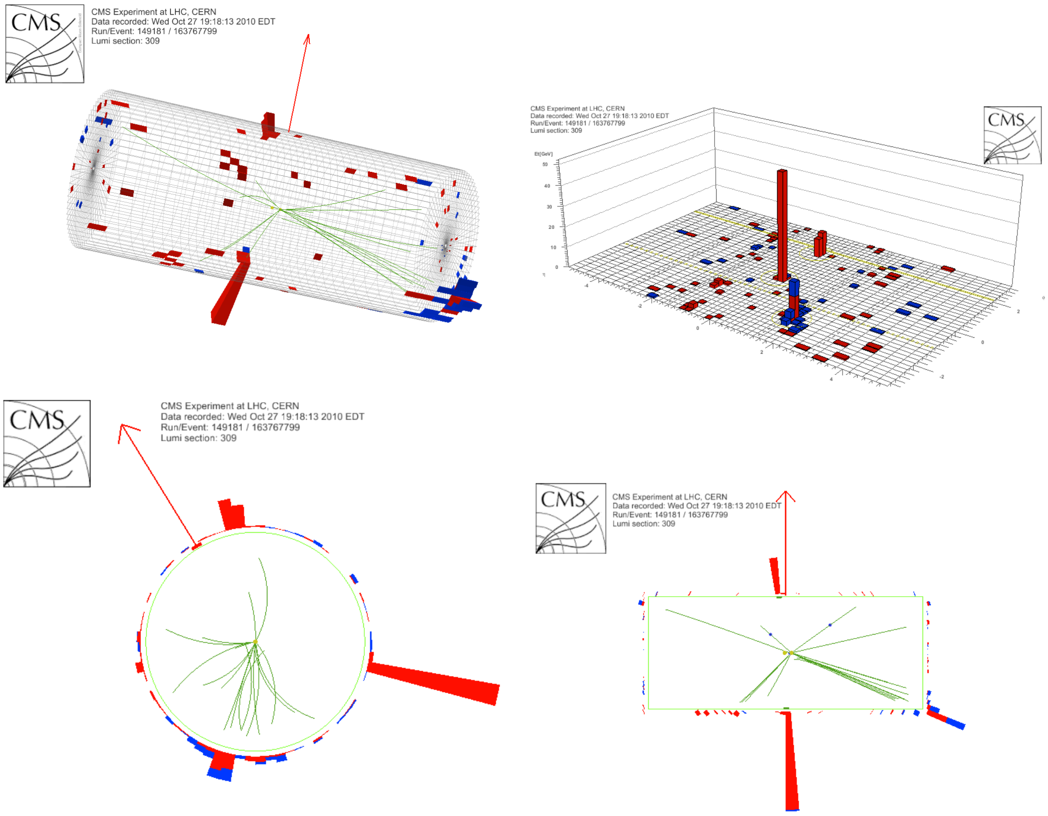

Figure 7.3: One event passing all selection cuts was observed in 36 pb^{-1} of 2010 data.

7.4 Monte Carlo Signal

The search performed in this analysis was designed to be a general search. The only standard model processes that produce the diphoton and large E_T^{miss} signal, $W\gamma\gamma$ and $Z\gamma\gamma$, have cross sections so small that they are negligible. Therefore, any detected signal is an indication of new physics. In order to illustrate our sensitivity to physics beyond the standard model, we chose two BSM models, Gauge Mediated SUSY and Universal Extra Dimensions, for which we generated MC signal events.

7.4.1 General Gauge Mediation

The MC events for GGM were generated for a range of squark and gluino masses between 400 and 2000 GeV with three choices of neutralino mass, 50, 150, and 500 GeV. These points were generated as part of the "Summer 2010" MC Production and all the point were combined into a single dataset. The parameter values ($M_{\tilde{g}}$, $M_{\tilde{q}}$, $M_{\tilde{\chi}_1^0}$) and cross section were added to each event for identification during analysis.

Other GGM parameters were fixed to the LHC "Benchmark" scenario for a "Bino-like" neutralino NLSP [35]. The ISAJET program used these parameters to generate particle masses, decay modes, and branching ratios. These values are then stored in a format known as the SuperSymmetry Les Houches Accord (SLHA). The SLHA file is then passed to PYTHIA 6.4 to perform event generation and hadronization.

7.4.2 Universal Extra Dimensions

The UED model has two varying parameters, Λ, the ultraviolet cutoff, and R, which is the radius of compactification. In this and the previous studies R is the free parameter while Λ is chosen to satisfy the relation $\Lambda R = 20$.

Additional parameters are used by PYTHIA 6.4 [36], which is used to generate the signal Monte Carlo (MC). These values were chosen to match the previous ATLAS analysis [37] and are as follows:

- Number of Large Extra Dimensions: 6
- M_D, the $(N + 1)$ dimensional Planck scale: 5 TeV
- Number of KK excitation quark flavors: 5

Sample points of $1/R$ equal to $700, 750, 800, 850, 900, 950$, and 1000 GeV are generated and analyzed using the same technique as in the gauge mediated SUSY search performed by CMS. All points were generated using CMSSW_3_8_5 with FASTSIM. The list of produced datasets is shown in Table 7.6. Since the UED MC samples were produced privately, some indirect validation was performed. The PYTHIA parameters and MC tune were chosen to be the same as for the GGM production MC. As a check of the procedure, the same configuration was used to generate several GGM points, which were analyzed and compared to the GGM production.

The generation of UED events with PYTHIA is straightforward, with only one parameter (R) to be set. UED production cross sections agree with the published cross sections from the ATLAS analysis [37]. Any other differences that could affect the analysis would have to be due different PYTHIA settings for hadronization or the underlying event. The cross sections and acceptance times efficiency of privately produced GGM points and production GGM points are within one percent, which would have a negligible effect on the overall result of the analysis. Table 7.7 shows a comparison of the production and private GGM points.

Table 7.6: UED signal datasets.

1/R	**Dataset**
700	/UED_700/stringer-UED_700-7e4a337ac7d53c52317548c28cf66ab4/USER
750	/UED_750/stringer-UED_750-e845e099efd769f087e759fde47c8362/USER
800	/UED_800/stringer-UED_800-90c8befa1fa4a39a2881aa446562a647/USER
850	/UED_850/stringer-UEDn_850-c0ad3da711a1c3defbf0da24825897fc/USER
900	/UED_900/stringer-UED_900-9526f4ab86428cba1d4e4a9eafca7915/USER
950	/UED_950/stringer-UED_950-c12b9ea43225b378541cf11da6296a78/USER
1000	/UED_1000/stringer-UED_1000-8acfc87e8fc7ea3c336ba286e799a6f8/USER

Table 7.7: Comparison of GGM samples.

$M_{\tilde{g}}$ GeV	$M_{\tilde{q}}$ GeV	$M_{\tilde{\chi}_1^0}$ GeV	Eff × Acc (Prod)	Eff × Acc (Priv)
1040	640	50	16.92%	17.23%
1360	720	500	19.51%	20.18%
1680	720	150	24.98%	24.91%

7.4.3 Monte Carlo Studies

Several studies using GGM and UED MC were performed. The effect of the restriction to the ECAL barrel on acceptance was examined with respect to the GGM and UED generated MC signal events. The effects of losses in efficiency were studied for the selection cuts in general and in detail for the jet requirement. Also, to determine the limits as is discussed in Chapter 9, the total acceptance times efficiency must be determined for both models.

7.4.3.1 Effects on Acceptance due to Barrel Restriction

The loss in acceptance due to limiting the analysis to the ECAL barrel ($|\eta| < 1.379$) can be shown to be very small. This is because of the tendency of GGM and UED events to have the photons and jets very centralized with respect to the detector. A comparison of the η distribution for photons and jets is shown in Figure 7.4.

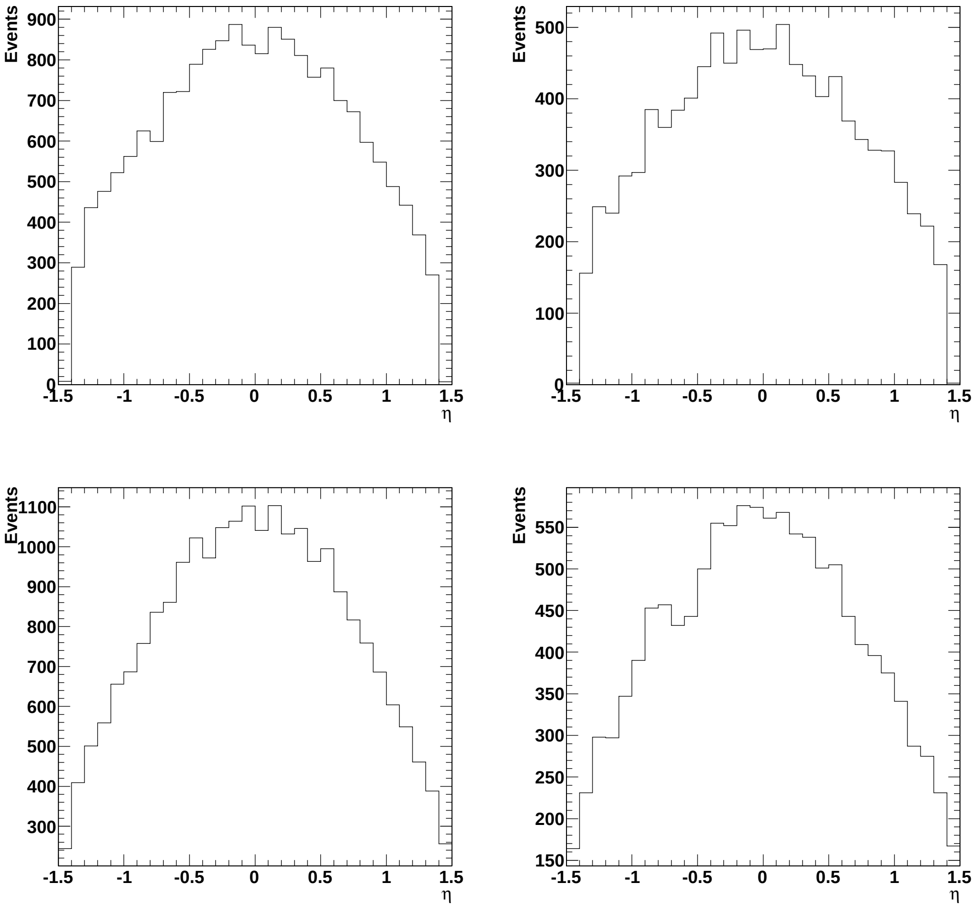

Figure 7.4: Upper Left: η distribution for UED MC signal photons (1/R=800). Upper Right: η distribution for GGM MC signal photons ($M_{\tilde{g}}$ = 700 GeV, $M_{\tilde{q}}$ = 700 GeV, $M_{\tilde{\chi}_1^0}$ = 150 GeV). Lower Left: Jet η distribution for UED MC signal events. Lower Right: Jet η distribution for GGM MC signal events.

7.4.3.2 Effect of Jet Requirement on Efficiency

A study was performed to determine if the addition of the jet requirement would have an adverse effect on the efficiency. Both GGM SUSY and UED events contain numerous jets. Figure 7.5 shows the distribution of jet multiplicity per event in the $\gamma\gamma$ sample for a GGM and UED sample point. As very few diphoton events would not pass the jet requirement making the loss in efficiency negligible.

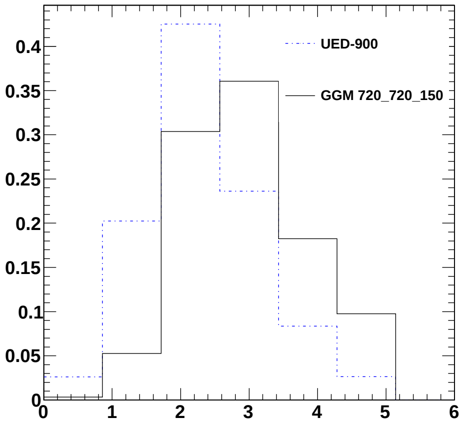

Figure 7.5: The number of jets per event for a GGM sample point with $M_{\tilde{g}} = 720$ GeV,$M_{\tilde{q}} = 720$ GeV,$M_{\tilde{\chi}_1^0} = 150$ GeV and a UED sample point with (1/R = 900 GeV. Very few events have zero jets, making the loss of efficiency negligible.

Figure 7.6 shows the effect of the chosen value of the $\Delta R > 0.9$. A typical GGM point, $M_{\tilde{g}} = 640$ GeV, $M_{\tilde{q}} = 640$ GeV, $M_{\tilde{\chi}_1^0} = 150$ GeV, was chosen and the efficiency was plotted for increasing numbers of jets. As the number of jets increases, the average distance of the closest jet to the lead photon decreases. As jets begin to overlap photons, the photons are no longer considered isolated, failing the ECAL and HCAL isolation cuts. As Figure 7.6 shows, the photon efficiency goes to zero as $\Delta R = 0.5$. For all values above 0.5 the photon efficiency is flat, indicating that our choice of 0.9 for the ΔR cut

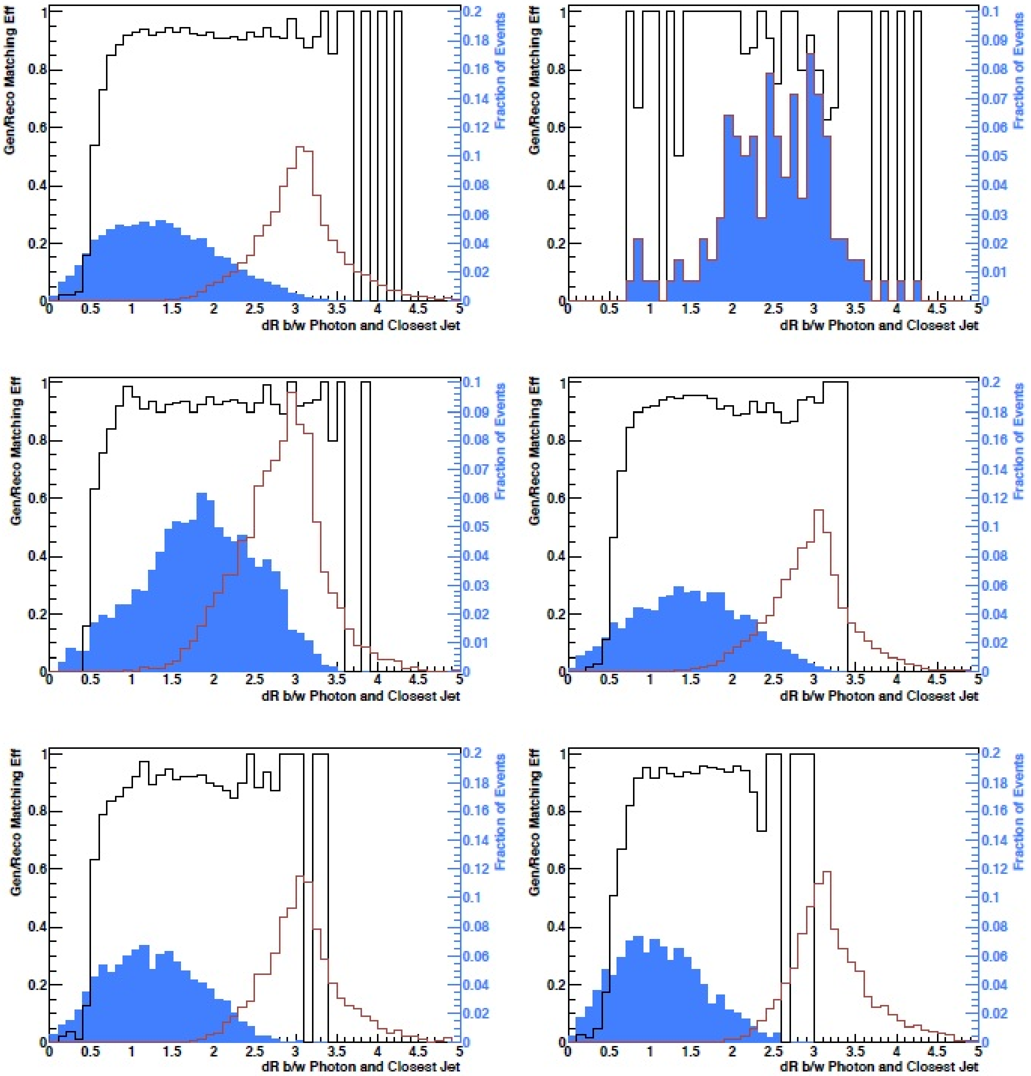

Figure 7.6: The black histogram shows the event efficiency as a function of the ΔR cut. The blue solid histogram is the normalized distribution of distances from the lead photon to the closest jet. The red histogram is the normalized distribution of distances from the lead photon to the most distant jet. Plots for up to six jets per event are shown. 1st Row Left: $N_{jets} = 1$; 1st Row Right: $N_{jets} = 2$; 2nd Row Left: $N_{jets} = 3$; 2nd Row Right: $N_{jets} = 4$; 3rd Row Left: $N_{jets} = 5$; 3rd Row Right: $N_{jets} = 6$.

has no significant effect on the efficiency.

7.4.3.3 Selection Cut Effects on Efficiency for GGM Signal

Each of the selection cuts used by the analysis has some effect on the overall acceptance times efficiency of the analysis. Signal MC events were used to identify where these losses occur. Figure 7.7 shows a breakdown of the losses in efficiency at different stages of the selection process. As can be seen, at the generator level, the initial efficiency for events with two 30 GeV E_T photons in the ECAL barrel is approximately 70%. The reconstruction efficiency is nearly 100% and causes no appreciable losses. The application of the isolation cuts causes the largest reduction in efficiency, lowering the efficiency to below 30%. Figure 7.7 also shows that the efficiency lost due to the isolation cuts increases as the number jets from quark/gluon decays increases. This agrees with the results of the study done in Section 7.4.3.2.

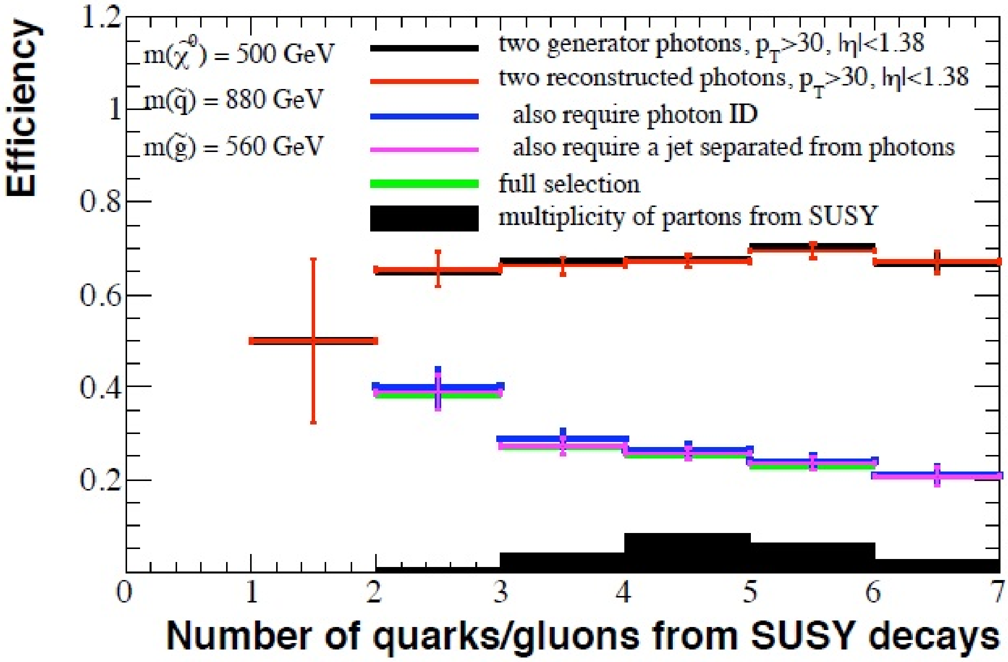

Figure 7.7: Losses to acceptance due to selection cuts for a typical GGM point ($M_{\tilde{g}} = 560$ GeV,$M_{\tilde{q}} = 880$ GeV, $M_{\tilde{\chi}_1^0} = 500$ GeV)

7.4.4 Determination of Acceptance times Efficiency

While the topology of GGM and UED events is similar, there are some kinematic differences that cause a difference is overall acceptance times efficiency between the two models. These kinematic differences are due to the different masses of the GGM and UED counterparts. The masses of GGM and UED equivalents are shown in Table 7.8.

Table 7.8: GGM and UED particle comparison. Particles are grouped by their topological equivalent. Masses for UED (1/R=700) point shown. Masses for GGM ($M_{\tilde{g}} = 1040$ GeV, $M_{\tilde{q}} = 640$ GeV, $M_{\tilde{\chi}_1^0} = 50$ GeV) point shown.

GGM Particle	Mass (GeV)	**UED Particle**	Mass (GeV)
Gluino ($\tilde{g}$)	1040	KK Gluon (g^*)	865
Squark ($\tilde{q}$)	640	KK Quark (q^*)	800
Neutralino ($\tilde{\chi}_1^0$)	50	KK Photon (γ^*)	700
Gravitino ($\tilde{G}$)	$< 10^{-6}$	Graviton (G$^{(*)}$)	> 400

7.4.4.1 GGM

In order to determine the acceptance times efficiency for each GGM point, the entire analysis chain was performed on 10000 MC events for each parameter point. The acceptance times efficiency is then calculated as:

$$\text{Acc.} \times \text{Eff.} = \frac{\text{Number of events passing all selection cuts}}{\text{Number of generated events}} \cdot (\text{Photon Scale Factor})^2 \tag{7.1}$$

where the photon scale factor, determined in Section 6.5.2.2, is taken to be 0.987. The resulting acceptances for all generated GGM points are shown in Figure 7.8.

7.4.4.2 UED

The acceptance times efficiency as a function of $1/R$ was then determined from seven MC sample points over the range $700 < 1/R < 1000$ GeV. The procedure for calculating the acceptance times efficiency was the same as used for the GGM points (Equation 7.1). For the range off generated point the acceptance times efficiency varied between 29% and 32% and is shown in Figure 7.9.

7.4.4.3 Comparison of GGM and UED Efficiencies

After analysis of the two models, it is shown that the UED model has, in general, a higher efficiency than GGM. This can be explained by the kinematic differences between GGM and UED events. As was shown in Section 7.4.3.3, a loss in efficiency occurs as jets overlap photons causing the isolation cuts to fail. As can be seen in Figure 7.10, the jets in GGM events tend to be closer to the photons than in UED events. This

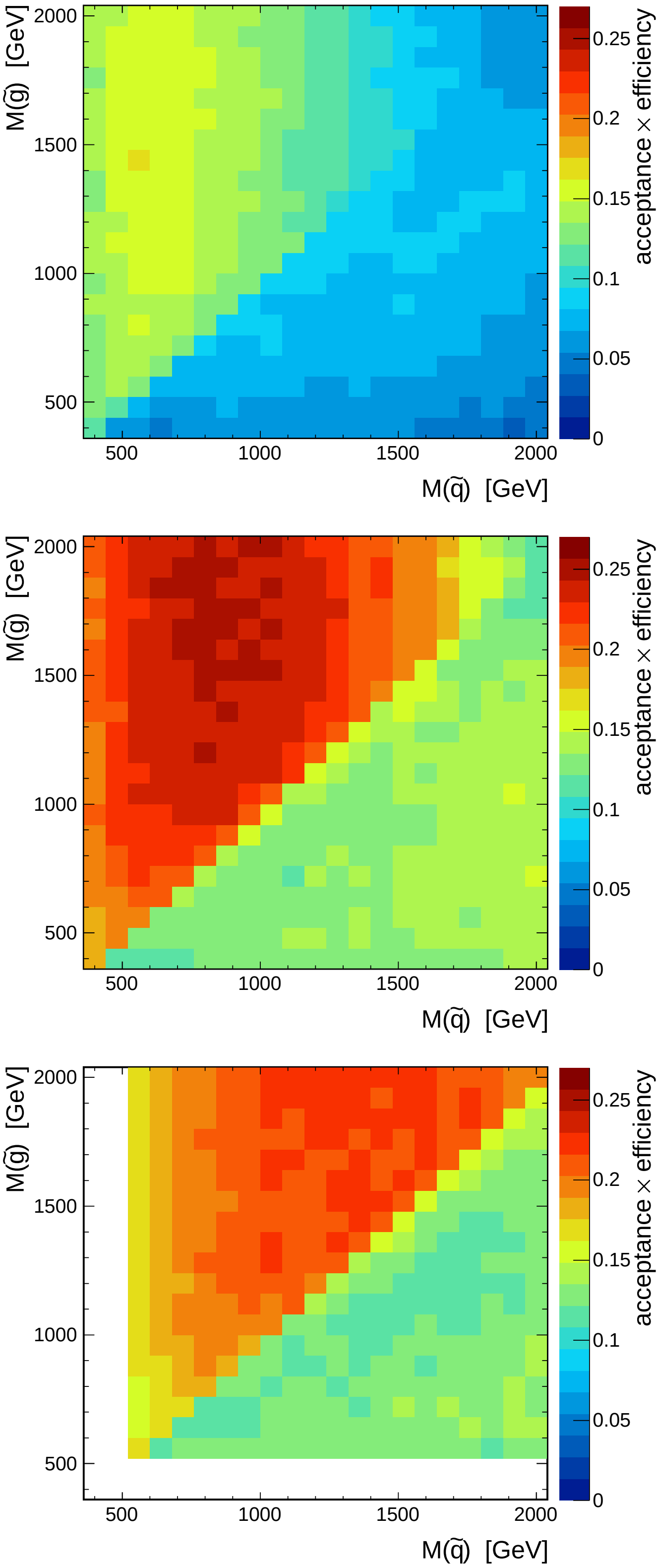

Figure 7.8: Acceptance times efficiency for all generated GGM points. Upper: Points with $M_{\tilde{\chi}_1^0} = 50$ GeV. Middle: Points with $M_{\tilde{\chi}_1^0} = 150$ GeV. Lower: Points with $M_{\tilde{\chi}_1^0} = 500$ GeV.

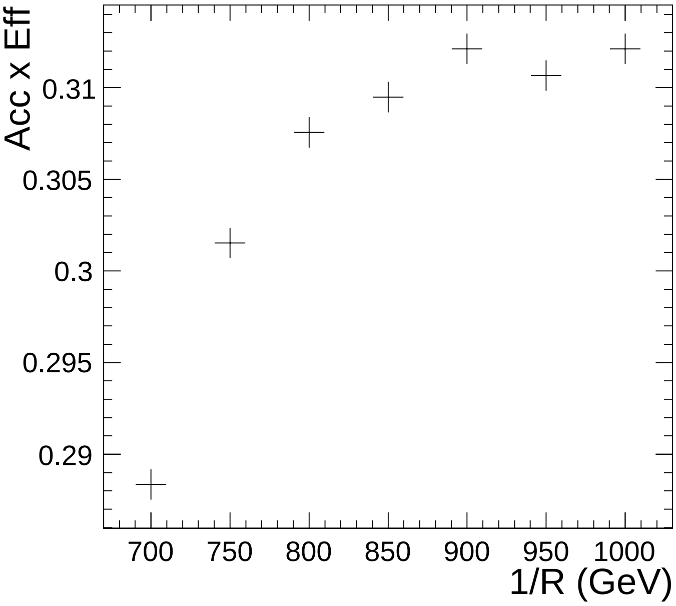

Figure 7.9: Acceptance times efficiency for seven generated UED points.

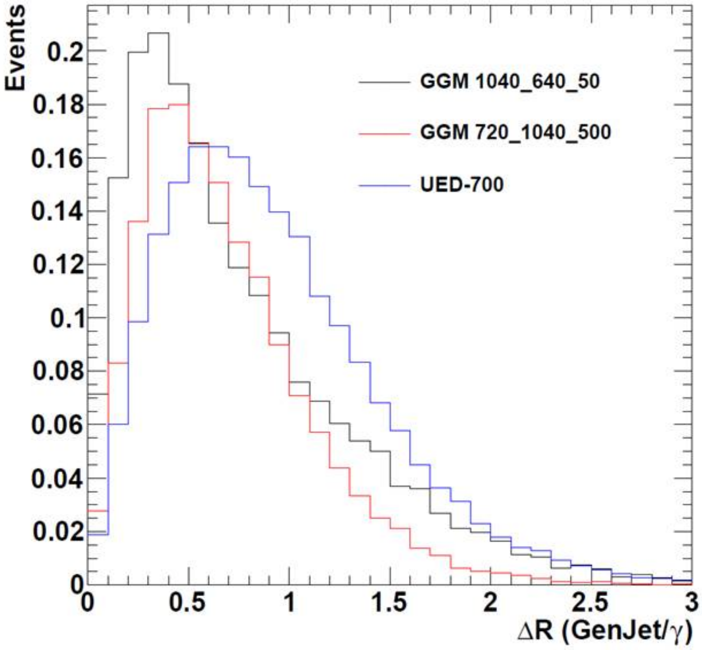

Figure 7.10: Minimum distance between photon and jet for two GGM points and on UED point. Event counts were normalized to one.

causes more frequent jet-photon overlaps and therefore lower efficiency.

Chapter 8

Estimation of Backgrounds

8.1 QCD

The largest background in the diphoton and E_T^{miss} channel comes from processes involving the strong force. These processes described by Quantum Chromodynamics (QCD) can produce photons and jets. The jets, however, can be misidentified as photons and mimic the diphoton signal. Also, QCD events have no true large E_T^{miss}. However, since the energy resolution in the ECAL is much better than in the HCAL, a miscalculation of E_T^{miss} can occur.

8.1.1 QCD Template

In order to model the contribution to the signal from QCD events a "template" method was used. QCD events should have no true E_T^{miss}. The measured E_T^{miss} is due to the difference in energy resolution between the ECAL and the HCAL. The ECAL energy resolution is far superior to the HCAL energy resolution. Two types of kinematically similar (i.e. having two EM-like objects) events with no true E_T^{miss} were selected: $Z \to ee$ and events with two "fake" photons (ff) as defined previously. We use two control samples to verify the consistency of the method.

For QCD and $Z \to ee$ events, the EM objects recoil against the hadronic activity in the event (Fig. 8.1). Therefore the E_T^{miss} measured is correlated to the sum of the EM objects p_T. As the $\gamma\gamma$ di-EM E_T spectrum (Fig. 8.2) is different from the di-EM E_T spectrum for electrons and fakes, we re-weight the E_T^{miss} distribution. As di-EM P_T and E_T^{miss} are correlated, the di-EM E_T is the natural choice for re-weighting.

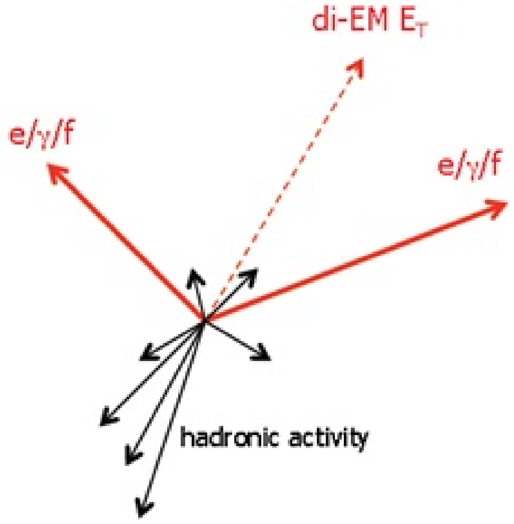

Figure 8.1: The di-EM p_T is recoiling against hadronic activity in the event.

To obtain the weights to be applied to the E_T^{miss}, the ratio of the di-EM p_T between the ff or ee events and the $\gamma\gamma$ events is computed bin by bin (Fig. 8.3). A linear fit is then performed to determine the re-weighting values as a function of the di-EM p_T. A two-dimensional histogram, di-EM p_T vs. E_T^{miss}, is generated to get the number of events for each E_T^{miss} bin for each range of di-EM p_T. The di-EM p_T vs. E_T^{miss} distributions for $Z \to ee$ and "fake-fake" events are shown in 8.4. Using these

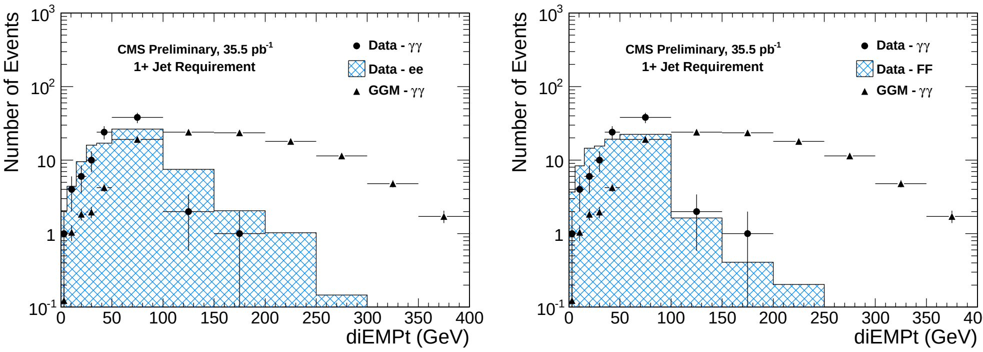

Figure 8.2: Left: Di-EM p_T for ee sample. Right: Di-EM p_T for ff sample.

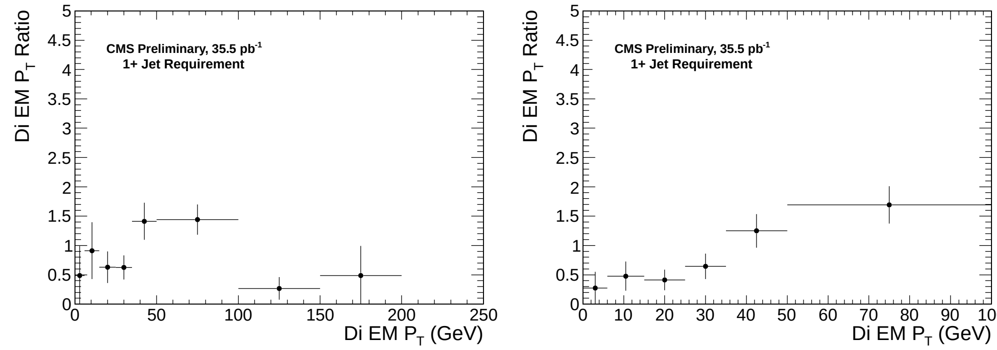

Figure 8.3: Ratio of di-EM p_T distributions. Left: ee sample. Right ff sample.

distributions, each bin is re-weighted and a new E_T^{miss} distribution is produced.

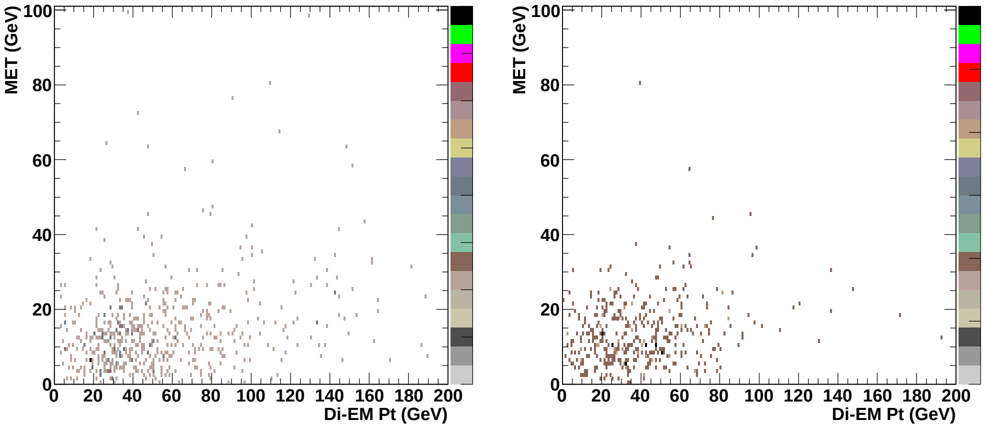

Figure 8.4: Two dimensional histograms are used to re-weight the E_T^{miss} distribution as a function of its di-EM p_T. Left: Di-EM p_T vs. E_T^{miss} for ee sample. Right Di-EM p_T vs. E_T^{miss} for ff events.

The re-weighted E_T^{miss} distribution must then be normalized to account for the difference in the numbers of ff or ee events versus $\gamma\gamma$ events. As it is assumed that events with low E_T^{miss} contain no new physics, we can then normalize the numbers of events based on this region without affecting the signal region. The re-weighted E_T^{miss} distribution is therefore normalized to the candidate sample based on the first four bins, $E_T^{miss} < 20$ GeV.

To propagate the error through the re-weighting and normalization process, 1000 “pseudo-experiments” are performed. For each iteration, the bins in the di-EM p_T ratio are varied using a gaussian distribution and a new re-weighting function is determined. The central value is taken to be the E_T^{miss} distribution using the unvaried re-weighting function. The systematic error for each bin is computed by counting the number of fluctuations above and below the central value. The distance from the central value of each bin which contains 68% of the fluctuations is then determined. The distance represents a one sigma error in the number of events in each E_T^{miss} bin. The fluctuations above and below are used separately to determine the positive and negative errors allowing for the errors to be asymmetric.

8.1.2 QCD Estimation Results

Using the $Z \rightarrow ee$ template, the expected QCD background with $E_T^{miss} > 50$ GeV is determined to be 1.67 ± 0.64 events. From the "fake-fake" template we predict 0.49 ± 0.37 events. A complete breakdown of the QCD estimate and errors is shown in Table 8.1.

Table 8.1: Estimated QCD numbers of events in the data sample using the two control templates.

Type	Number of Events	Statistical Error	Re-weight Error	Normalization Error
QCD background estimate (ff)	0.49 ± 0.37	± 0.36	± 0.06	± 0.07
QCD background estimate (ee)	1.67 ± 0.64	± 0.46	± 0.38	± 0.23

8.2 Electroweak

The contribution to the background due to electroweak (EWK) processes must also be considered. The EWK processes that can contribute to the signal are $W\gamma$, $W + jets$, $W\gamma\gamma$, and $Z\gamma\gamma$ where the W decays to an electron and a neutrino and the Z decays to two neutrinos. Events involving W's and Z's have true E_T^{miss} due to the neutrinos escaping undetected. The $W\gamma$ and $W + jets$ events require the electron to be misidentified as a photon and, in the case of $W + jets$, a jet also to be misidentified as a photon. The $W\gamma\gamma$ and $Z\gamma\gamma$ events, requiring no misidentification, are an irreducible background; however the production cross sections for these processes are so small as to be negligible, as shown in Table 8.2.

Table 8.2: The number of predicted $W\gamma\gamma$ and $Z\gamma\gamma$ events provided no significant source of background. The number of expected events shown here assumes 100% efficiency.

Process	Cross section (fb)	Expected Events (35.5 pb^{-1})
$W\gamma\gamma$	10.39	0.368
$Z\gamma\gamma$	5.127	0.182

8.2.1 $e\gamma$ contribution

To determine the number of electroweak events in our $\gamma\gamma$ sample we use the photon fake rate determined in Section 6.5.1 along with the number of events in the $e\gamma$ sample. Assuming that the $e\gamma$ sample is dominated by W decays, one can infer the number of $e\gamma$ events that appear in the $\gamma\gamma$ sample.

If we define the following values: the probability of an electron being misidentified as a photon, f_e, the number of actual $W\gamma$ events, $N_{W\gamma}$, and the number of events in $e\gamma$ sample, $N_{e\gamma}$, then we can write the following relations.

The number of true $W\gamma$ events.

$$N_{W\gamma} = N_{e\gamma}/(1 - f_e) \tag{8.1}$$

The number of $W\gamma$ events misidentified as $\gamma\gamma$.

$$N_{fake\gamma\gamma} = N_{e\gamma} \cdot f_e \tag{8.2}$$

Combining equations 8.1 and 8.2 we can get the total contribution to the $\gamma\gamma$ sample in terms of the number of $e\gamma$ events.

$$N_{fake\gamma\gamma} = N_{e\gamma} \cdot \frac{f_e}{(1 - f_e)} \tag{8.3}$$

Then to determine the EWK contribution to the E_T^{miss} distribution for $\gamma\gamma$ events, we can scale at the E_T^{miss} distribution of $e\gamma$ events by $\frac{f_e}{(1-f_e)}$. The estimated EWK contribution to the $\gamma\gamma$ sample with $E_T^{miss} > 50$ GeV is 0.04 ± 0.15.

8.2.1.1 Jet fake rate

A study was performed by the CMS Exotica Photon group to determine the rate at which jets are misidentified as photons [38]. Several methods, some MC based and some data-driven, were used in the study. It was shown that the fake rate is dependent on the p_T of the jet. The results are shown in Figure 8.5.

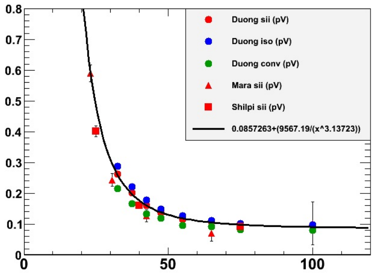

Figure 8.5: Jet fake rate as a function of jet p_T as determined by the CMS Exotica Photon Group.

8.2.2 Electroweak Background Closure

In order to test our data-driven method of determining the electroweak contribution, a study was performed using $W\gamma$ and $W + jets$ MC. The E_T^{miss} distribution for the $e\gamma$ sample should be comprised of the contributions, from $W\gamma$ and $W + jets$. The $W\gamma$ events contribute directly to the $e\gamma$ sample while the $W + jets$ must have a jet misidentified as a photon. To determine the number of $W + jets$ events with misidentified jets, we scale the E_T^{miss} for the $W + jets$ MC by the jet/photon fake rate. Because of the limited statistics, the jet requirement was not used in this study.

The LO cross section for $W\gamma$ production is 54.5 pb and the LO cross section for $W + jets$ in 26.5 nb. MC samples for $W\gamma$ and $W + jets$ contained 165000 and 5.66 million events, respectively. These samples were then scaled to 35.5 pb, and the

$W\gamma$ sample was multiplied by a k-factor of 1.8 to account for next leading order (NLO) production, and the $W + jets$ sample is multiplied by the jet/photon fake rate. The E_T^{miss} distribution for the $e\gamma$ sample is then plotted, along with the estimated QCD contribution to $e\gamma$ and the appropriately scaled MC samples for $W\gamma$ and $W + jets$. This plot is shown in Figure 8.6. As can be seen the background estimate matches well to the data.

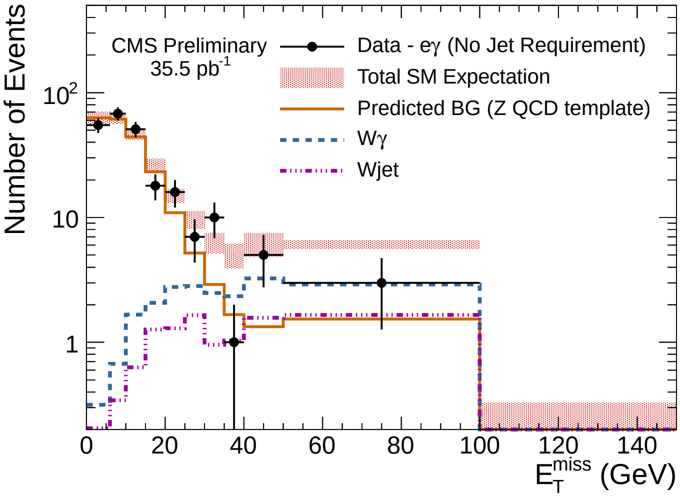

Figure 8.6: The E_T^{miss} distribution of the $e\gamma$ sample, without jet requirement, is plotted against the total background prediction coming from the data-driven QCD estimate (using $Z \rightarrow ee$ events) and the MC EWK samples.

8.3 Background Closure

Combining the contributions from the QCD and EWK estimate we can calculate our total background expectations. Using an average of the $Z \rightarrow ee$ and ff templates and adding the EWK contribution, we estimate the total background to be 1.2 ± 0.8 events. Figure 8.7 shows the 2010 data with the background estimate and expected signal for both the GGM and UED models.

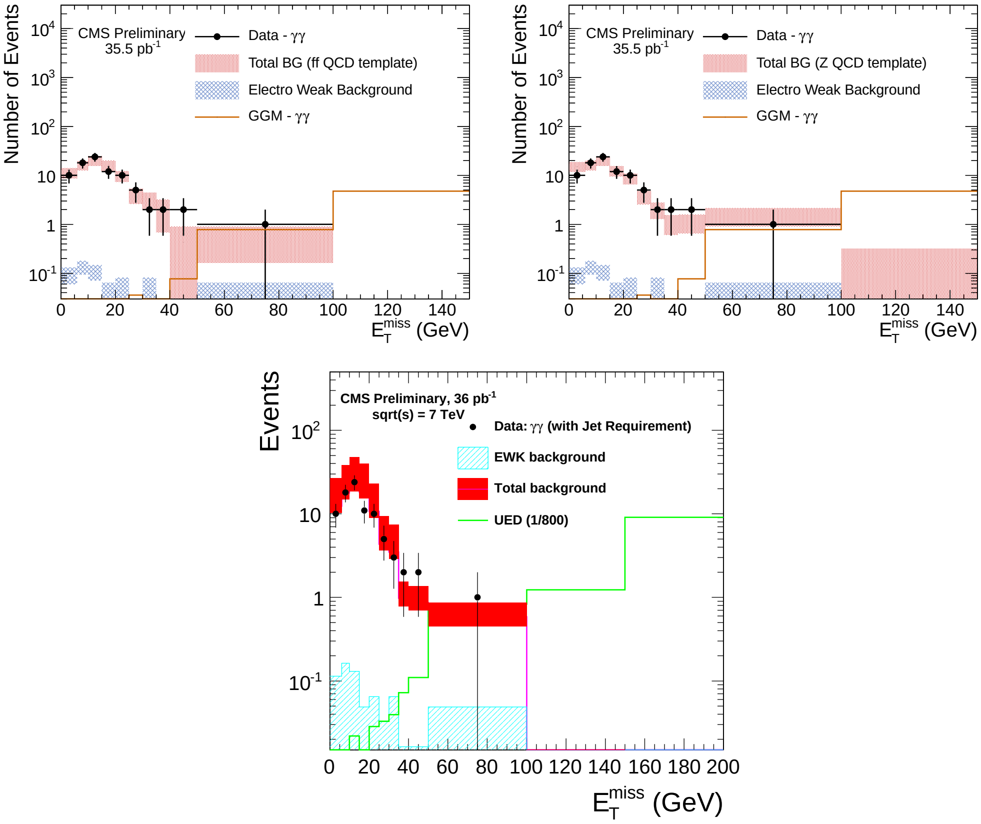

Figure 8.7: The background closure plots show 36 pb^{-1} of data with estimated background and expected signal for GGM (top plots) and UED lower plot.

Chapter 9

Determination of Limits

As no signal of physics beyond the standard model was observed, we can place bounds on the cross section and parameters of the models studied. A Bayesian method was used to determine the cross sections that can be excluded at the 95% confidence limit (CL). The cross section limits are then parameterized in terms of squark, gluino, and neutralino masses for the GGM model and compactification radius for the UED model.

9.1 Uncertainties

The calculations for the cross section upper limits are dependent on several parameters which have some associated uncertainties. The uncertainties are listed in Table 9.1.

9.1.1 Acceptance

The uncertainty on the acceptance is comprised of several components. The uncertainty on the photon scale factor, described in Section 6.5.2.2 and uncertainty due

Parameter		Total Err.
Luminosity	35.5	4.0
Acceptance		2.6
	Pile-up	1.1 %
	Photon/Electron Differences	0.5 %
	Jet Energy Scale	2.0 %
	PDF Acceptance	varies %

Table 9.1: Uncertainties used in limit calculation. The individual uncertainties comprising the Acceptance × Efficiency uncertainties are listed in the second column.

to pixel seed veto efficiency, from Section 6.2.6, is presented as a combined 0.5% for photon/electron differences. Uncertainty due to pileup, computed in Section 6.5.2.3, is taken as 1.1%. Uncertainty on the jet energy scale, 2.0%, is determined in Section 7.3.3.1. The uncertainty on acceptance due to the use of parton distribution functions, described below, varies based on squark and gluino masses.

9.1.1.1 Parton Distribution Functions

At any hadron collider, the total energy of the collision is not known as the colliding particles are composite objects, with each parton carrying some fraction of the momenta. To account for this effect, we use parton distribution functions (PDFs), that model the distribution of momenta in the proton. There are uncertainties associated with the use of PDFs that affect the calculation of cross sections and acceptances and their associated uncertainties.

At the LHC, we take the three most common PDFs that use results from the Tevatron and fixed target experiments: NNPDF, MRST2001, CTEQ6. Each event in our MC sample is given weight corresponding to the values and errors in the PDF associated with the initial parton distribution [39]. These weights are then used to determine the rate and acceptance by determining the number of re-weighted events before and after the selection. For each PDF, these weights yield an error both on the cross section and on the acceptance. An "envelope" method is used, where the central value is chosen as the midpoint of the envelope and one σ uncertainty is used as the error:

$$x = \frac{1}{2}(max(x1 + s1, x2 + s2, x3 + s3) + min(x1 - s1, x2 - s2, x3 - s3)) \tag{9.1}$$

$$s = \frac{1}{2}(max(x1 + s1, x2 + s2, x3 + s3) - min(x1 - s1, x2 - s2, x3 - s3)) \tag{9.2}$$

where x1, x2, and x3 are the central values of the three different PDFs, and s1, s2 and s3 are their uncertainties.

This procedure was performed using generator level photons with $p_T > 30$ GeV and requiring one jet with $p_T > 30$ GeV . Acceptance uncertainties were calculated for each GGM point and are shown in Figure 9.1. For most of the GGM the uncertainties are less than 5%, with only at larger squark and gluino masses having larger uncertainties.

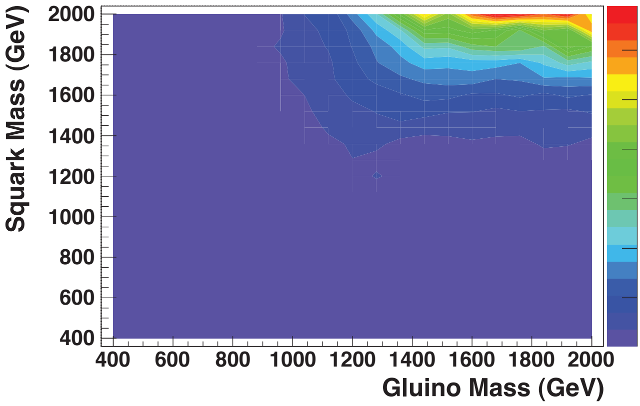

Figure 9.1: PDF acceptance uncertainties as a function of squark and gluino mass.

For the UED model, we assume that the PDF uncertainties will be similar for corresponding KK gluon and KK quark masses. The values used for the seven UED points are listed in Table 9.2.

(1/R) GeV	$M_{\tilde{g}}$	$M_{\tilde{q}}$	PDF Acceptance (%)	PDF Cross section (%)
700	800	865	0.2048	12.88
750	855	926	0.2346	13.64
800	910	986	0.2346	13.64
850	967	1046	0.2261	14.41
900	1025	1107	0.2203	15.13
950	1080	1167	0.2063	17.74
1000	1135	1227	0.3662	16.39

Table 9.2: PDF uncertainties for UED points.

9.2 Cross Sections

To determine the limit for each model in terms of its parameters, the cross sections must be known. Cross sections are determined by PYTHIA at leading order (LO) during the generation process for both GGM and UED points. In the case of the UED points the cross section was fit with an exponential function to parameterize the cross section in terms of the 1/R parameter. In the case of GGM cross sections, next to leading (NLO) corrections, known as k-factors, were generated using PROSPINO [40] and are shown in Figure 9.3. Due to the fact that PROSPINO was designed for use with supersymmetric models and may not be valid for other models, no k-factors were used for UED cross sections.

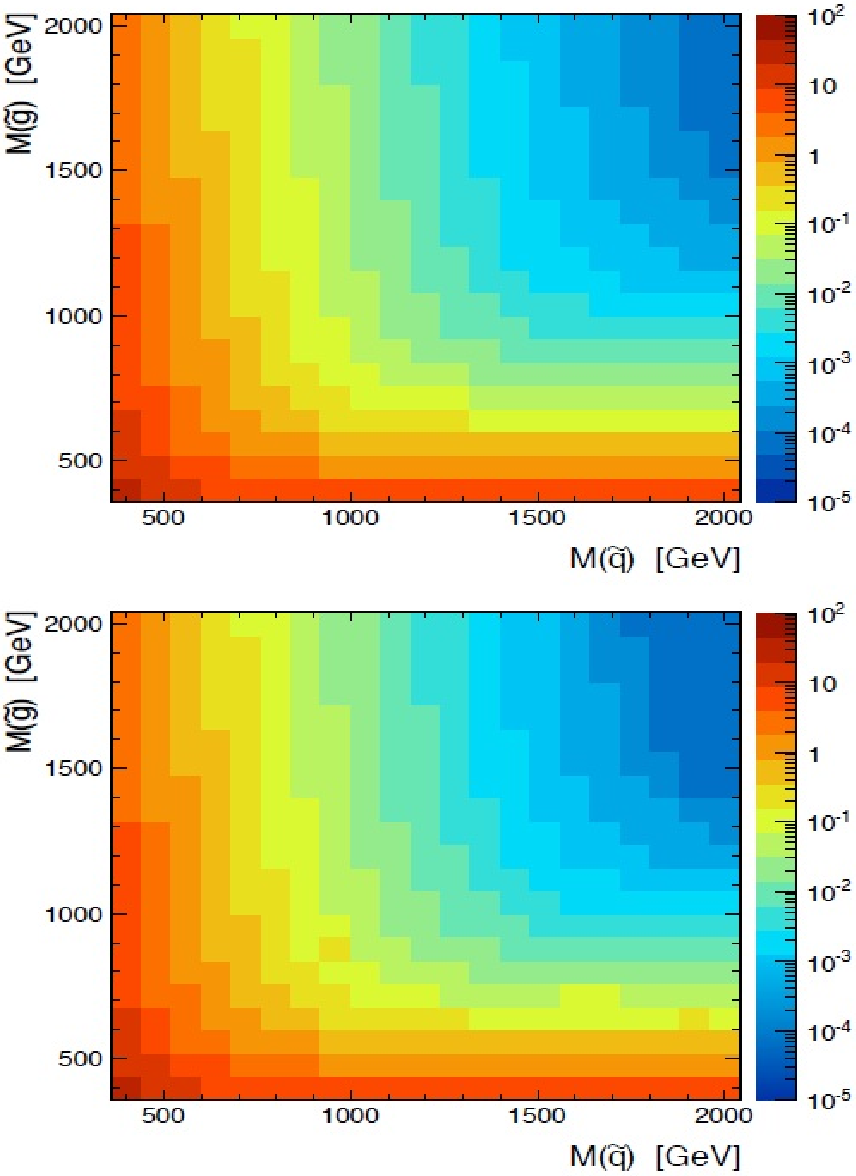

Figure 9.2: PYTHIA LO cross sections for GGM production as a function of squark and gluino mass with a neutralino mass of 50 GeV (top) and 150 GeV (bottom).

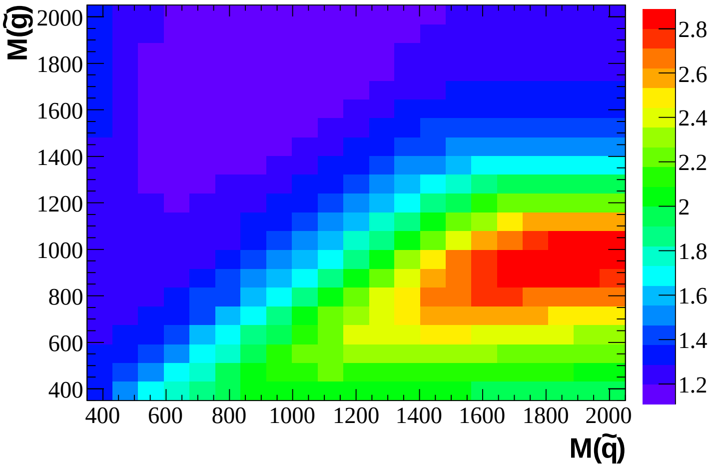

Figure 9.3: NLO corrections to the PYTHIA LO cross sections for GGM production, known as k-factors, were generated using the PROSPINO program. The k-factors are presented in for each GGM point based on squark and gluino mass.

9.2.1 Cross Section PDF Uncertainties

The uncertainty due to the use of PDFs, in addition to affecting the acceptance, also affect our ability to measure cross sections. While the PDF cross section uncertainty does not directly affect the calculation of a cross section limit, it does interfere with our ability to determine exclusion ranges in terms of model parameters. As PDF cross section uncertainties can be quite large, this can have a significant effect and must be considered. Figure **??** shows the PDF cross section uncertainties for GGM points as a function of squark and gluino mass. PDF cross section uncertainties for UED models were, as for PDF acceptance uncertainties, assumed to be the same for similar particle masses and are shown in Table 9.2.

9.3 Bayesian Methods

We use a Bayesian method for determining upper limits, as described in [41]. The result given by this analysis is the observation of some number of events (N) with

$E_T^{miss} > 50$ GeV in the $\gamma\gamma$ sample. The probability that the production cross section of the model is σ, given N observed events is can be expressed by Bayes' theorem:

$$p(\sigma|N) = \frac{L(N|\sigma)\pi(\sigma)}{\int L(N|\sigma')\pi(\sigma')d\sigma'} \tag{9.3}$$

where $L(N|\sigma)$ is the "Likelihood", the probability distribution function (p.d.f.) to observe N given a production cross section σ. $\pi(\sigma)$ is the prior p.d.f., based on our knowledge of σ. For this analysis, we use a "flat" prior, defined as:

$$\pi(\sigma) = \begin{cases} 0 & \text{if } \sigma < 0 \\ 1 & \text{if } \sigma \geq 0 \end{cases} \tag{9.4}$$

This simple prior assumes only that the cross section is non-negative.

The Likelihood function is based on three parameters: luminosity (l), estimated background (b), and the acceptance times efficiency (ε). These values have associated uncertainties that must be incorporated. To account for these uncertainties we model the parameters with different p.d.f.'s, where the central value is the parameter and $\pi(l)$, $\pi(b)$, and $\pi(\varepsilon)$ are the distributions with standard deviations equal to the error. The Likehood function then becomes:

$$L(N|\sigma) = \int L(N|\sigma, l, \varepsilon, b)dld\varepsilon db \tag{9.5}$$

where, using the Poisson distribution,

$$L(N|\sigma, l, \varepsilon, b) = \frac{(\sigma l\varepsilon + b)^N}{N!}e^{-(\sigma l\varepsilon + b)} \tag{9.6}$$

Three different p.d.f. shapes were tested: Gaussian, log-normal, and gamma. For one observed event passing all selection cuts, the maximum cross section at the 95% confidence level can be calculated from:

$$0.95 = \int_0^{CL95} p(\sigma|1)d\sigma = \frac{\int_0^{CL95}(\sigma l\varepsilon + b)e^{-(\sigma l\varepsilon+b)}\pi(l)\pi(b)\pi(\varepsilon)dld\varepsilon dbd\sigma}{\int_0^{\inf}(\sigma' l\varepsilon + b)e^{-(\sigma' l\varepsilon+b)}\pi(l)\pi(b)\pi(\varepsilon)dld\varepsilon dbd\sigma'} \tag{9.7}$$

where $CL95$ is the maximum cross section.

9.4 GGM Limit Calculations

As acceptances and PDF uncertainties vary for each point in the GGM grid, each point has its own cross section upper limit, which is compared to the production cross section to determine if the point is excluded. All points use an assumption of 36 ± 3.9 pb^{-1} of integrated luminosity and 1.2 ± 0.8 events of estimated background (Chap. 8). A sample of this calculation, for a particular sample point, is presented in Section 9.4.1. The complete grid of cross section upper limits, for the three different neutralino masses, are shown in Figure 9.4. The upper limit on the production cross sections of GGM to between 0.3 and 1.1 pb.

9.4.1 Cross Section Limit for GGM Sample Point

As an example, we choose a GGM point with $M_{\tilde{g}} = 720$ GeV, $M_{\tilde{q}=720}$ GeV, and $M_{\tilde{\chi}_1^0=150}$ GeV. The NLO cross section, including a k-factor of 1.45, is 0.712 pb, with uncertainties due to PDF of 18.4% and renormalization scale of 13%. The acceptance times efficiency for this point is $0.218 \pm 0.0041(stat) \pm 0.0054(syst.)$. This implies, for 36 pb^{-1}, an expectation of 5.5 ± 1.2 observed events. Using the total background estimation from Secton 8.3, we calculate the cross section upper limit at 95% CL, using Equation 9.7, to be 0.557 pb, 0.544 pb, and 0.536 pb, using the Gaussian, log-normal, and gamma distributions, respectively.

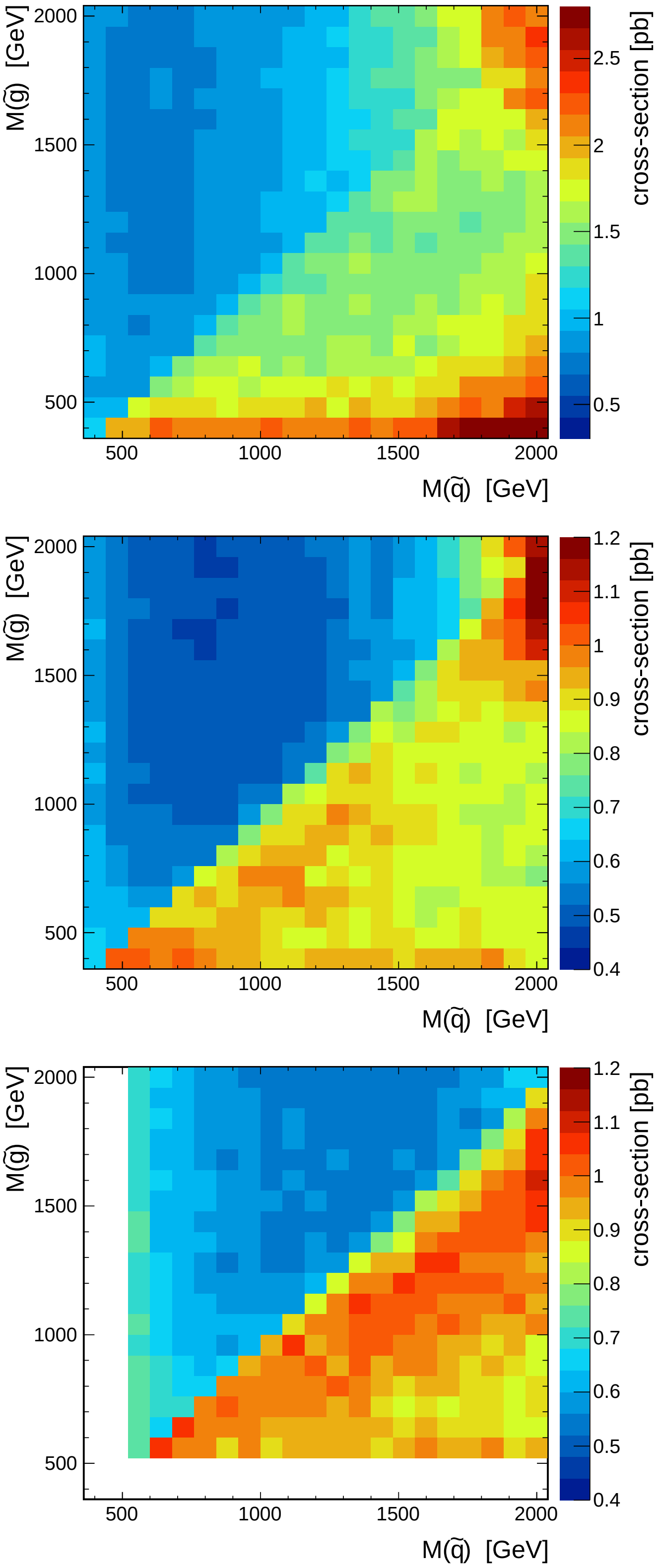

Figure 9.4: Maximum GGM cross sections at the 95% CL. Upper: $M_{\tilde{\chi}_1^0} = 50$ GeV. Middle: $M_{\tilde{\chi}_1^0} = 150$ GeV. Lower: $M_{\tilde{\chi}_1^0} = 500$ GeV

9.4.2 GGM Exclusion Region

Comparing the calculated cross section upper limit, Figure 9.4 and production cross sections, Figure 9.2, we identify the point of exclusion in the squark and gluino mass grid. This is done for the three different neutralino masses, with and without the use of k-factors, and is shown in Figure 9.5. The upper plot includes the use of k-factors and indicates uncertainty in the cross section due to PDFs and renormalization scale as the hatched region. The lower plots shows the exclusion contours, without k-factors, for LO cross sections.

9.5 UED Limit Calculations

The cross section upper limit for UED production can be calculated in the same way as for GGM, using Equation 9.7. The maximum UED productions cross section is computed using the acceptance times efficiency from Figure 7.9 and the same luminosity and background as for the GGM calculation. The UED cross sections, shown in Section 9.2, and the CL95 cross section upper limit are interpolated and their intersection is determined. This intersection is shown in Figure 9.6. Uncertainty due to PDFs and renormalization scale is shown as the shaded region, while the intersection of the central value implies that all values of $1/R < 889$ GeV are excluded.

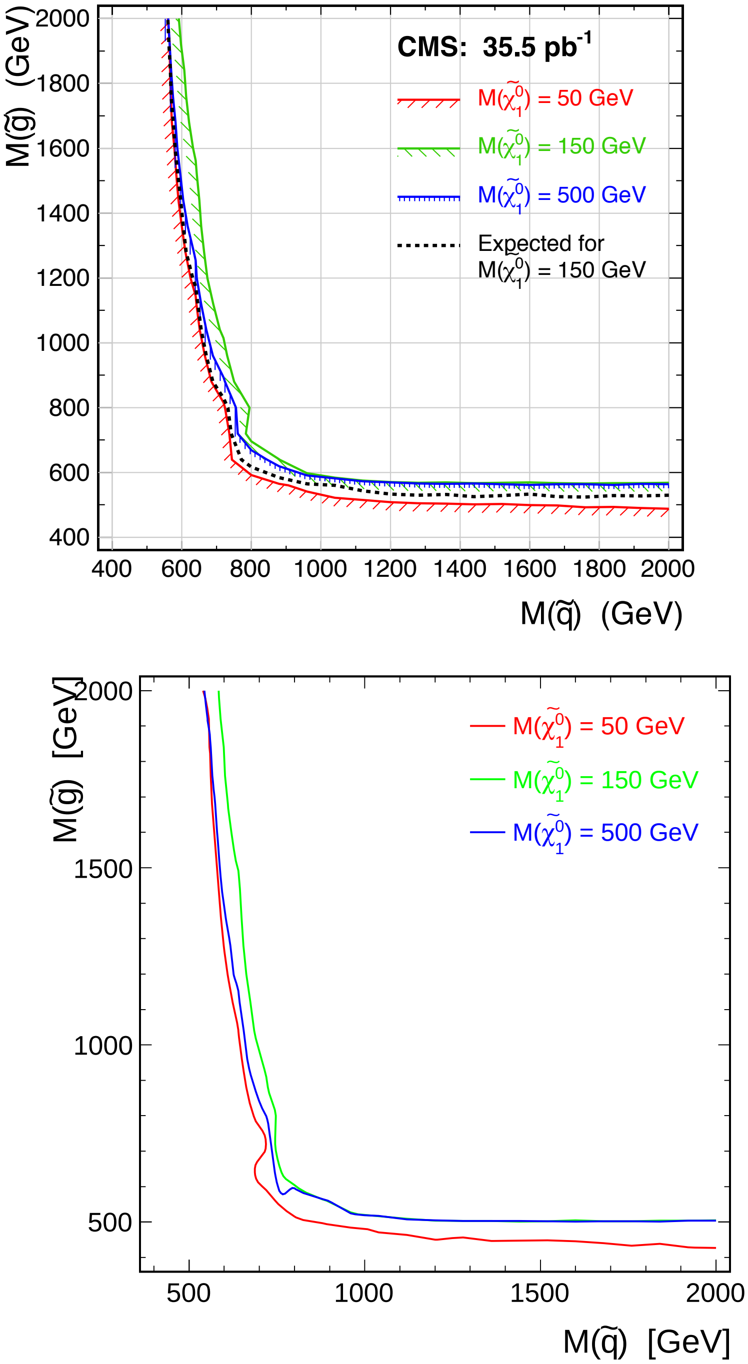

Figure 9.5: GGM exclusion regions at the 95% CL. Upper: Exclusion contour including k-factors and uncertainties. Lower: Exclusions contours for LO cross sections, without k-factors.

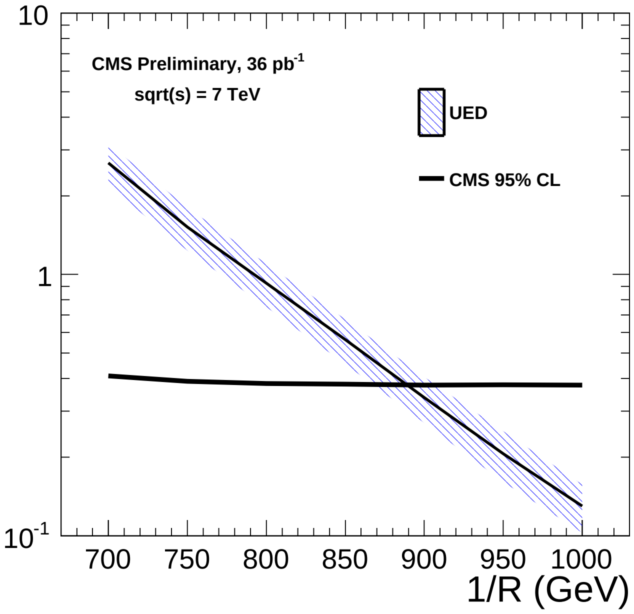

Figure 9.6: The UED cross section upper limit at the 95% CL is compared with UED LO production cross sections. Intersection of the central cross section value implies all values of $1/R < 889$ are excluded. The shaded region shows uncertainty due to PDFs and renormalization scale.

Chapter 10

Conclusions

This search for new physics in 36 pb^{-1} of data using diphoton events observed one event with $E_T^{miss} > 50$ GeV. The computed background expectation using two control samples, $Z \to ee$ events and events with two "fake" photons, was 1.67 ± 0.64 events and 0.49 ± 0.37 events, respectively, for a combined estimate of 1.2 ± 0.8 events. As the observed one event agrees with well with the estimated background we state that no signal for new physics was detected in the diphoton plus E_T^{miss} channel.

This result was interpreted in two theoretical models for physics beyond the standard model, General Gauge Mediation and Universal Extra Dimensions. For both models the predicted cross sections for various scenarios in terms of model parameters, gluino, squark, and neutralino for GGM and radius of compactification (1/R) for UED, were used to set upper limits at the 95% CL. GGM cross section upper limits were set to between 0.3 and 1.1 pb, which are the world's best limits for GGM production set to date[42]. The excluded regions in terms of the GGM parameters is shown in Figure 9.5. The UED exclusion region in terms of the radius of compactification at the 95% CL is 1/R $<$ 889 GeV and is shown in Figure 9.6. This limit exceeds the limit set by the previous two published analyses[43, 37] and is also the world's best limit to date.

Bibliography

[1] CMS, "CMS Website," 2011, http://cms.web.cern.ch/cms/Media/Images/Detector/index.html.

[2] C. Macesanu, C. D. McMullen, and S. Nandi, "New signal for universal extra dimensions," *Phys. Lett.*, vol. B546, pp. 253–260, 2002.

[3] C. W. N.R. Shah, "Gravitons and Dark Matter in Universal Extra Dimensions," *Phys. Rev. D*, vol. 74, p. 104008, 2006.

[4] C. Macesanu, C. D. McMullen, and S. Nandi, "Collider implications of universal extra dimensions," *Phys. Rev.*, vol. D66, p. 015009, 2002.

[5] L. Evans and P. Bryant, "LHC Machine," *Journal of Instrumentation*, vol. 3, no. 08, p. S08001, 2008.

[6] M. Conte and W. W. MacKay, *An Introduction to the Physics of Particle Accelerators.* World Scientific, 2008.

[7] O. Brüning, P. Collier, P. Lebrun, S. Myers, R. Ostojic, J. Poole, and P. Proudlock, eds., *LHC Design Report.* CERN-2004-003, Jun. 2004.

[8] A. Ballarino, A. Ijspeert, and U. Wagner, "Potential of high temperature superconductor current leads for cryogenics," in *Proceedings of the 16th International Cryogenic Engineering Conference*, (Kitakyushu Japan), pp. 1139–1142, Elsevier Science, Oxford U.K., 1996.

[9] CMS Collaboration, "The CMS experiment at the CERN LHC," *JINST*, vol. 0803, p. S08004, 2008.

[10] V. Klyukhin, N. Amapane, V. Andreev, A. Ball, B. Cure, A. Herve, A. Gaddi, H. Gerwig, V. Karimaki, R. Loveless, M. Mulders, S. Popescu, L. Sarycheva, and T. Virdee, "The cms magnetic field map performance," *Applied Superconductivity, IEEE Transactions on*, vol. 20, pp. 152 –155, june 2010.

[11] S. Das, "Status and performance of the compact muon solenoid pixel detector," *Nuclear Instruments and Methods in Physics Research Section A: Accelerators, Spectrometers, Detectors and Associated Equipment*, vol. 623, no. 1, pp. 147 – 149, 2010. 1st International Conference on Technology and Instrumentation in Particle Physics.

[12] F. Hartmann, *Evolution of Silicon Sensor Technology in Particle Physics.* Springer, 2009.

[13] M. Dinardo, "Tracking and vertexing capabilities of the cms tracking detector with the first lhc data," *Nuclear Instruments and Methods in Physics Research Section A: Accelerators, Spectrometers, Detectors and Associated Equipment*, vol. In Press, Corrected Proof, pp. –, 2010.

[14] M. Ryan, "The cms electromagnetic calorimeter at the lhc," *Nuclear Instruments and Methods in Physics Research Section A: Accelerators, Spectrometers, Detectors and Associated Equipment*, vol. 598, no. 1, pp. 217 – 219, 2009. Instrumentation for Collding Beam Physics - Proceedings of the 10th International Conference on Instrumentation for Colliding Beam Physics.

[15] G. Franzoni, "Performance of cms ecal with first lhc data," *Nuclear Instruments and Methods in Physics Research Section A: Accelerators, Spectrometers, Detectors and Associated Equipment*, vol. 628, no. 1, pp. 90 – 94, 2011. VCI 2010 - Proceedings of the 12th International Vienna Conference on Instrumentation.

[16] M. Felcini, "The trigger system of the cms experiment," *Nuclear Instruments and Methods in Physics Research Section A: Accelerators, Spectrometers, Detectors and Associated Equipment*, vol. 598, no. 1, pp. 312 – 316, 2009. Instrumentation for Collding Beam Physics - Proceedings of the 10th International Conference on Instrumentation for Colliding Beam Physics.

[17] A. Dierlamm, G. H. Dirkes, M. Fahrer, M. Frey, F. Hartmann, L. Masetti, O. Militaru, S. Shah, R. Stringer, and A. Tsirou, "The CMS Tracker Control System," *J.Phys.Conf.Ser.*, vol. 119, p. 022019, 2008.

[18] S. Shah, A. Tsirou, P. G. Verdini, F. Hartmann, L. Masetti, G. H. Dirkes, R. Stringer, and M. Fahrer, "The CMS Tracker Detector Control System," *Nucl. Instrum. Meth.*, vol. A604, pp. 281–283, 2009.

[19] ETM, "PVSS Online Help," 2011.

[20] G. Altarelli, "Status of the Standard Model and Beyond," *Nuclear Instruments and Methods in Physics Research Section A: Accelerators, Spectrometers, Detectors and Associated Equipment*, vol. 518, no. 1-2, pp. 1 – 8, 2004. Frontier Detectors for Frontier Physics: Proceedin.

[21] S. P. Martin, "A Supersymmetry Primer," 1997.

[22] V. Barger, J. Jiang, P. Langacker, and T. Li, "Gauge coupling unification in the standard model," *Physics Letters B*, vol. 624, no. 3-4, pp. 233 – 238, 2005.

[23] S. Ferrara, L. Girardello, and F. Palumbo, "General mass formula in broken supersymmetry," *Phys. Rev. D*, vol. 20, pp. 403–408, Jul 1979.

[24] S. Y. Choi *et al.*, "Reconstructing the chargino system at e+ e- linear colliders," *Eur. Phys. J.*, vol. C14, pp. 535–546, 2000.

[25] M. Guchait, "Exact solution of the neutralino mass matrix," *Zeitschrift fr Physik C Particles and Fields*, vol. 57, pp. 157–163, 1993. 10.1007/BF01555748.

[26] H. Baer and X. Tata, *Weak Scale Supersymmetry: From Superfields to Scattering Events.* Cambridge University Press, 2006.

[27] D. Hooper and S. Profumo, "Dark matter and collider phenomenology of universal extra dimensions," *Phys. Rept.*, vol. 453, pp. 29–115, 2007.

[28] H.-C. Cheng, K. T. Matchev, and M. Schmaltz, "Radiative corrections to kaluza-klein masses," *Phys. Rev. D*, vol. 66, p. 036005, Aug 2002.

[29] CMS Collaboration, *CMS Physics Technical Design Report Volume I: Detector Performance and Software.* Technical Design Report CMS, Geneva: CERN, 2006.

[30] "CMS Photon ID Twiki," 2011.

[31] CMS Collaboration, "Measurement of the isolated prompt photon production cross section in pp collisions at $\sqrt{s} = 7$ tev," *Phys. Rev. Lett.*, vol. 106, p. 082001, Feb 2011.

[32] CMS Collaboration, "Jet performance in pp collisions at 7 tev," *CMS Physics Analysis Summary*, vol. JME-10-003, 2010.

[33] M. Cacciari, G. P. Salam, and G. Soyez, "The anti-k_t jet clustering algorithm," *JHEP*, vol. 04, p. 063, 2008.

[34] CMS Collaboration, "Plans for Jet Energy Corrections at CMS," *CMS Physics Analysis Summary*, vol. JME-07-002, 2008.

[35] Y. Gershtein, M. Park, J. Ruderman, D. Shih, S. Thomas, and Y. Zhao, "General neutralino parameter spaces," May 2011.

[36] M. ElKacimi, D. Goujdami, H. Przysiezniak, and P. Skands, "One universal extra dimension in pythia," *Computer Physics Communications*, vol. 181, no. 1, pp. 122 – 127, 2010.

[37] ATLAS Collaboration, "Search for Diphoton Events with Large Missing Transverse Energy in 7 TeV Proton-Proton Collisions with the ATLAS Detector," *Phys. Rev. Lett.*, Dec. 2010.

[38] Y. Yang, S. J. S, M. Soares, and D. Nguyen, "Exotica photon fake rate studies," May 2011.

[39] M. Botje, J. Butterworth, A. Cooper-Sarkar, A. de Roeck, J. Feltesse, S. Forte, A. Glazov, J. Huston, R. McNulty, T. Sjostrand, and R. Thorne, "The PDF4LHC Working Group Interim Recommendations,"

[40] W. Beenakker, R. Hopker, and M. Spira, "PROSPINO: A program for the PROduction of Supersymmetric Particles In Next-to-leading Order QCD," 1996.

[41] Particle Data Group Collaboration, "The bayesian approach," *Phys. Lett.*, vol. B667,Section 32.3.1, p. 1, 2008.

[42] CMS Collaboration, "Search for supersymmetry in pp collisions at sqrt(s)=7 tev in events with two photons and missing transverse energy," *Phys. Rev. Lett.*, vol. 106, p. 211802, May 2011.

[43] D0 Collaboration, "Search for diphoton events with large missing transverse energy in 6.3 fb^{-1} of $\mathbf{p\bar{p}}$ collisions at $\sqrt{\mathbf{s}} = \mathbf{1.96}$ TeV," *Phys. Rev. Lett.*, vol. 105, p. 221802, 2010.

[44] T. Appelquist, H.-C. Cheng, and B. A. Dobrescu, “Bounds on universal extra dimensions,” *Phys. Rev. D*, vol. 64, p. 035002, Jun 2001.

[45] A. Dominguez, “The cms pixel detector,” *Nuclear Instruments and Methods in Physics Research Section A: Accelerators, Spectrometers, Detectors and Associated Equipment*, vol. 581, no. 1-2, pp. 343 – 346, 2007. VCI 2007 - Proceedings of the 11th International Vienna Conference on Instrumentation.

[46] B. Kreis, “The online calibration, operation, and performance of the cms pixel detector,” *Nuclear Instruments and Methods in Physics Research Section A: Accelerators, Spectrometers, Detectors and Associated Equipment*, vol. In Press, Corrected Proof, pp. –, 2010.

[47] H. E. Haber and G. L. Kane, “The search for supersymmetry: Probing physics beyond the standard model,” *Physics Reports*, vol. 117, no. 2-4, pp. 75 – 263, 1985.

Appendix A

Software

A.1 Data processing

This analysis was performed using CMS Software (CMSSW) version 3_8_3. CMSSW is object-oriented analysis software designed specifically for the CMS detector. CMSSW interfaces with several other physics packages to perform different tasks. There are four processes defined in the data analysis chain for CMSSW: GEN, SIM, DIGI, and RECO. The first three steps are needed only for simulated data while the RECO process is need for both simulated and real data.

A.1.1 MC Generation

The GEN or generator step allows for the creation of simulated physics events using Monte Carlo randomization. CMSSW has several "producers" which provide simple events. One example of this is the "Particle Gun" in which particles of a chosen type are created with a chosen distribution of energy and direction. More complex generation is possible using a MC generator such as PYTHIA. PYTHIA can generate complex production processes and cascade decays including hadronization and radiative processes. PYTHIA can generate all standard model processes and supports many BSM models including the ones used in this analysis, Gauge Mediated SUSY and Universal Extra Dimensions. PYTHIA can also use an externally generated file containing particle spectrums, cross sections and branching ratios known as a SUSY Les Houches Accord (SLHA) file. PYTHIA would then create events using the SLHA information and then apply its own hadronization process. Additional generators, such as MadGraph, can be used with CMSSW. If the generator does not directly interface with CMSSW then the generator level events can be passed to CMSSW using a standard format known as the Les Houches Event (LHE) format.

A.1.2 Detector Simulation

The SIM step in the reconstruction chain simulates the effects of material as the particles pass through the different layers of the CMS detector. This is performed using GEANT4. Due to the complexity of the full simulation process the SIM step can take a long time. In some cases it could be a number of seconds per event. This would make the generation of large numbers of event very difficult. To solve this problem a simplified method of detector simulation know as FASTSIM, was developed. The FASTSIM software makes a number of simplifying assumptions and includes optimization for speed. The results were tuned to the GEANT4 full simulation to assure accurate simulation. More detail can be found in [29].

A.1.3 Digitization

The digitization (DIGI) step simulates the detector response to generated particles. Each subdetector group created its own digitizer to provide an accurate simulation. Each digitizer included simulated errors due to resolution limitations and misalignment.

Again, as this is a simulation process it is not used with collected data, but rather with MC generated events.

A.1.4 Reconstruction

The reconstruction (RECO) process takes the low-level detector information, simulated or collected, and constructs high-level objects (tracks, superclusters, calotowers) and physics quantities such as E_T^{miss}. In some cases different algorithms are used to create several versions of physics objects allowing the use some freedom in the choice of definitions.

A.1.5 AOD

The full reconstructed event can become very large, containing multiple definitions of physics objects information from intermediate processing steps. To reduce the size per event a smaller format called Analysis Object Data (AOD). The AOD format only contains the highest level objects with none of the intermediate information. The AOD format can reduce event size by over a factor 10.

A.2 Custom Object Selectors

The CMSSW event data model (EDM) creates “collections” of physics objects that can be used in the analysis. It is possible to define custom collections that may be added to the event post-reconstruction. The collections can contain new objects, composite objects, or objects present in other collections. It is also possible, if no new information is added to the event, but rather the new collection only contains a subset of existing information, the collection may contain only references. A reference is a pointer to an existing object rather than a copy of that object. As the size of each event stored on disk can exceed 1 MB, it is useful to use references whenever possible to reduce the event size.

A.2.1 GMSB Object Selectors

In order to facilitate the analysis of the EM objects defined, custom collections of Photons, Electrons, and Fakes were created. These collections, called for historical reasons, GMSBPhotons, GMSBElectrons, and GMSBFakes, contain references to objects in the photon collection. These collections provide a filtered subset of photons, classified by EM object type and passing the photon identification cuts.

Appendix B

Additional plots

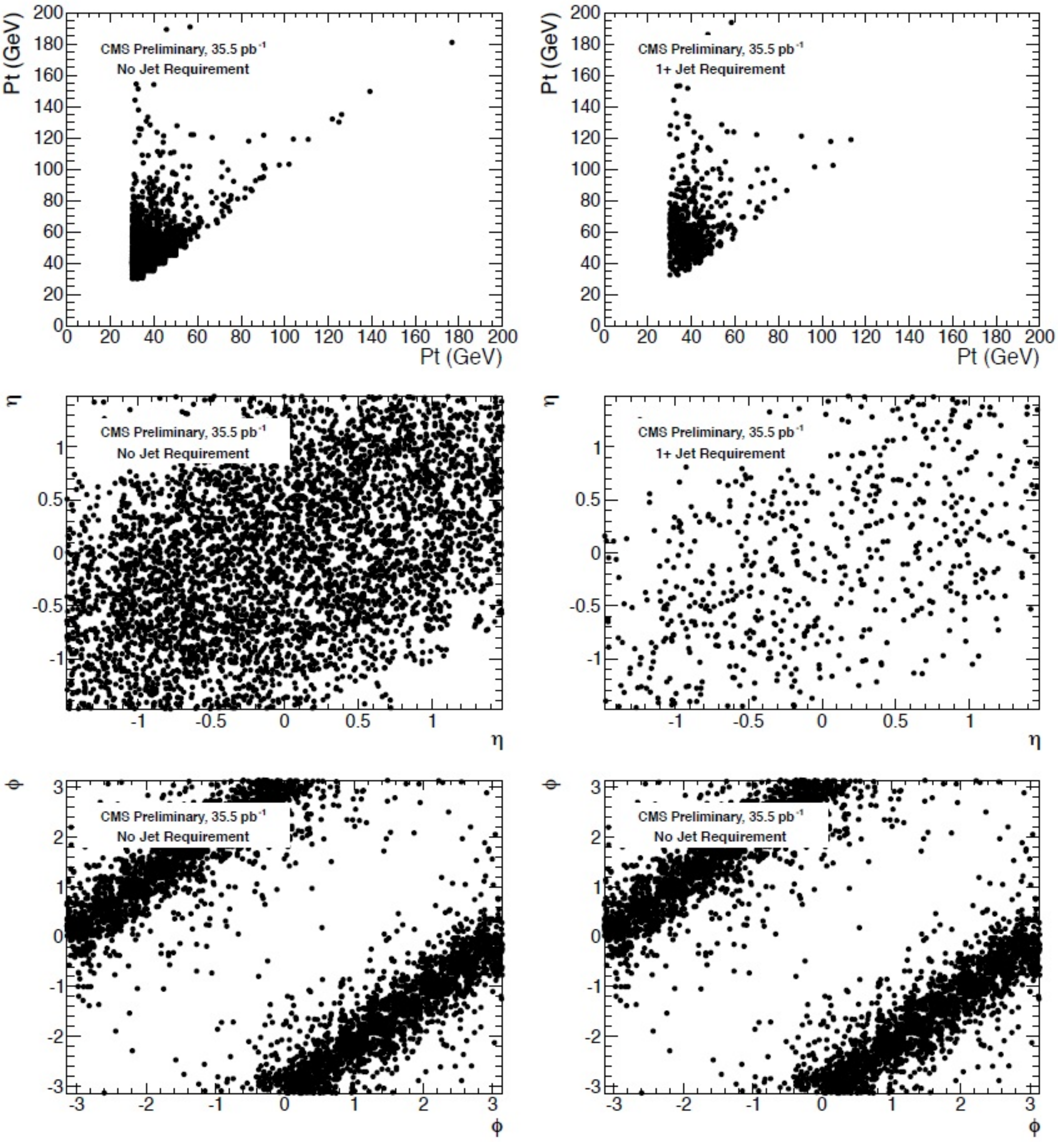

Figure B.1: Leading electron vs. trailing electron for E_T, η, and ϕ. Left plots: no jet required. Right plots: ≥1 jet required.

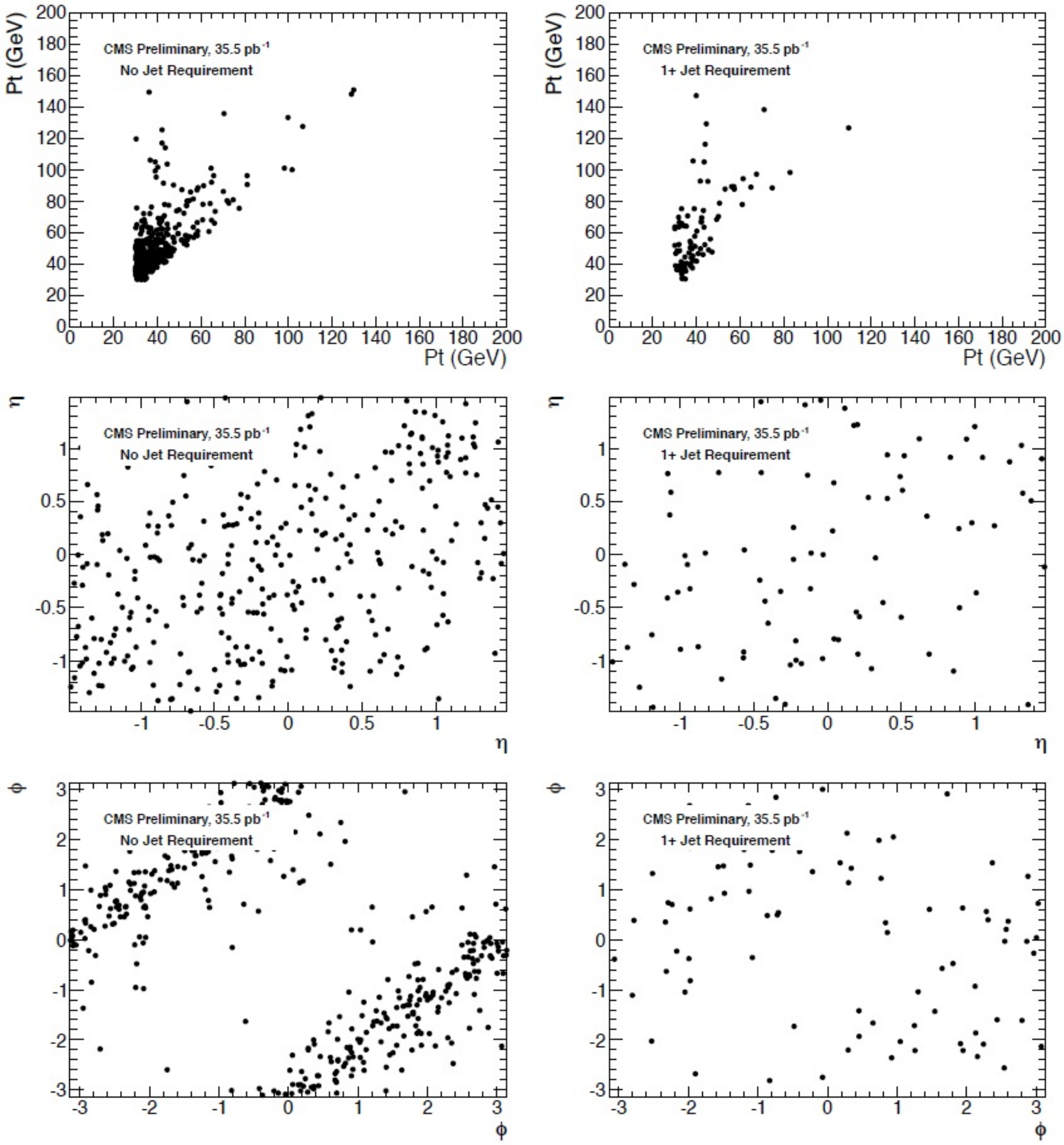

Figure B.2: Leading photon vs. trailing photon for E_T, η, and ϕ. Left plots: no jet required. Right plots: ≥1 jet required.

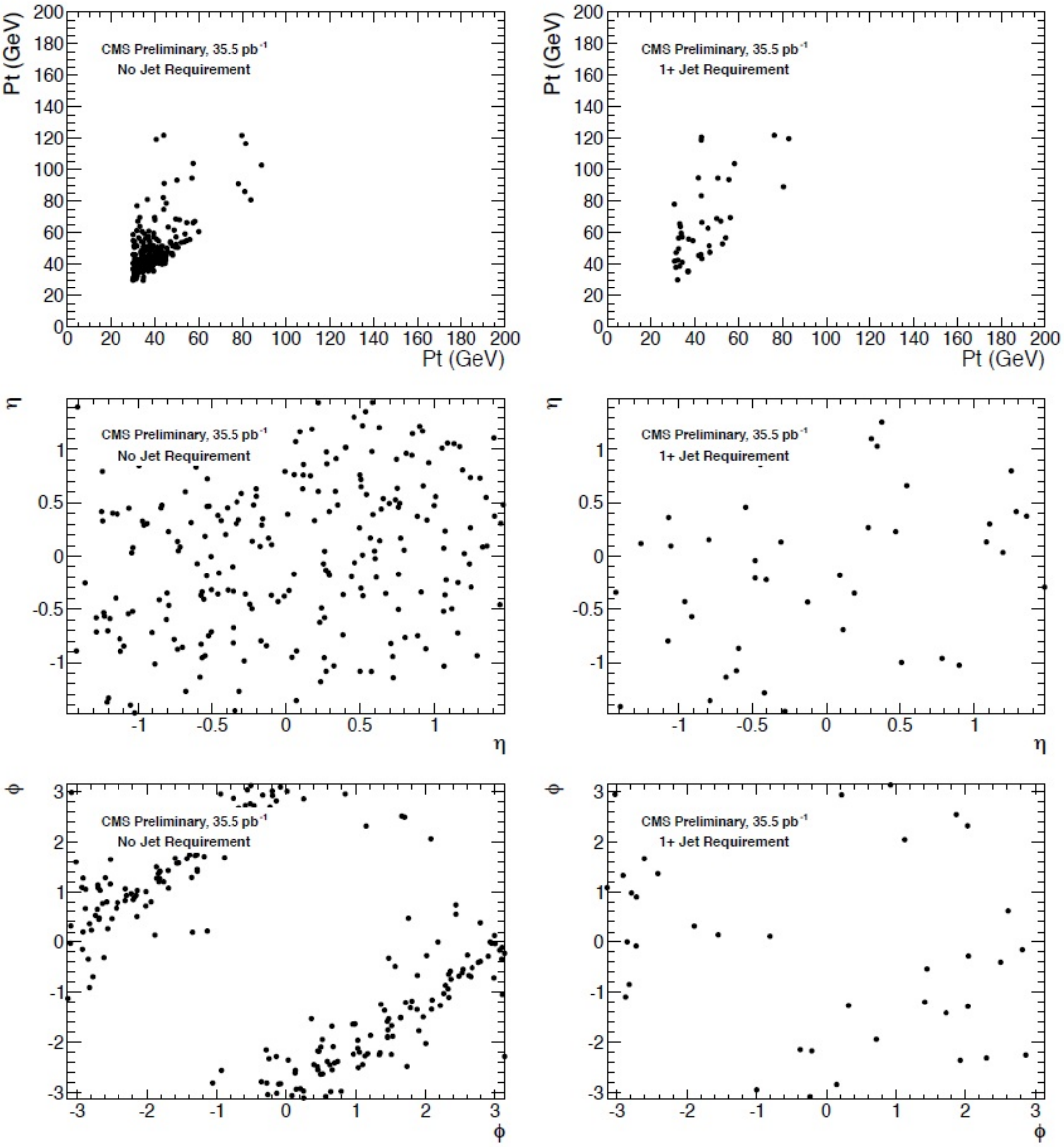

Figure B.3: Leading electron/photon vs. trailing electron/photon in $e\gamma$ events for E_T, η, and ϕ. Left plots: no jet required. Right plots: $\geq$1 jet required.

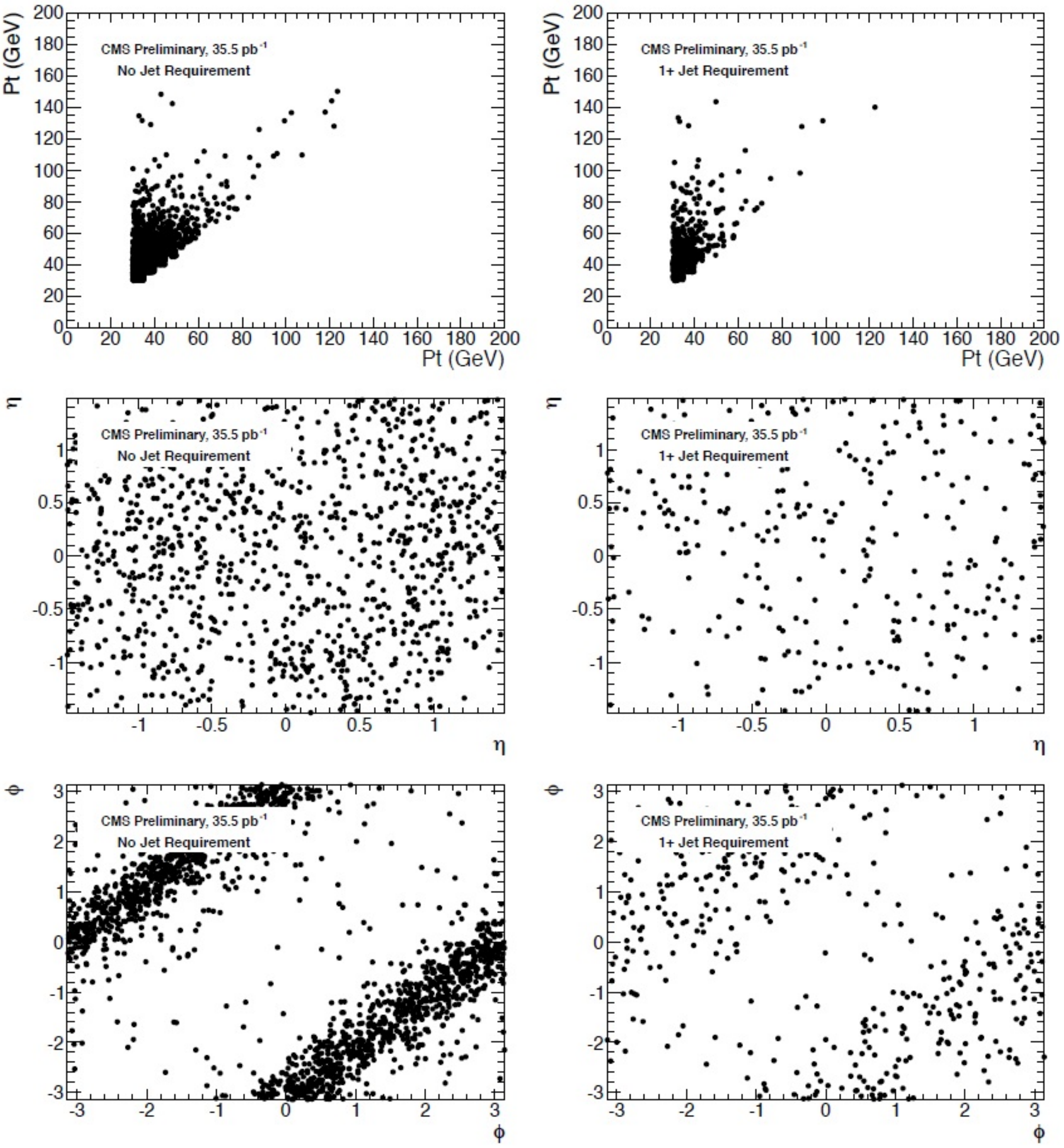

Figure B.4: Leading fake photon vs. trailing fake photon for E_T, η, and ϕ. Left plots: no jet required. Right plots: ≥1 jet required.

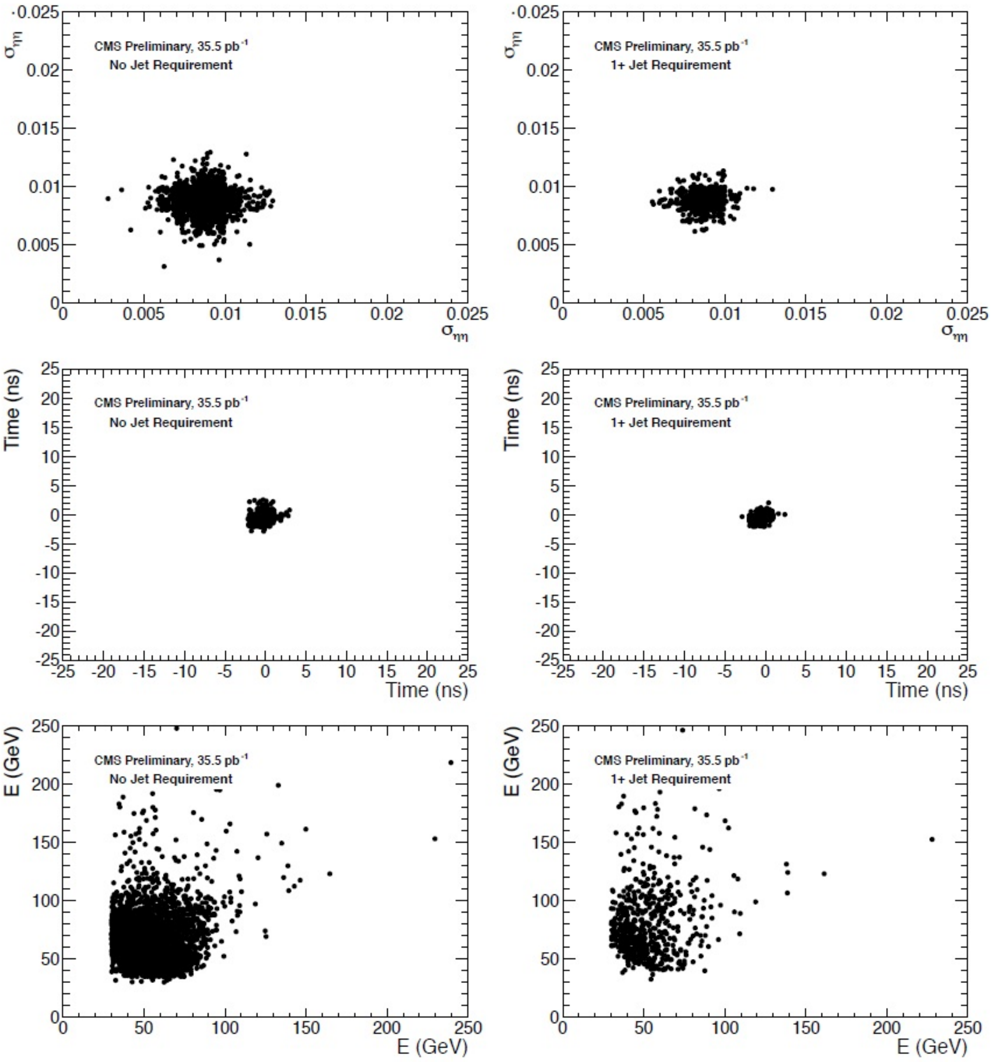

Figure B.5: Leading electron vs. trailing electron in *ee* events for $\sigma_{\eta\eta}$,Time, and Energy. Left plots: no jet required. Right plots: ≥1 jet required.

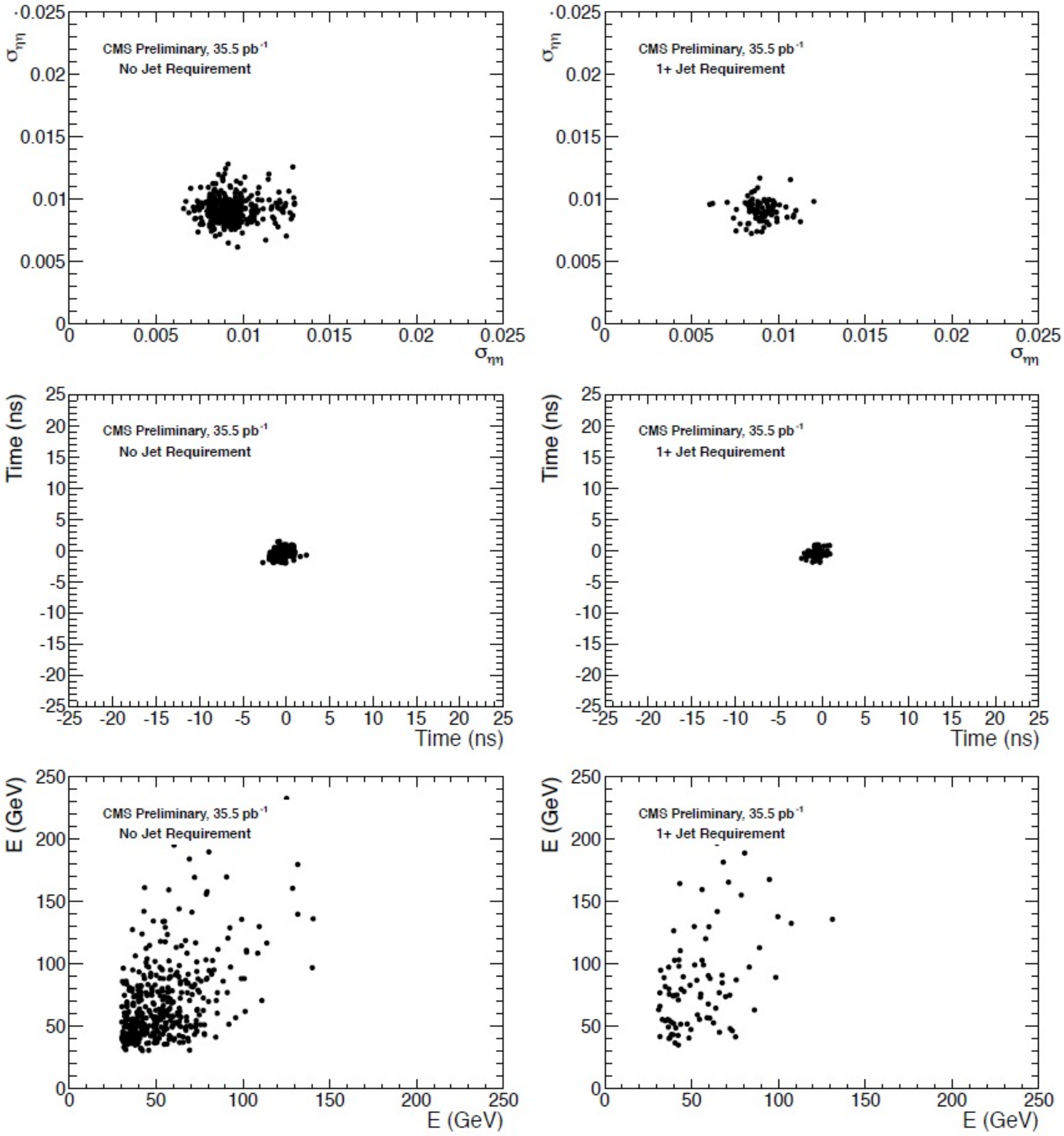

Figure B.6: Leading photon vs. trailing photon in $\gamma\gamma$ events for $\sigma_{\eta\eta}$,Time, and Energy. Left plots: no jet required. Right plots: ≥1 jet required.

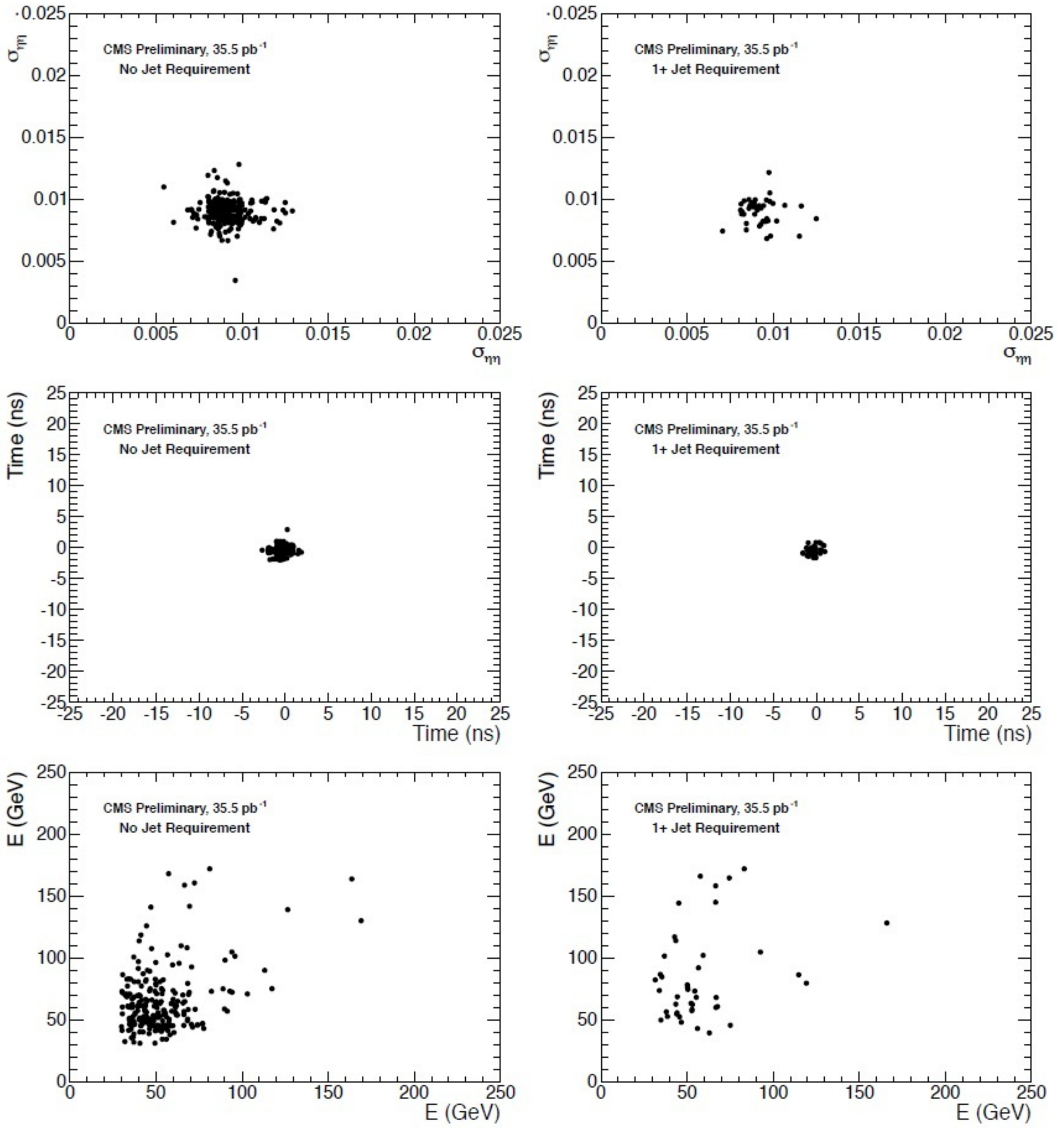

Figure B.7: Leading electron/photon vs. trailing electron/photon in $e\gamma$ events for $\sigma_{\eta\eta}$,Time, and Energy. Left plots: no jet required. Right plots: ≥1 jet required.

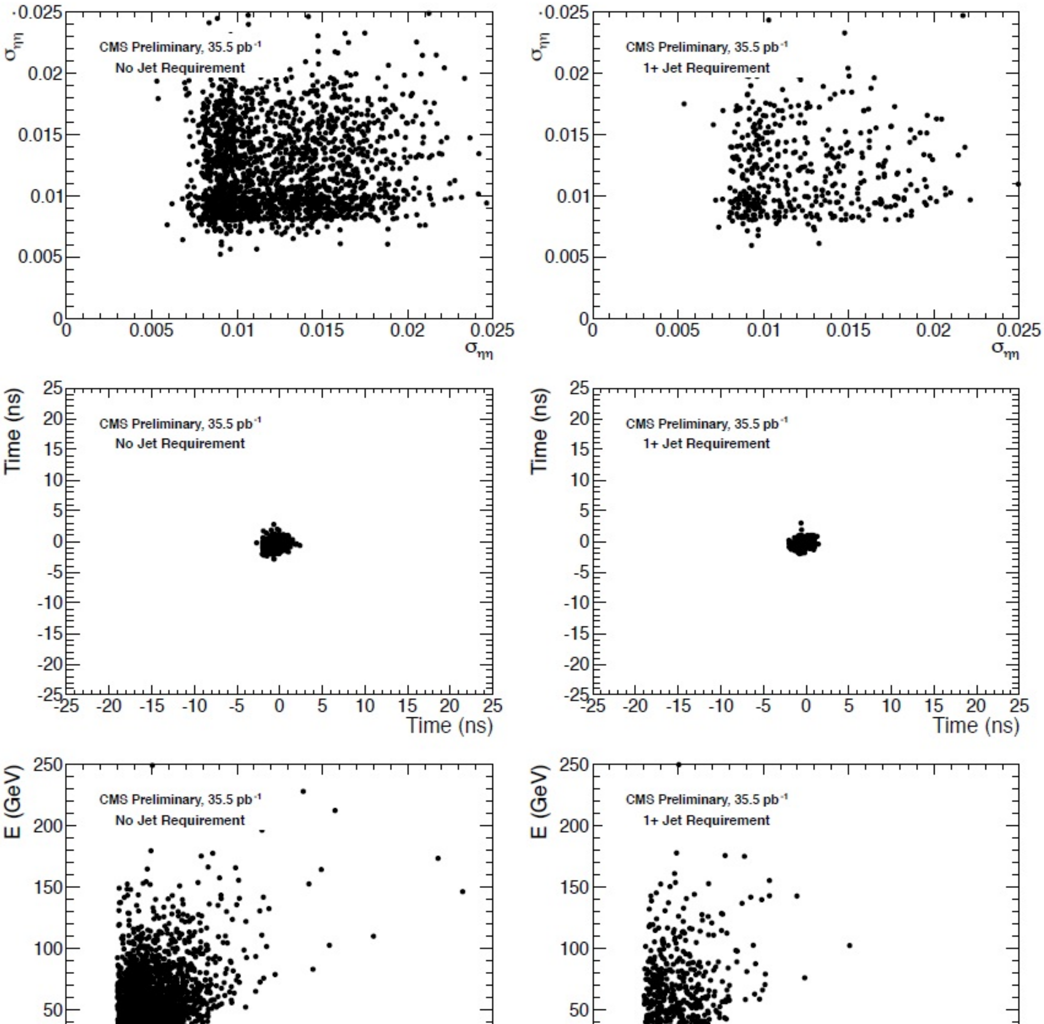

Figure B.8: Leading fake photon vs. trailing fake photon in ff events for $\sigma_{\eta\eta}$,Time, and Energy. Left plots: no jet required. Right plots: ≥1 jet required.

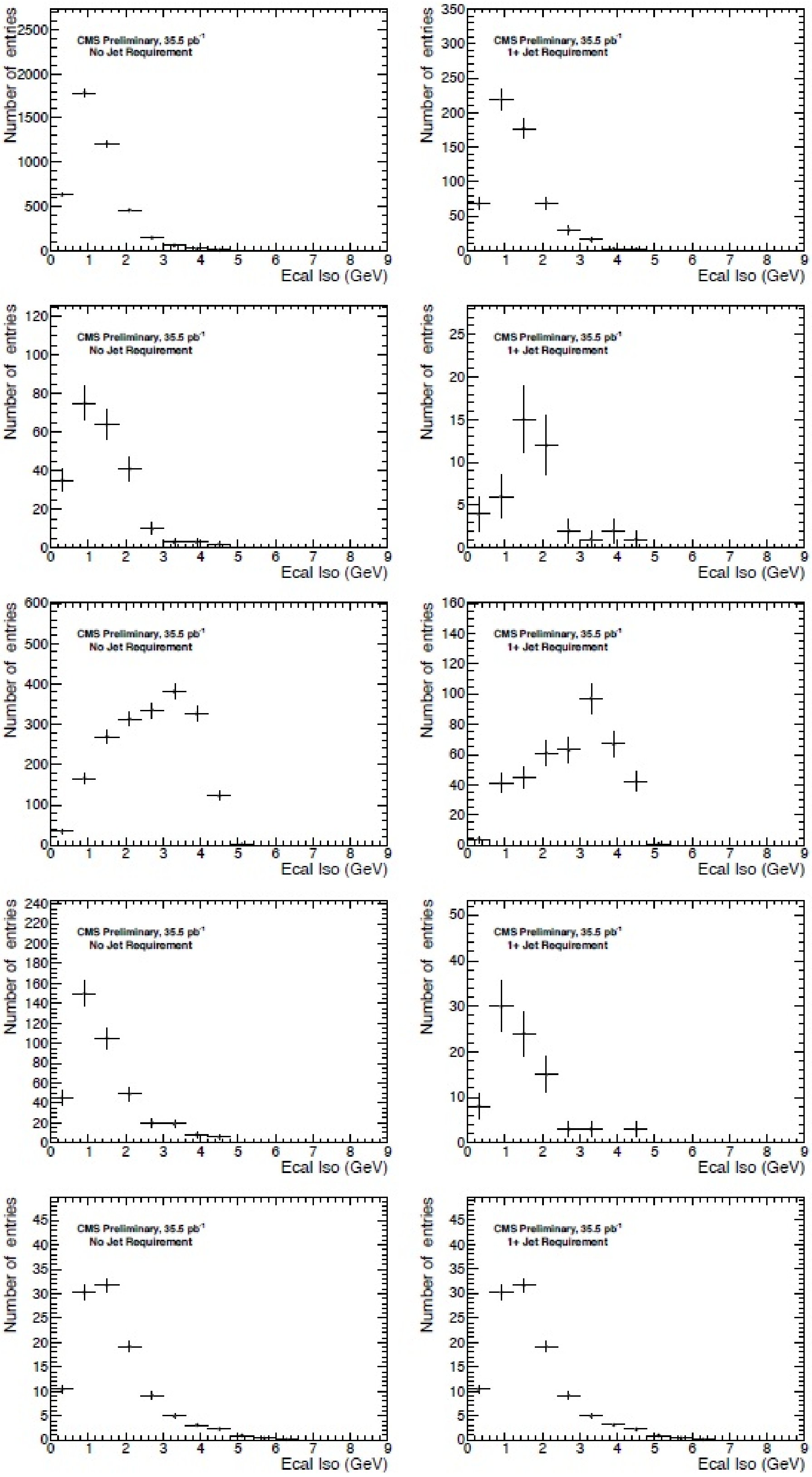

Figure B.9: ECAL Isolation distributions for lead photon/electron/fake photon. 1^{st} row: ee events. 2^{nd} row: $e\gamma$ events. 3^{rd} row: ff events. 4^{th} row: $\gamma\gamma$ events. 5^{th} row: $\gamma\gamma$ events in GGM signal MC. Left plots: no jet required. Right plots: $\geq$1 jet required.

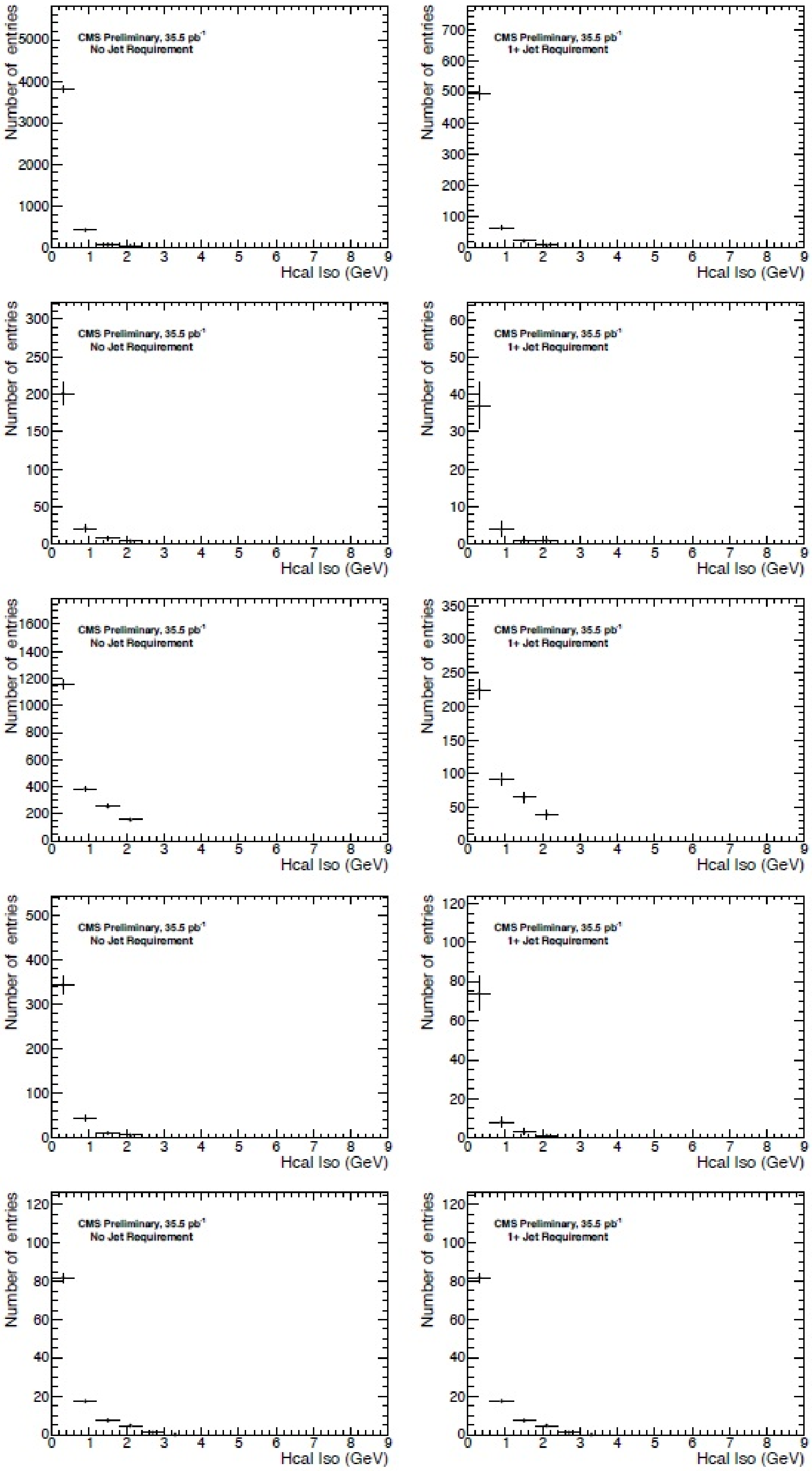

Figure B.10: HCAL Isolation distributions for lead photon/electron/fake photon. 1^{st} row: ee events. 2^{nd} row: $e\gamma$ events. 3^{rd} row: ff events. 4^{th} row: $\gamma\gamma$ events. 5^{th} row: $\gamma\gamma$ events in GGM signal MC. Left plots: no jet required. Right plots: $\geq$1 jet required.

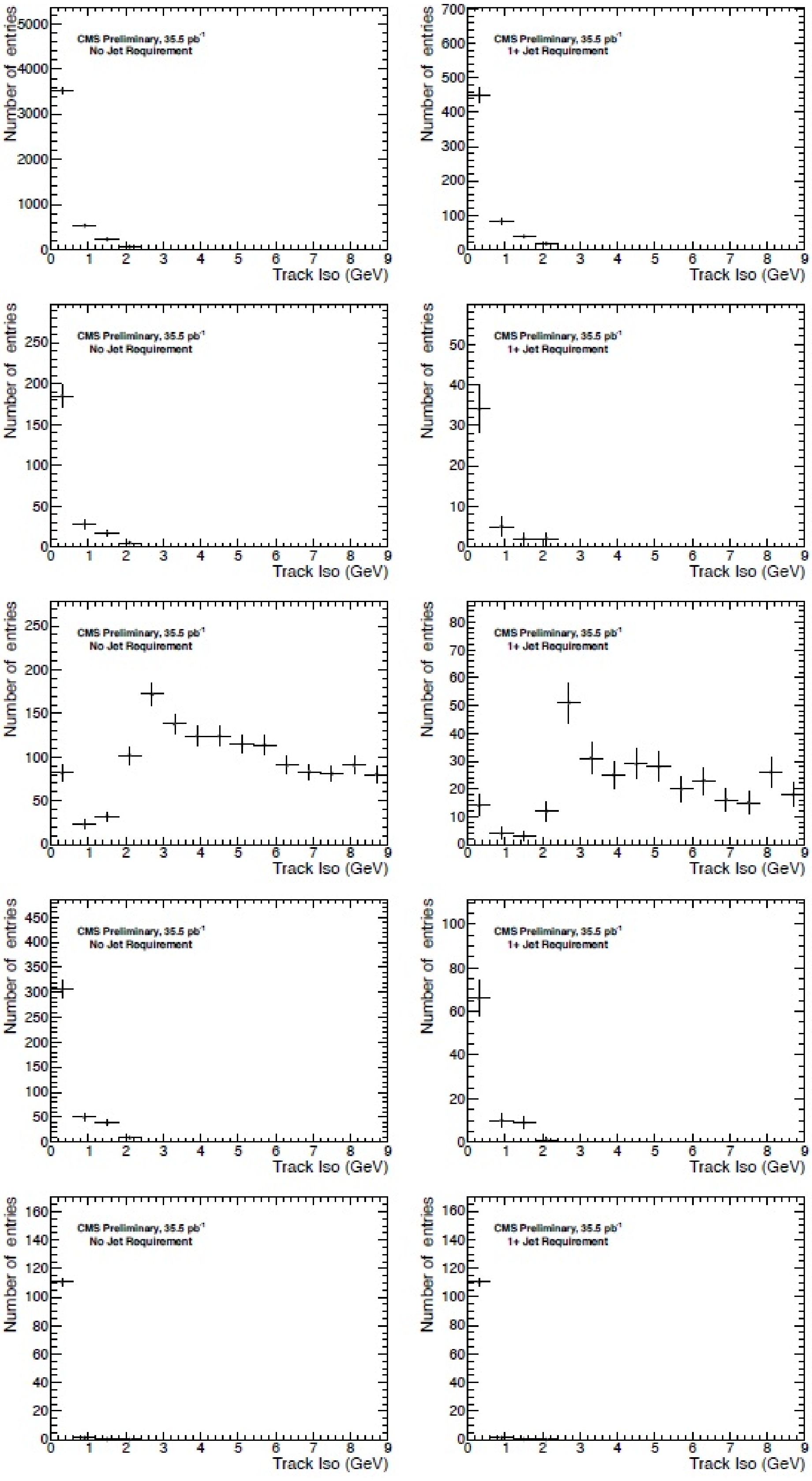

Figure B.11: Track Isolation distributions for lead photon/electron/fake photon. 1^{st} row: ee events. 2^{nd} row: $e\gamma$ events. 3^{rd} row: ff events. 4^{th} row: $\gamma\gamma$ events. 5^{th} row: $\gamma\gamma$ events in GGM signal MC. Left plots: no jet required. Right plots: $\geq$1 jet required.

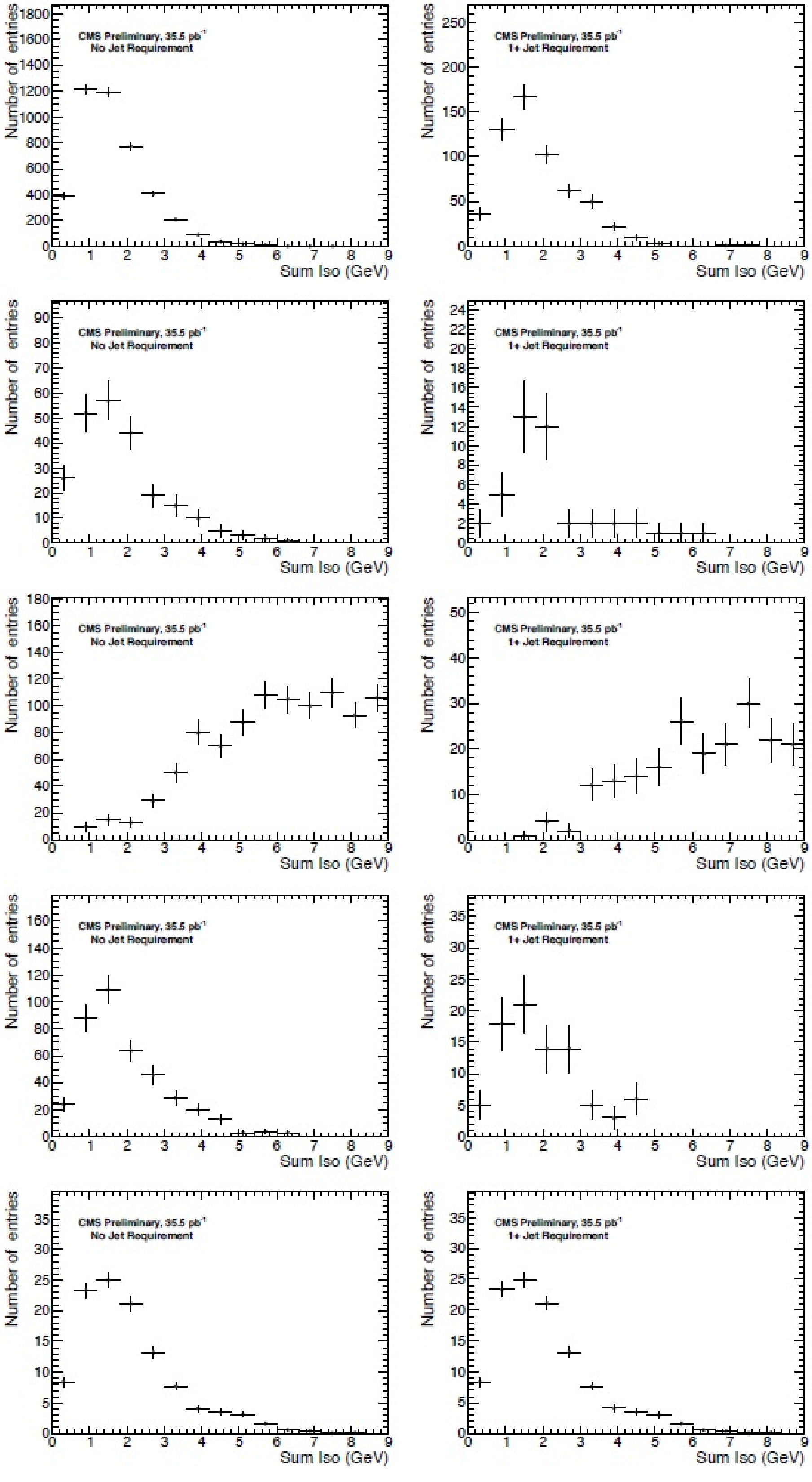

Figure B.12: Sum of ECAL, HCAL, and Track Isolations for lead photon/electron/fake photon. 1st row: ee events. 2nd row: $e\gamma$ events. 3rd row: ff events. 4th row: $\gamma\gamma$ events. 5th row: $\gamma\gamma$ events in GGM signal MC. Left plots: no jet required. Right plots: $\geq$1 jet required.

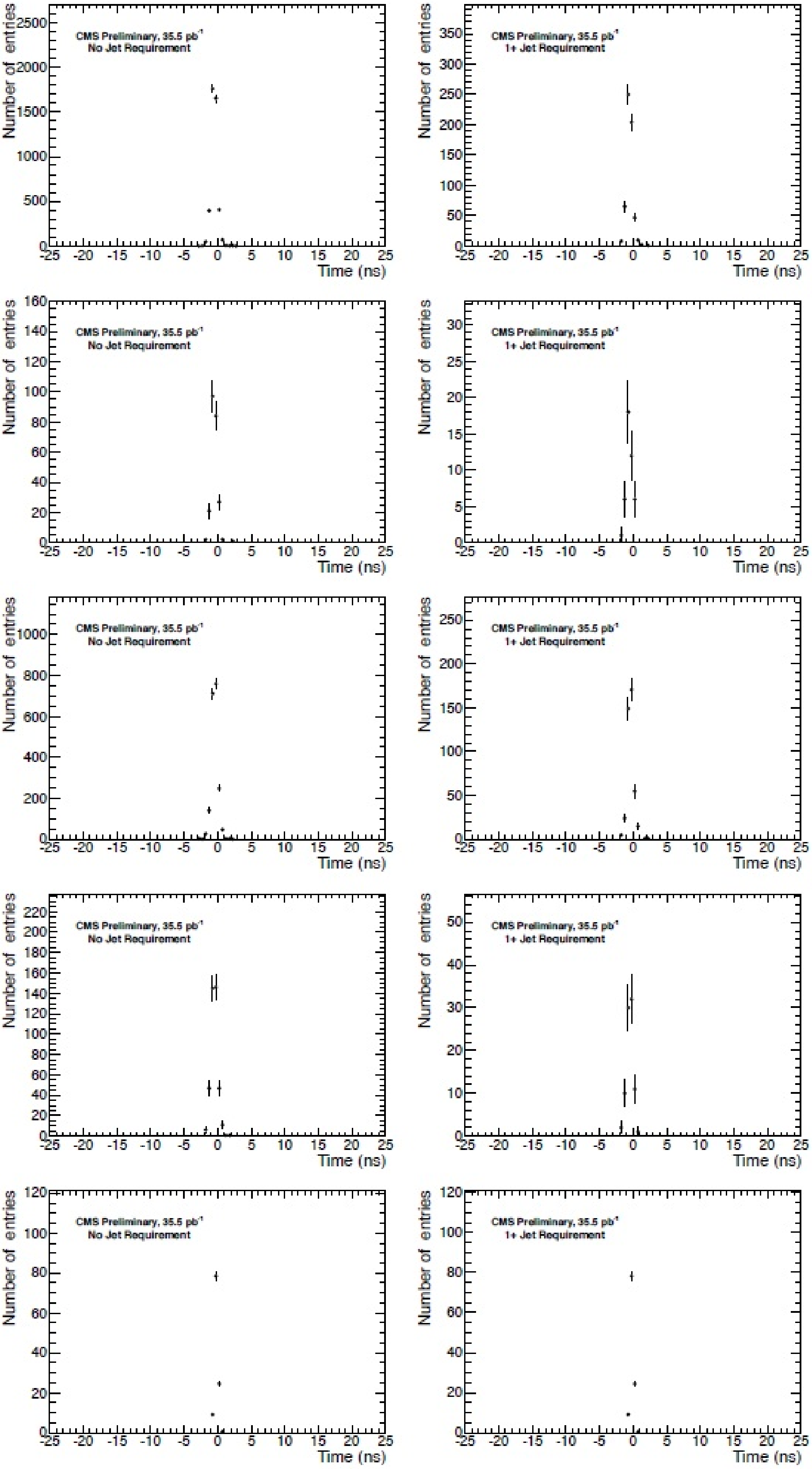

Figure B.13: Time (rechit vs. bunch crossing) distributions for lead photon/electron/fake photon. 1st row: ee events. 2nd row: $e\gamma$ events. 3rd row: ff events. 4th row: $\gamma\gamma$ events. 5th row: $\gamma\gamma$ events in GGM signal MC. Left plots: no jet required. Right plots: ≥1 jet required.

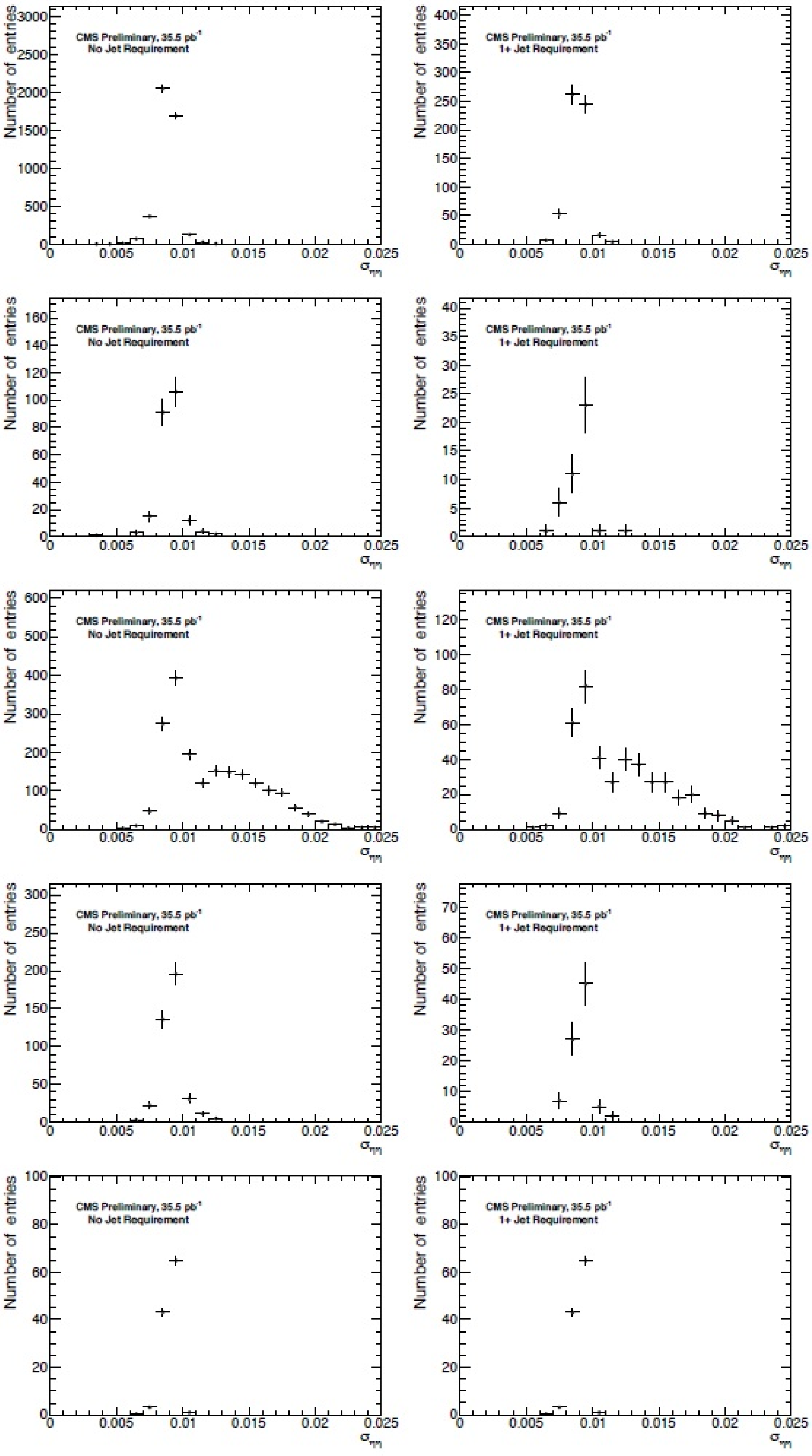

Figure B.14: Showershape ($\sigma_{i\eta i\eta}$) distributions for lead photon/electron/fake photon. 1^{st} row: ee events. 2^{nd} row: $e\gamma$ events. 3^{rd} row: ff events. 4^{th} row: $\gamma\gamma$ events. 5^{th} row: $\gamma\gamma$ events in GGM signal MC. Left plots: no jet required. Right plots: ≥1 jet required.

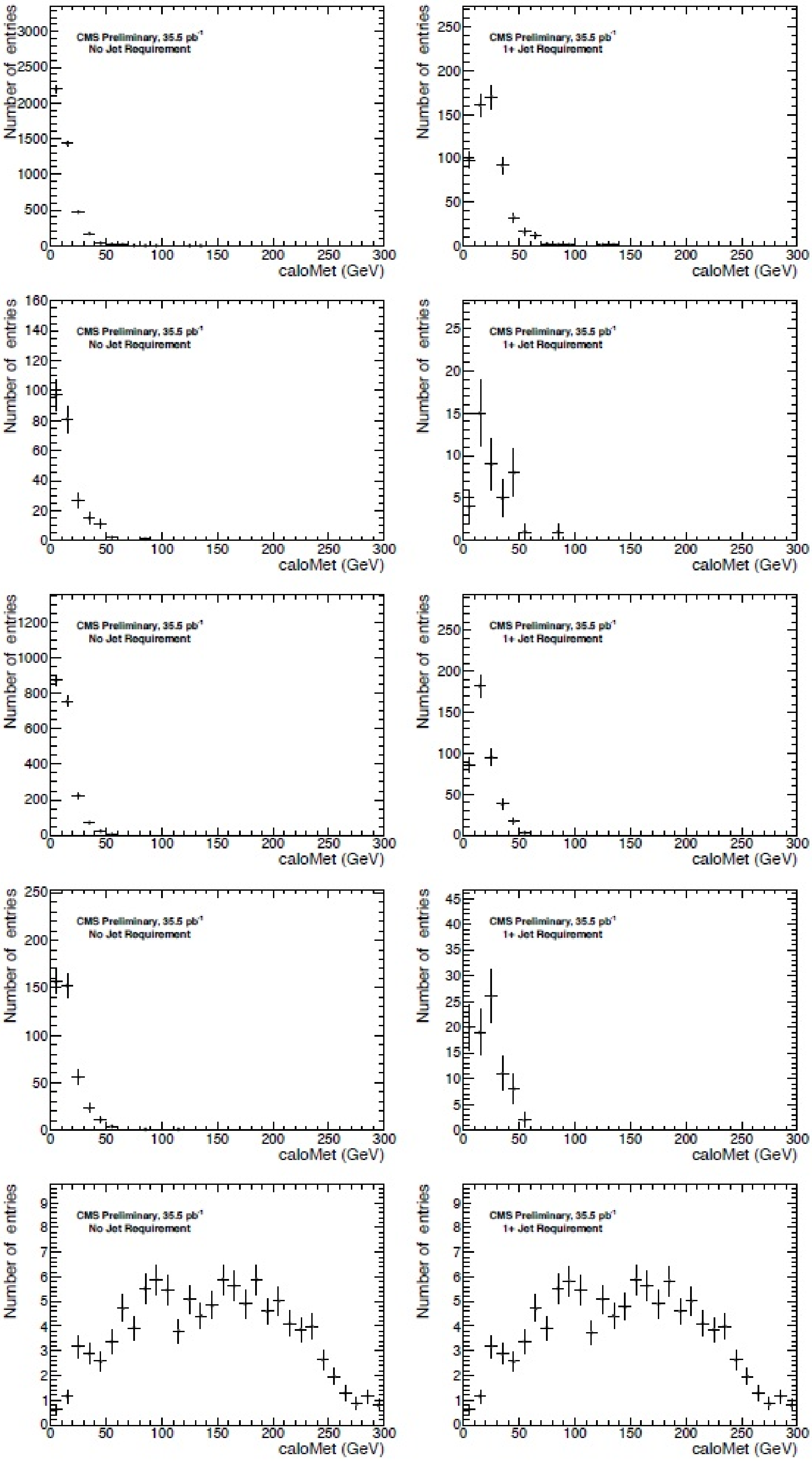

Figure B.15: CaloMET distributions for events. 1st row: ee events. 2nd row: $e\gamma$ events. 3rd row: ff events. 4th row: $\gamma\gamma$ events. 5th row: $\gamma\gamma$ events in GGM signal MC. Left plots: no jet required. Right plots: ≥1 jet required.

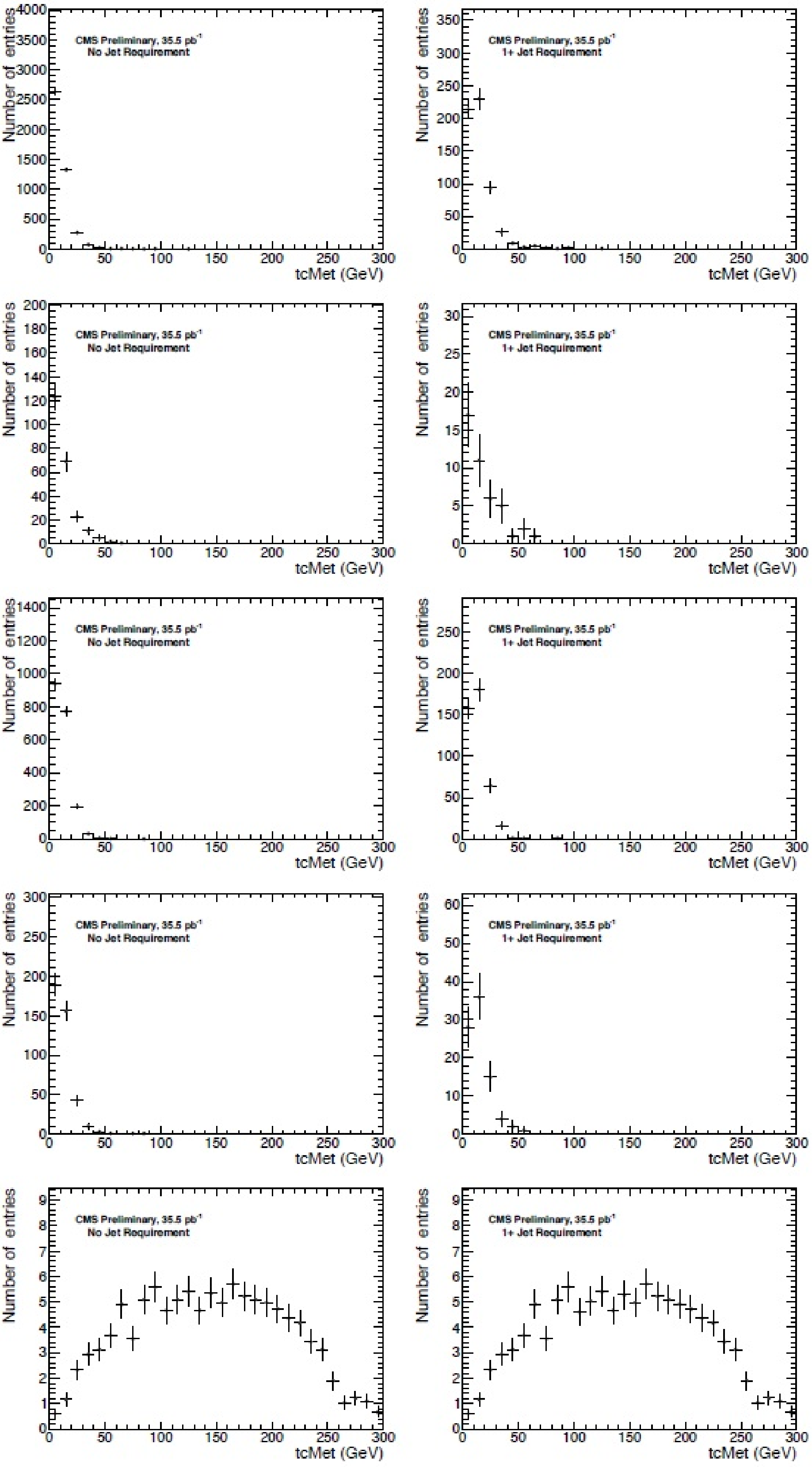

Figure B.16: tcMET distributions for events. 1^{st} row: ee events. 2^{nd} row: $e\gamma$ events. 3^{rd} row: ff events. 4^{th} row: $\gamma\gamma$ events. 5^{th} row: $\gamma\gamma$ events in GGM signal MC. Left plots: no jet required. Right plots: ≥1 jet required.

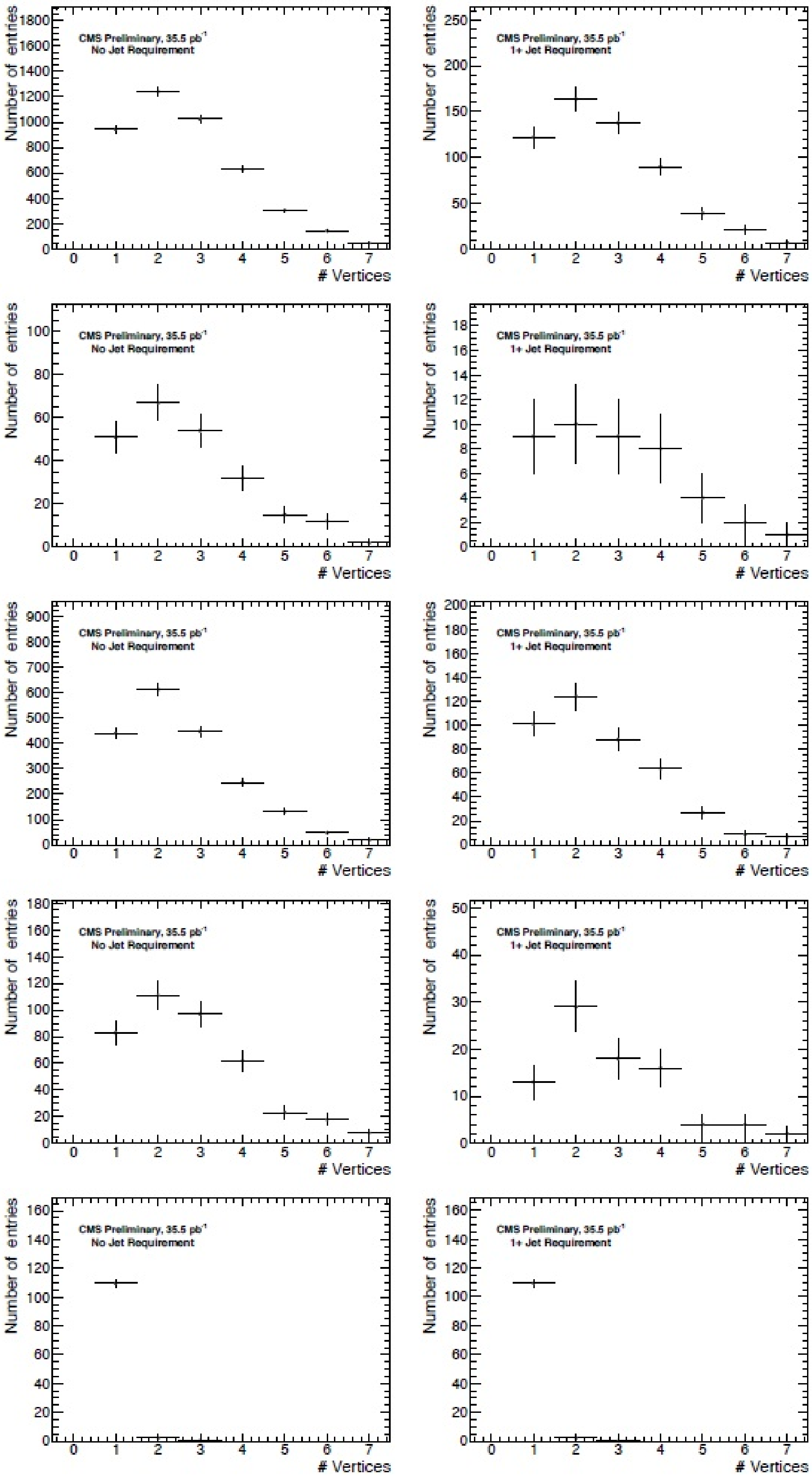

Figure B.17: Distribution of number of vertices per event. 1st row: ee events. 2nd row: $e\gamma$ events. 3rd row: ff events. 4th row: $\gamma\gamma$ events. 5th row: $\gamma\gamma$ events in GGM signal MC. Left plots: no jet required. Right plots: ≥1 jet required.

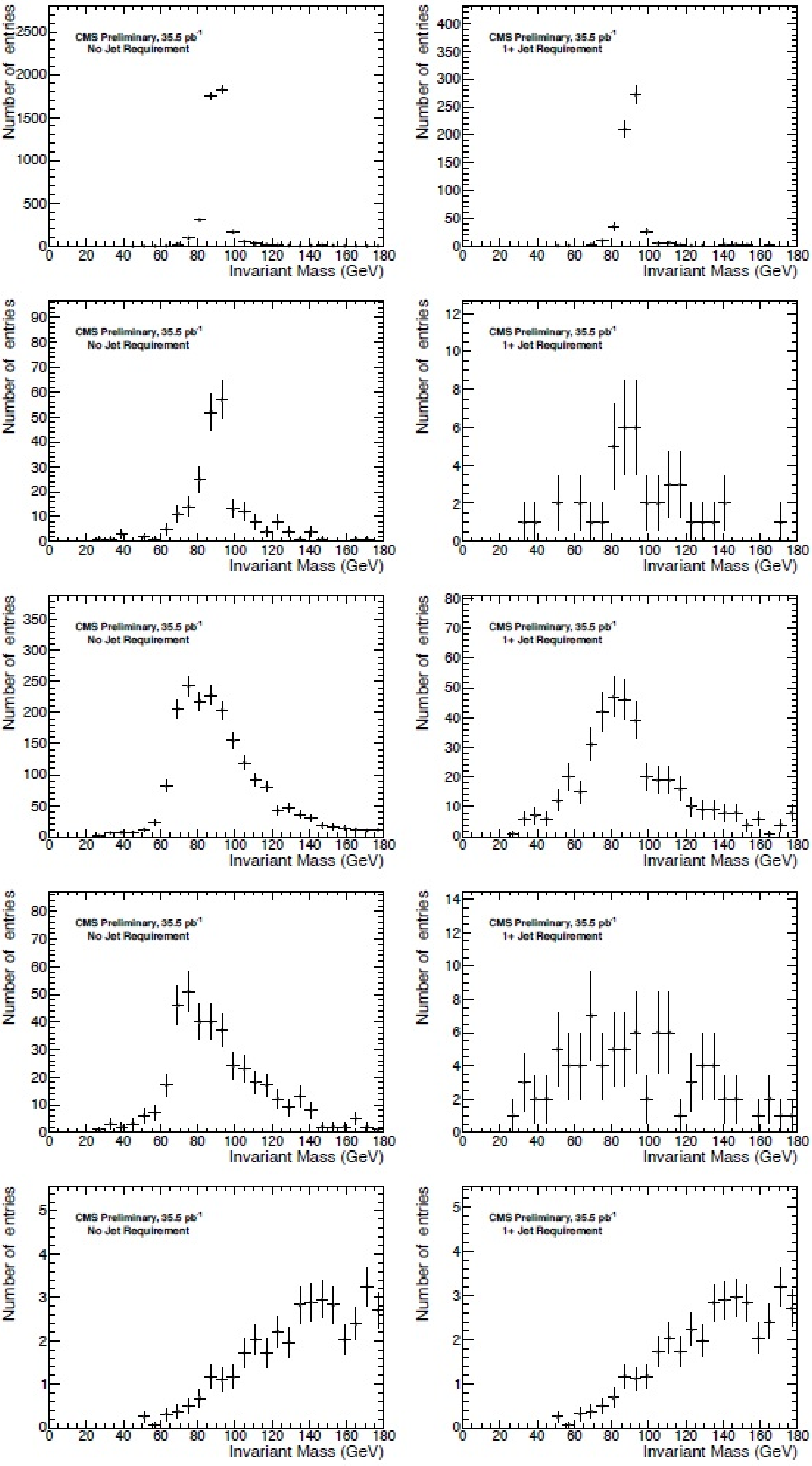

Figure B.18: Di-EM Invariant mass distributions. 1^{st} row: ee events. 2^{nd} row: $e\gamma$ events. 3^{rd} row: ff events. 4^{th} row: $\gamma\gamma$ events. 5^{th} row: $\gamma\gamma$ events in GGM signal MC. Left plots: no jet required. Right plots: ≥1 jet required.

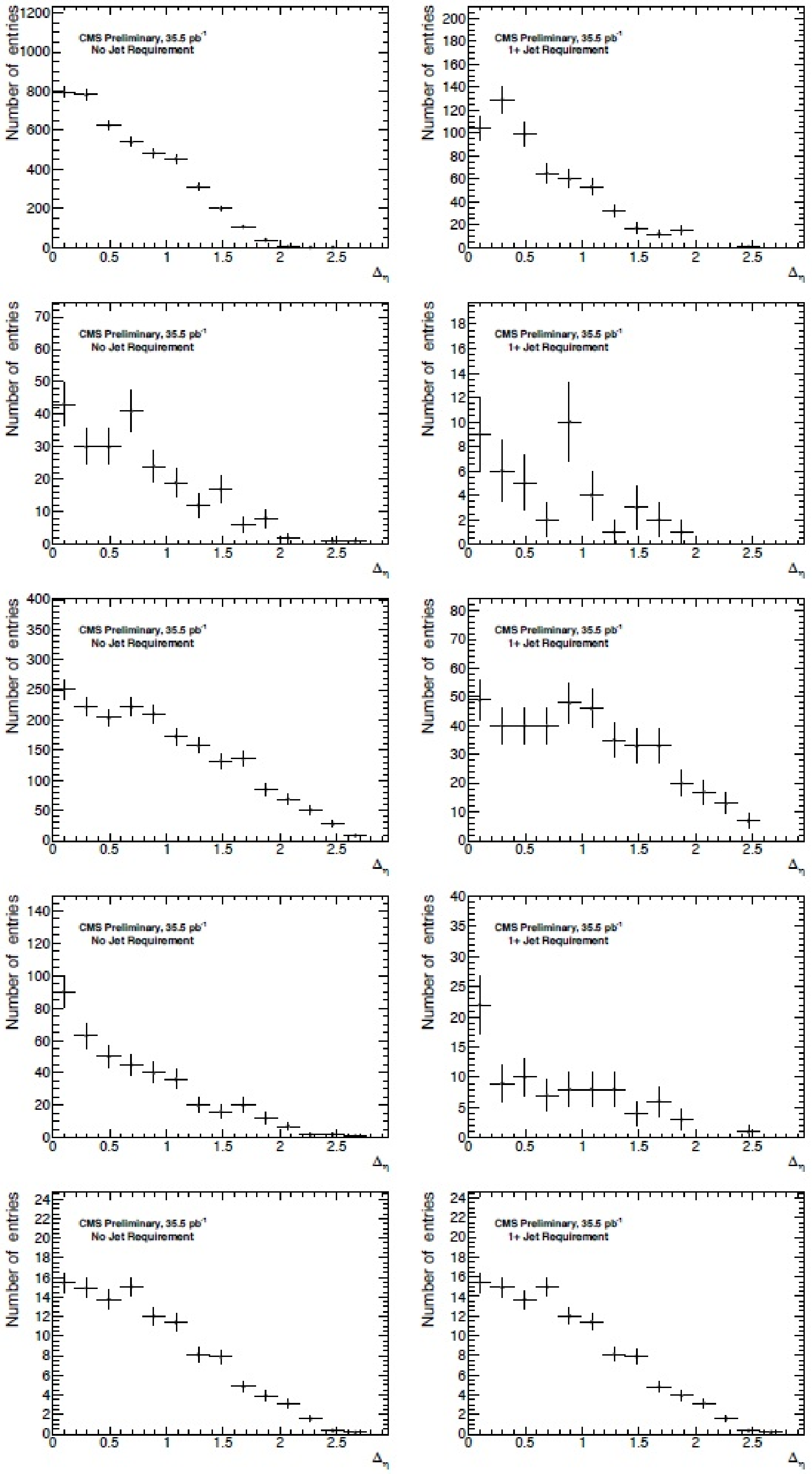

Figure B.19: $\Delta\eta$ distributions between lead and trail objects. 1st row: ee events. 2nd row: $e\gamma$ events. 3rd row: ff events. 4th row: $\gamma\gamma$ events. 5th row: $\gamma\gamma$ events in GGM signal MC. Left plots: no jet required. Right plots: ≥1 jet required.

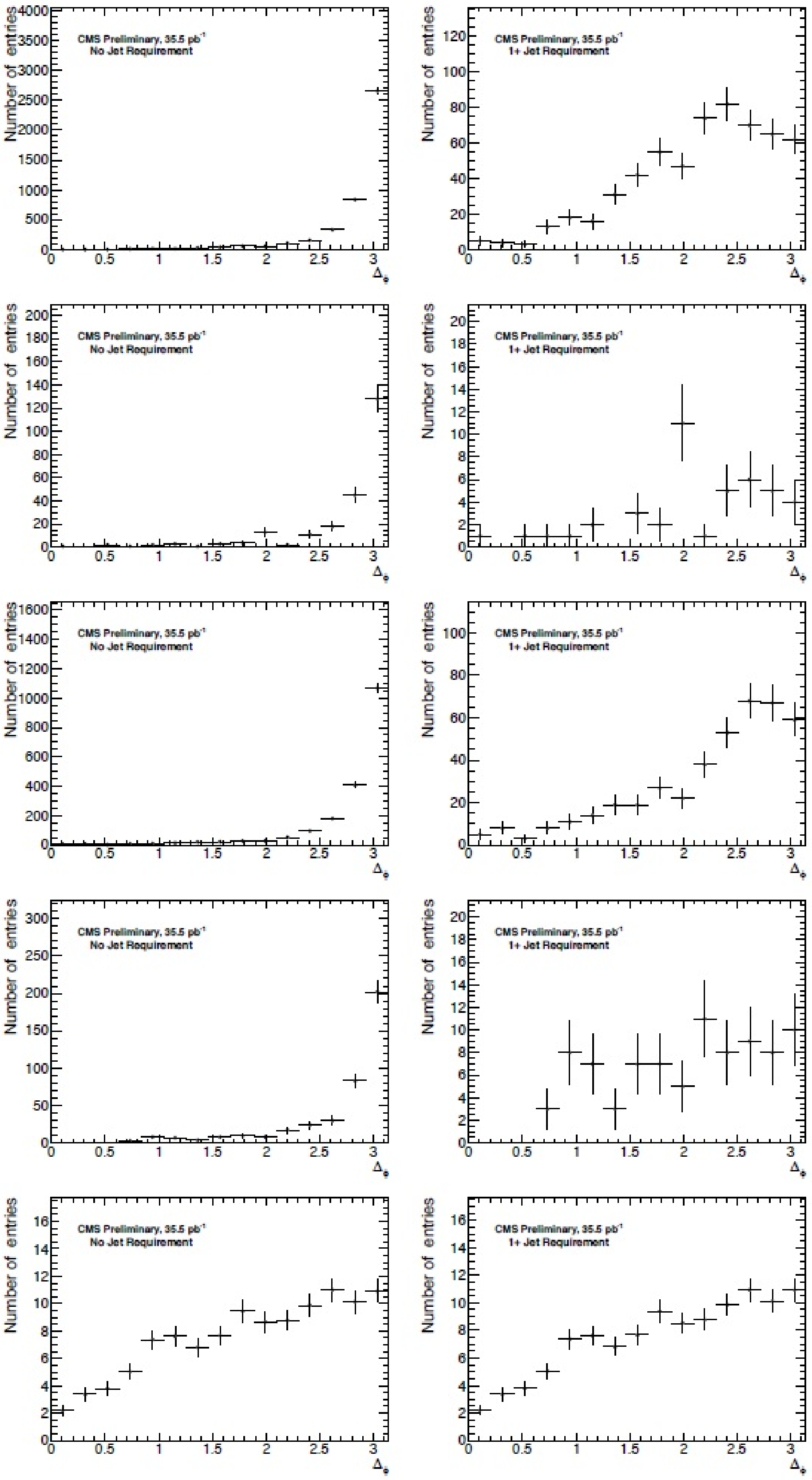

Figure B.20: $\Delta\phi$ distributions between lead and trail objects. 1^{st} row: ee events. 2^{nd} row: $e\gamma$ events. 3^{rd} row: ff events. 4^{th} row: $\gamma\gamma$ events. 5^{th} row: $\gamma\gamma$ events in GGM signal MC. Left plots: no jet required. Right plots: $\geq$1 jet required.

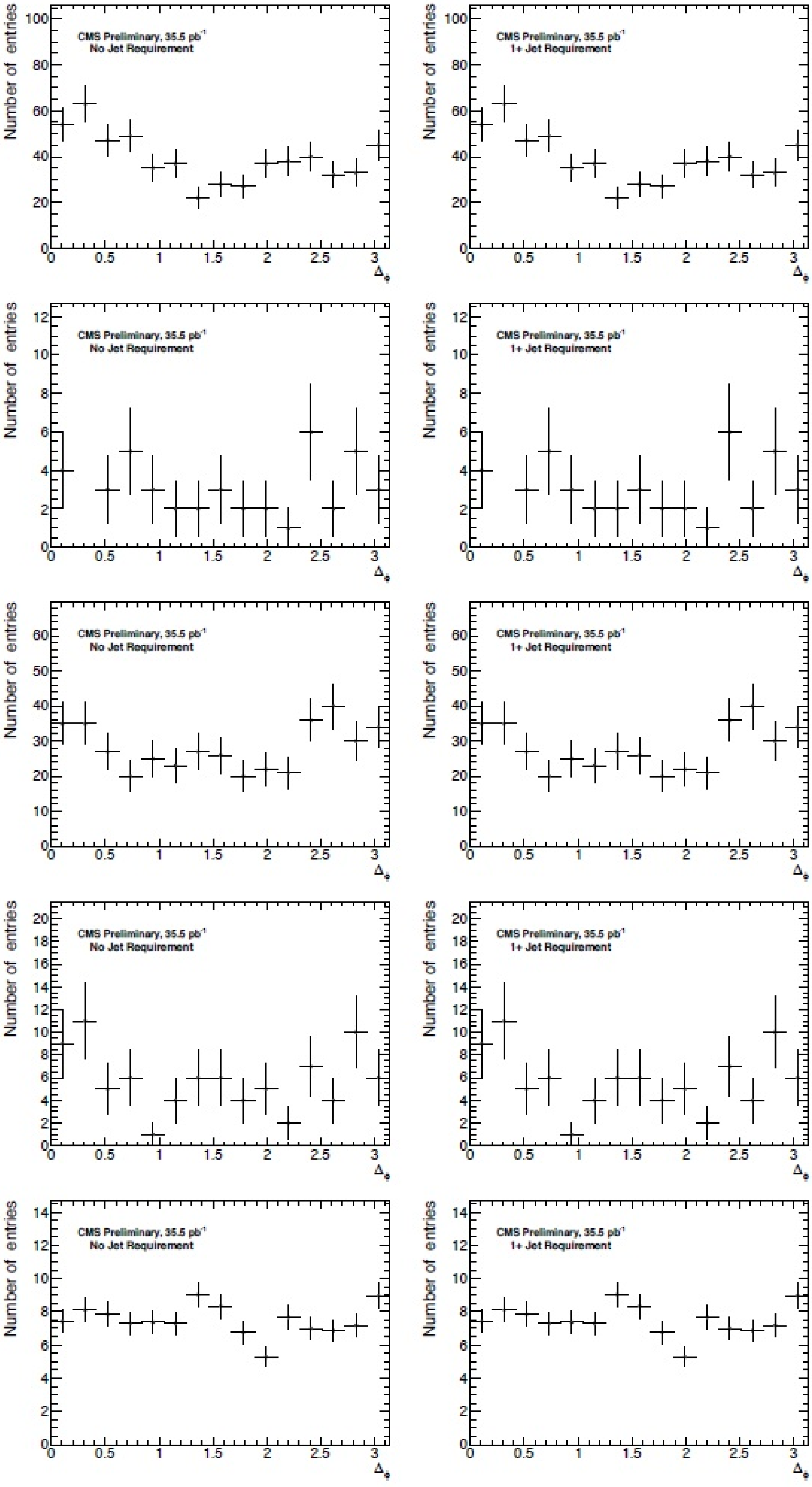

Figure B.21: $\Delta\phi$ distributions between highest p_T jet and E_T^{miss}. 1st row: ee events. 2nd row: $e\gamma$ events. 3rd row: ff events. 4th row: $\gamma\gamma$ events. 5th row: $\gamma\gamma$ events in GGM signal MC. Left plots: no jet required. Right plots: ≥1 jet required.

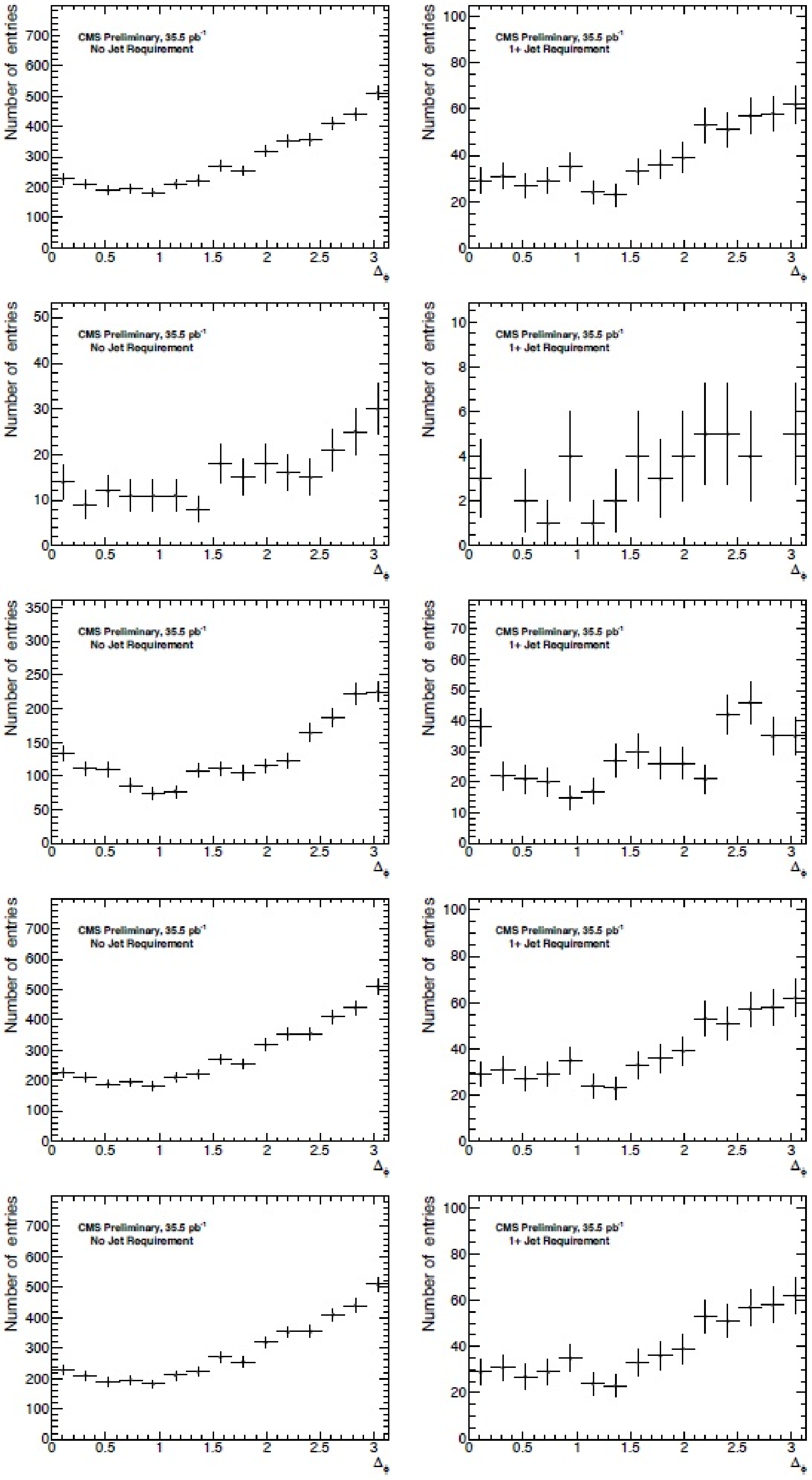

Figure B.22: $\Delta\phi$ distributions between highest p_T jet and E_T^{miss}. 1st row: ee events. 2nd row: $e\gamma$ events. 3rd row: ff events. 4th row: $\gamma\gamma$ events. 5th row: $\gamma\gamma$ events in GGM signal MC. Left plots: no jet required. Right plots: $\geq$1 jet required.

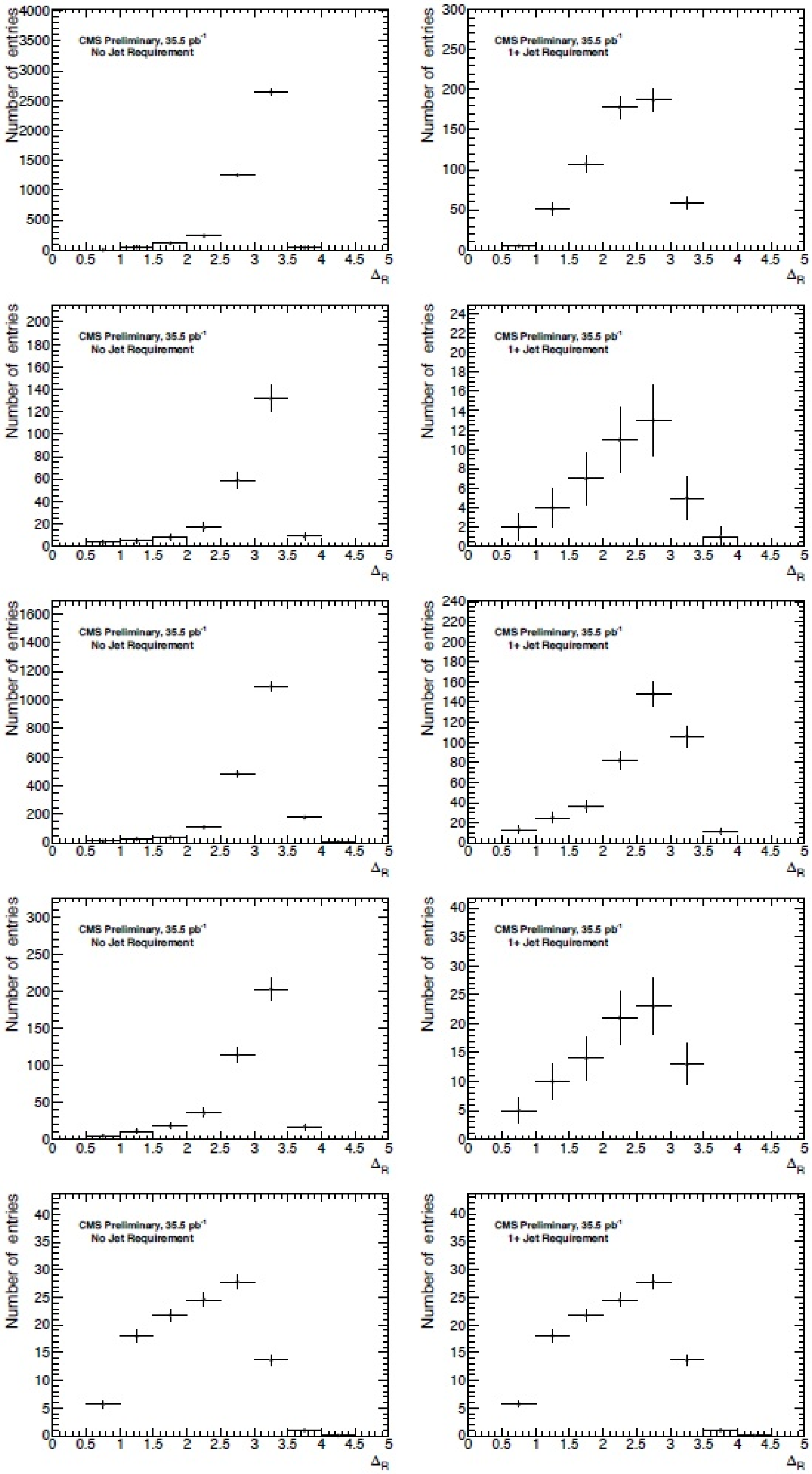

Figure B.23: ΔR distributions between lead and trail objects. 1st row: ee events. 2nd row: $e\gamma$ events. 3rd row: ff events. 4th row: $\gamma\gamma$ events. 5th row: $\gamma\gamma$ events in GGM signal MC. Left plots: no jet required. Right plots: ≥1 jet required.

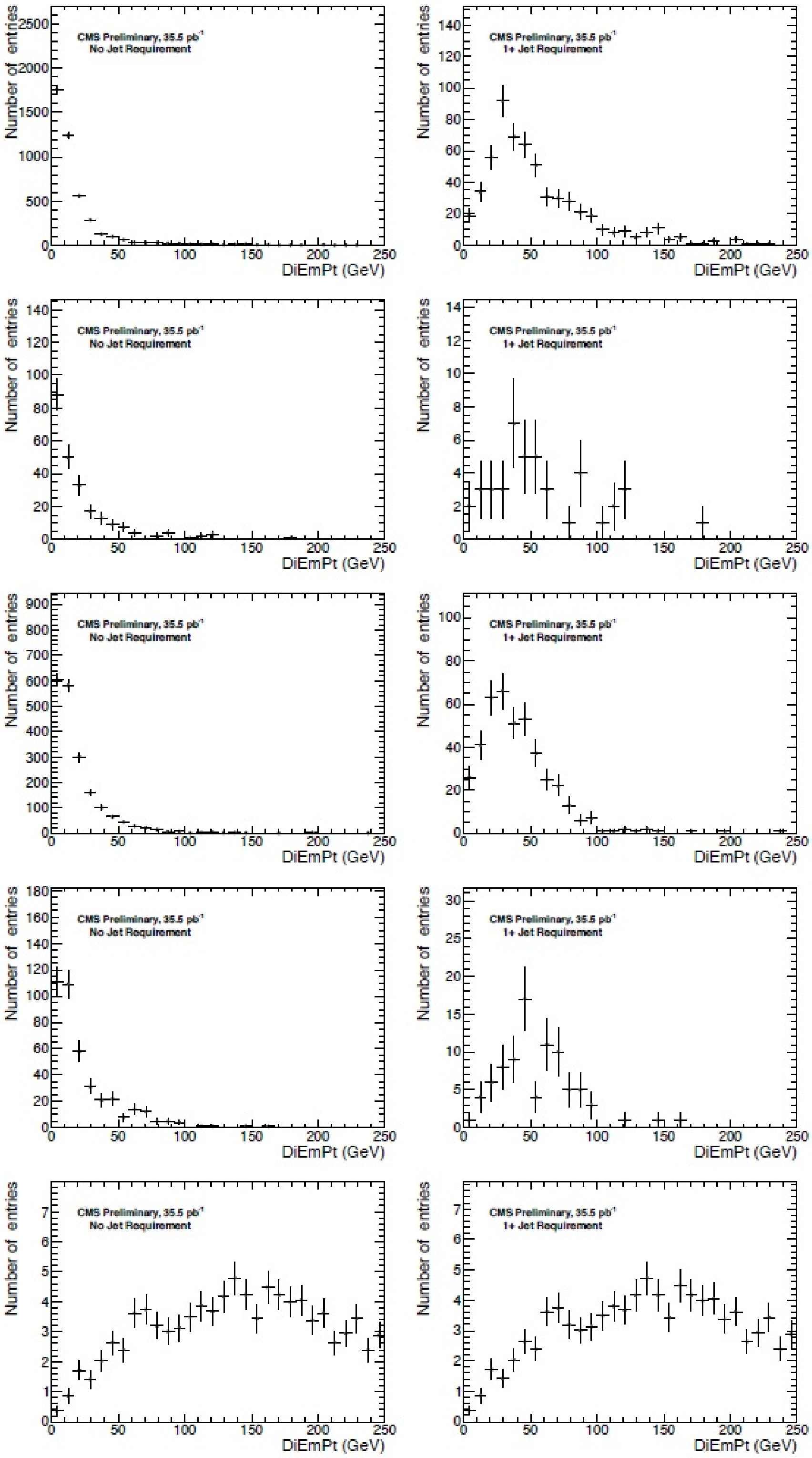

Figure B.24: DI-EMp_T distributions. 1st row: ee events. 2nd row: $e\gamma$ events. 3rd row: ff events. 4th row: $\gamma\gamma$ events. 5th row: $\gamma\gamma$ events in GGM signal MC. Left plots: no jet required. Right plots: $\geq$1 jet required.

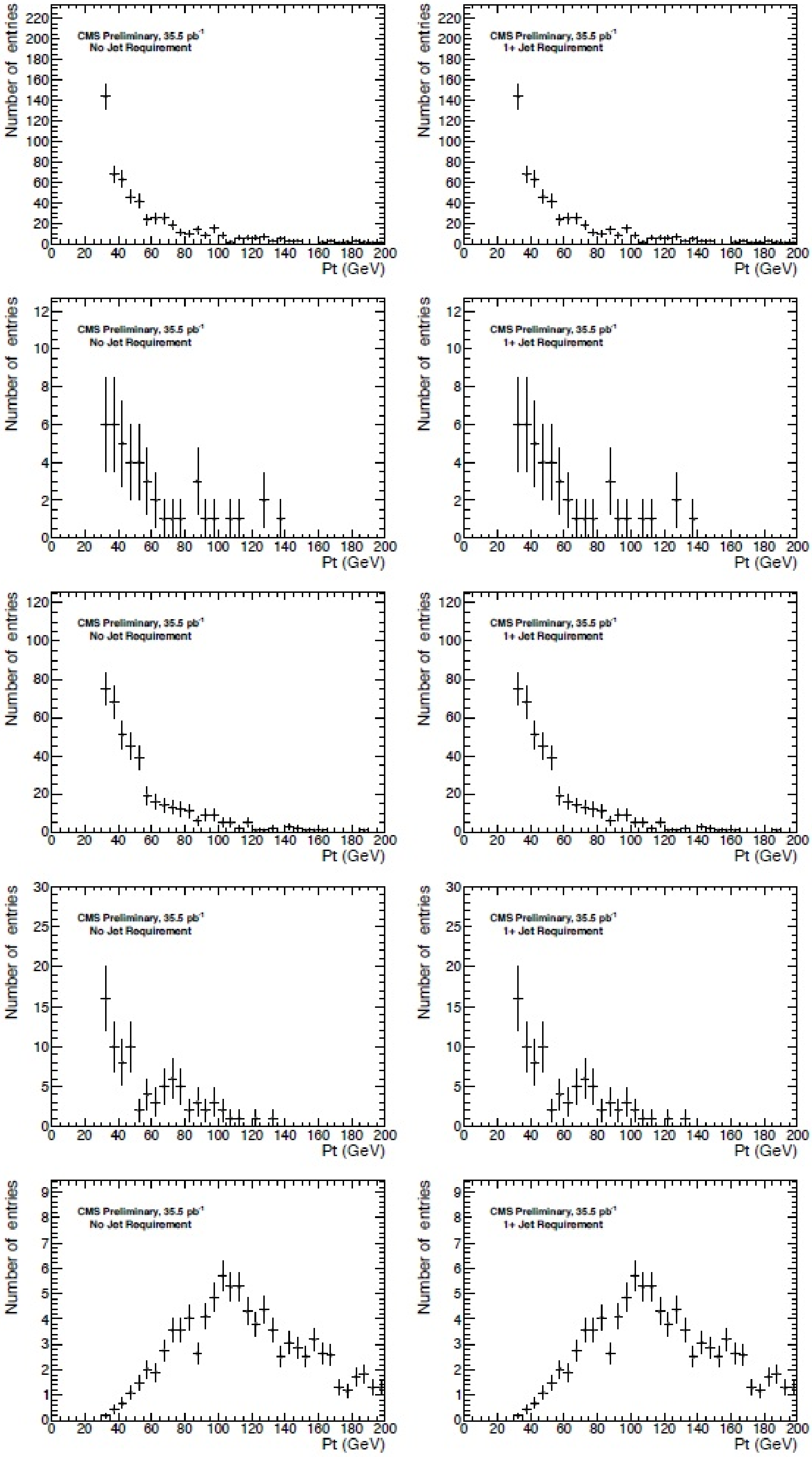

Figure B.25: Leading jet p_T distributions. 1st row: ee events. 2nd row: $e\gamma$ events. 3rd row: ff events. 4th row: $\gamma\gamma$ events. 5th row: $\gamma\gamma$ events in GGM signal MC. Left plots: no jet required. Right plots: ≥1 jet required.

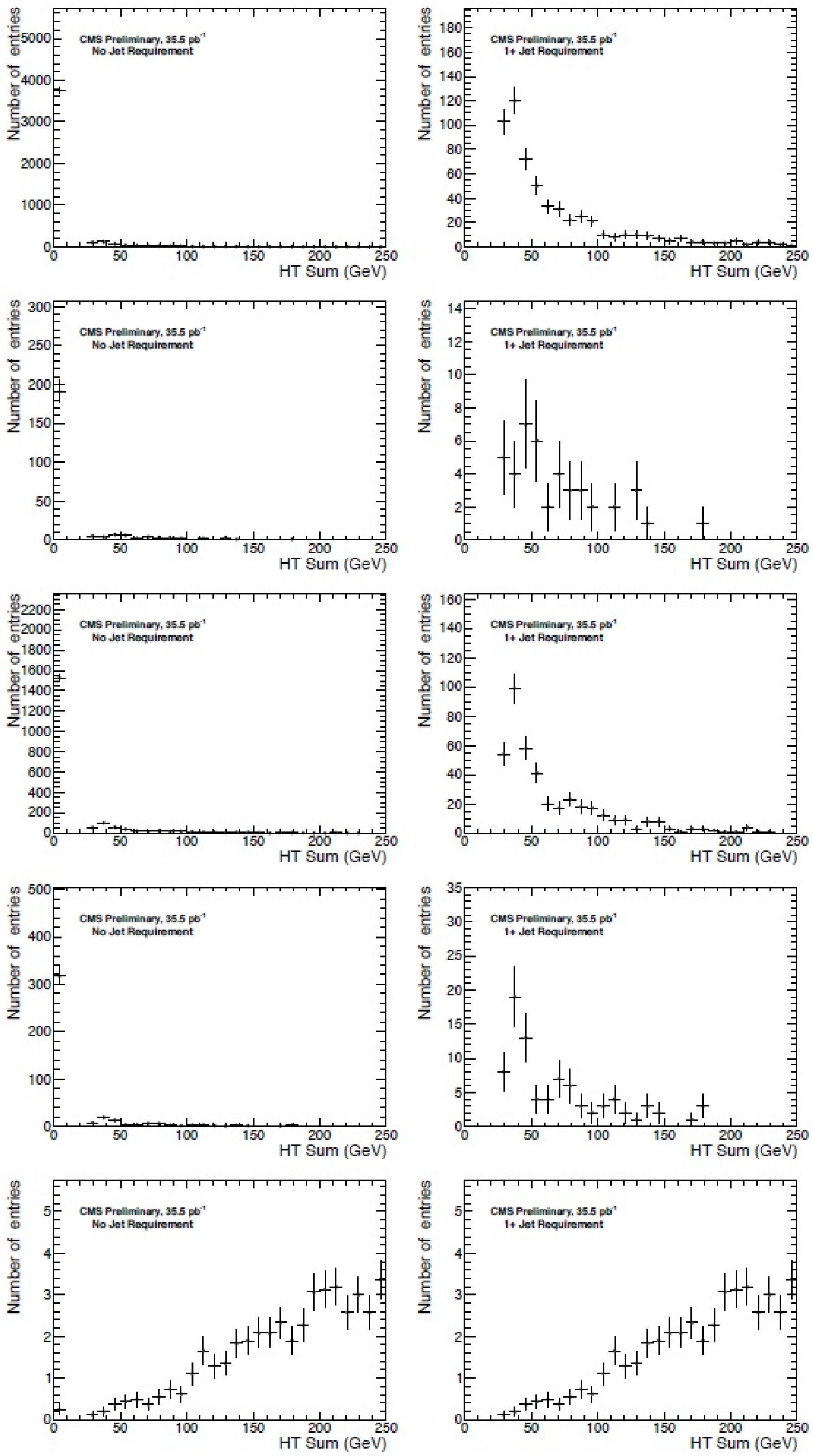

Figure B.26: Jet H_T sum distributions. 1^{st} row: ee events. 2^{nd} row: $e\gamma$ events. 3^{rd} row: ff events. 4^{th} row: $\gamma\gamma$ events. 5^{th} row: $\gamma\gamma$ events in GGM signal MC. Left plots: no jet required. Right plots: ≥1 jet required.

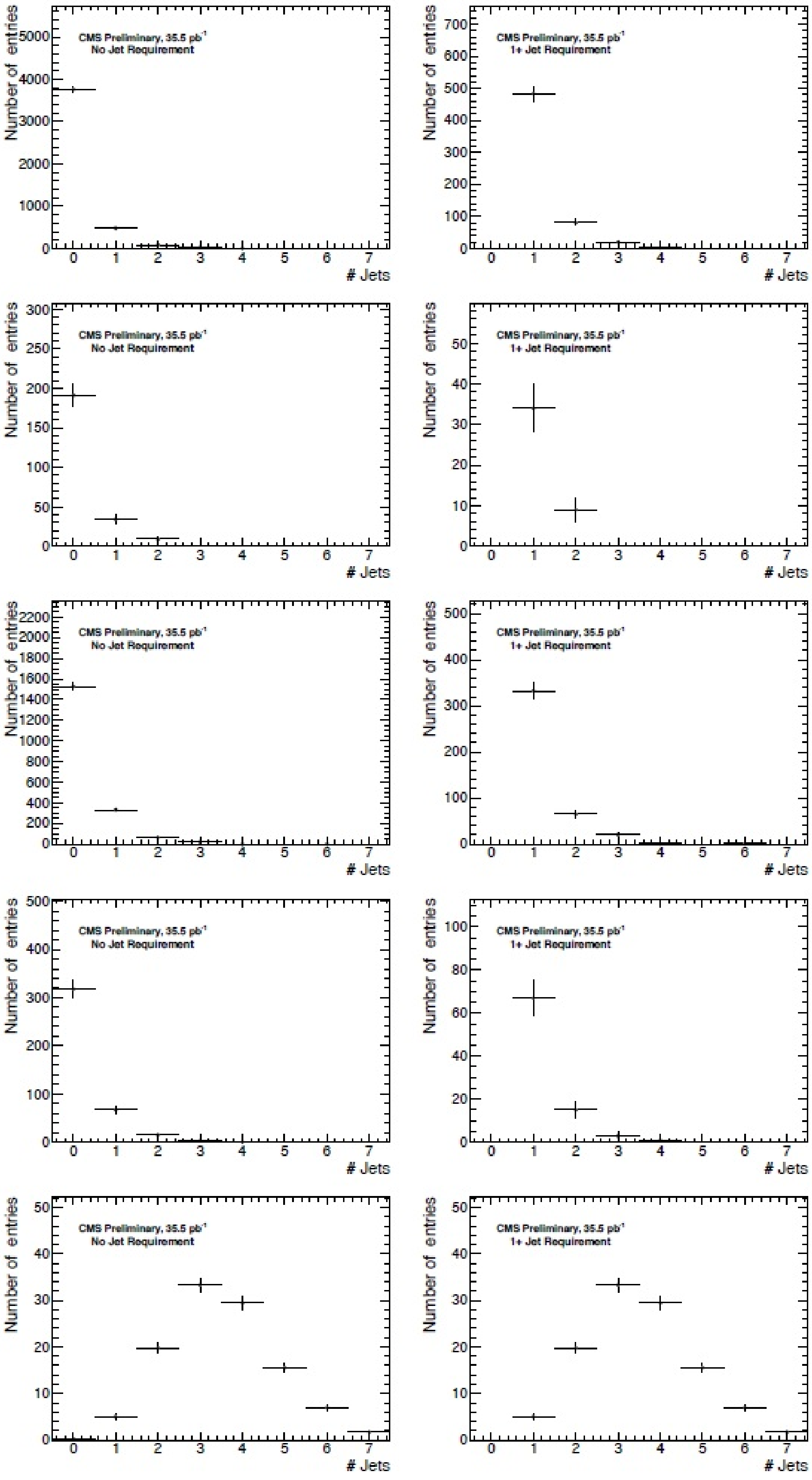

Figure B.27: Distribution of number of jets per event. 1^{st} row: ee events. 2^{nd} row: $e\gamma$ events. 3^{rd} row: ff events. 4^{th} row: $\gamma\gamma$ events. 5^{th} row: $\gamma\gamma$ events in GGM signal MC. Left plots: no jet required. Right plots: ≥1 jet required.

Glossary

CERN European Organization for Nuclear Research, a physics laboratory located in Geneva, Switzerland.. 1, 4, 15, 24, 36, 37, 40, 41

CMS The Compact Muon Solenoid Detector one of four large experiments at the LHC.. xi, xiii, 4, 6, 7, 15, 16, 18–22, 24, 25, 28, 30–32, 36, 40, 42–44, 47–49, 73, 77, 79, 91, 93, 94, 97, 98, 101, 118, 139, 140

CMSSW CMS Software, the physics analysis software package used for analysis of CMS data.. 92, 93, 95, 101, 139–141

CSC Cathode Strip Chambers, part of the CMS endcap muon system.. 16, 32–34

DCS Detector Control System, software system using for controlling and monitoring the detector.. 36, 40, 42–49, 51

DT Drift Tubes, part of the CMS barrel muon system.. 16, 32–34

ECAL Electromagnetic Calorimeter, CMS subdetector for measuring the energy of EM particles and jets.. xiii, 25, 28–30, 73, 75–79, 86, 90, 91, 93, 96–98, 102, 104, 106, 112

FSM Finite State Machine, a hierarchy of logical and hardware devices that compiles state information and propagates commands.. 40–42, 48, 49, 51, 53

GGM General Gauge Mediation, a form of GMSB using more parameters.. xiii, xiv, 2, 67, 71, 90, 97, 100–102, 104, 107, 108, 110, 119–121, 123, 124, 126, 128, 130, 133

GMSB Gauge Mediated Supersymmetry Breaking, a SUSY model that uses gauge interactions to break the symmetry of SUSY.. 2, 64

HB Hadronic Calorimeter Barrel, part of the CMS HCAL covering the barrel region.. 31

HCAL Hadronic Calorimeter, CMS subdetector for measuring the energy of hadronic jets.. 31, 75, 76, 79, 86, 93, 96, 98, 104, 112

HE Hadronic Calorimeter Endcap, part of the CMS HCAL covering the endcap region.. 31

HF Forward Hadronic Calorimeter, part of the CMS HCAL covering the extreme forward regions.. 31, 32

HLT High Level Trigger, software based triggering system used to reduce the event rate.. 35

HO Outer Hadronic Calorimeter, part of the CMS HCAL located outside the solenoid coil.. 31

JCOP Joint Controls Project, PVSS software framework developed at CERN to provide generic tools for interfacing with commonly used hardware systems.. 40, 41

JSON JavaScript Object Notation, a file format used by JavaScript to contain delimited information.. 91

KK Kaluza-Klein, theory of particles in higher dimensions suggested by the works of Theodor Kaluza and Oskar Klein.. 3, 67–70, 124

L1T Level 1 Trigger, hardware based triggering system used to reduce the event rate.. 34, 35

LED Large Extra Dimensions, a theory that posulates the existence of one or more extra dimensions in which only gravity propagates.. 3

LHC The Large Hadron Collider, a hadron collider measuring 27 km in circumference, located at CERN.. xii, 1, 4–8, 10–16, 22, 23, 28, 29, 34, 36, 37, 48, 66, 70, 72, 100, 122

LHE Les Houches Events, a file containing Monte Carlo generated events that can be then used by different physics simulation packages.. 140

LKP The Lightest Kaluza-Klein Particle, the KK particle with the lowest mass.. 3, 68–70

LSP The Lightest Superpartner, the lowest mass SUSY particle.. 2, 59, 65, 66

MSSM Minimally Supersymmetric Standard Model, the minimal extension to the SM to include supersymmetry.. 59–61, 64

NLSP The Next to Lightest Superpartner, the SUSY particle with the 2^{nd} lowest mass.. 2, 65, 66, 100

PDF Parton Distribution Function, a function that describes the distribution of momentum in the colliding protons.. xiv, 122–124, 126, 128, 130, 132

PLC Programmable Logic Controller, a programmable hardware system used to perform actions based on sensor data. Used primarily for safety systems.. 36, 41, 42, 51, 53

PS Proton Synchrotron, one of the accelerators in the CERN LHC complex.. 14

PSB Proton Synchrotron Booster, one of the accelerators in the CERN LHC complex.. 14

PSU Power Supply Unit, one of over two thousand power supplies providing high and low voltages to the CMS Tracker.. 50

PVSS Detector Control Unit, on-board chip providing temperature, voltage, and current information for each tracker module.. 43

PVSS Prozess-Visualisierungs-und-SteuerungsSystem, software SCADA system used at CERN to develop DCS systems.. 36–42, 46

QCD Quantum Chromodynamics, the theory of the strong nuclear force, which decribes the interactions of quarks and gluons.. vi, xiv, 31, 75, 80, 112, 113, 116, 119

RF Radio Frequencies.. 13

RPC Resistive Chambers, part of the CMS muon system, used in conjection with the DTs and CSCs, providing better time resolution.. 16, 32, 34

SCADA Supervisory Control and Data Acquisition, type of software used for control systems.. 36

SLHA Supersymmetry Les Houches Accord, file format for describing SUSY particles and decays that can be used by PYTHIA or other MC generators.. 100, 140

SM The Standard Model of particle physics. A successful model of particle physics describing the known particles and their interactions.. 2, 3, 55–60, 67, 69, 71

SPS Super Proton Synchrotron, one of the accelerators in the CERN LHC complex.. 14

SUSY Supersymmetry, the theory that every standard model has a counterpart with a 1/2 spin difference.. 2, 57–60, 64, 65, 67, 69, 71, 100, 101, 104, 140

TEC Tracker Endcap, subsystem of the CMS Silicon Strip Tracker.. 24, 47

TIB Tracker Inner Barrel, subsystem of the CMS Silicon Strip Tracker.. 24, 47, 48

TID Tracker Inner Disks, subsystem of the CMS Silicon Strip Tracker.. 24, 47

TOB Tracker Outer Barrel, subsystem of the CMS Silicon Strip Tracker.. 24, 47, 48

TTC Trigger, Timing, and Control, a system providing for the distribution of trigger and fast control signals.. 48, 53

UED Universal Extra Dimensions, a theory that posulates the existence of one or more small extra dimensions in which all SM particles propagates.. xiii, xiv, 3, 67–69, 71, 100–102, 104, 107, 108, 119, 121, 124, 126, 130, 132, 133